

Alma Mater Studiorum – Università di Bologna

DOTTORATO DI RICERCA IN

MECCANICA E SCIENZE AVANZATE DELL'INGEGNERIA

Ciclo XXXII

**Settore Concorsuale: 09/C2**

**Settore Scientifico Disciplinare: ING/IND-18**

NON-EQUILIBRIUM ATMOSPHERIC PLASMA AS A NOVEL  
ROUTE TO NANOMATERIAL SYNTHESIS AND PROCESSING FOR  
BIOMEDICAL APPLICATIONS

**Presentata da: Tommaso Gallingani**

**Coordinatore Dottorato  
Prof. Marco Carricato**

**Supervisore  
Prof. Vittorio Colombo**

**Co-supervisore  
Dott. Matteo Gherardi**

**Esame finale anno 2020**

*“Una volta che abbiate conosciuto il volo, camminerete sulla terra guardando il cielo, perché è là che siete stati ed è là che desidererete tornare.”*  
*Leonardo da Vinci*

*“Every occurrence in Nature is preceded by other occurrences which are its causes, and succeeded by others which are its effects. The human mind is not satisfied with observing and studying any natural occurrence alone, but takes pleasure in connecting every natural fact with what has gone before it, and with what is to come after it.”*  
*John Tyndall*

# Table of contents

<b>Abstract</b>	<b>6</b>
<b>Introduction</b>	<b>7</b>
<b>Outline</b>	<b>9</b>
<b>CHAPTER 1 Plasma Processing of Bio and Nanomaterials: an Overview</b>	<b>15</b>
1.1 Introduction	16
1.2 Plasma assisted deposition of antibacterial and antifouling coatings	16
1.2.1 <i>Passive strategies</i>	17
1.2.2 <i>Active strategies</i>	18
1.3 Plasma and droplets for biomaterial processing	21
1.4 References	24
<b>CHAPTER 2 Non-thermal Plasma Assisted Deposition of Silver-Based Nanostructured Coatings to Prevent Biofilm Proliferation and Clot Formation</b>	<b>27</b>
2.1 Introduction	28
2.2 Materials & Methods	31
2.2.1 <i>Plasma assisted deposition on 2D substrate</i>	31
2.2.2 <i>Plasma assisted deposition on mini catheters</i>	35
2.3 Results & Discussion	38
2.3.1 <i>Plasma assisted coating deposition on 2D substrate</i>	38
2.3.2 <i>Plasma assisted coating deposition on mini catheters</i>	47
2.4 Conclusions	52
2.5 References	53
2.6 Appendix	59
2.6.1 <i>Plasma assisted deposition on 2D substrates</i>	59
2.6.2 <i>Plasma assisted deposition on mini catheters</i>	61
<b>CHAPTER 3 In-flight Synthesis and Online Characterization of Silver Nanoparticles from Aerosol Droplets Reacting in a Non-thermal Plasma</b>	<b>63</b>

3.1	Introduction.....	64
3.2	Materials & Methods .....	68
3.2.1	<i>Plasma reactor</i> .....	68
3.2.2	<i>Electrical characterization</i> .....	68
3.2.3	<i>Droplets characterization</i> .....	69
3.2.4	<i>Nanoparticle characterization</i> .....	70
3.2.5	<i>Diffusion dryer experiment</i> .....	72
3.2.6	<i>Effect of residence time</i> .....	72
3.3	Results & Discussion.....	73
3.3.1	<i>Influence of water droplets in the silver reduction</i> .....	81
3.3.2	<i>Process efficiency</i> .....	83
3.4	Conclusions .....	87
3.5	References .....	88
3.6	Appendix .....	94
3.6.1	<i>Droplet flow visualization</i> .....	94
3.6.2	<i>Physical database used for calculation</i> .....	95
3.6.3	<i>Control experiment with aerosol drying before the DMA</i> .....	95
<b>CHAPTER 4 Experimental and simulative approach for the investigation of droplet evaporation in a flow-through non-thermal plasma reactor.....</b>		<b>96</b>
4.1	Introduction.....	97
4.2	Materials & Methods .....	100
4.2.1	<i>Experimental setup</i> .....	100
4.2.2	<i>Evaporation model</i> .....	103
4.3	Results & Discussion.....	109
4.3.1	<i>Experimental setup characterization and calibration</i> .....	109
4.3.2	<i>Simulation of droplet evaporation</i> .....	118
4.3.3	<i>Comparison of experimental and simulation results</i> .....	121
4.4	Conclusions .....	123
4.5	References .....	124
4.6	Appendix .....	129

4.6.1 Procedure for simulative data correction and comparison with experimental results .....	129
<b>Conclusions and Perspectives .....</b>	<b>130</b>
<b>Acknowledgments .....</b>	<b>132</b>

# Abstract

Since last century, the rising interest of value-added and advanced functional materials has spurred a ceaseless development in terms of industrial processes and applications. Among the emerging technologies, thanks to their unique features and versatility in terms of supported processes, non-equilibrium plasma discharges appear as a key solvent-free, high-throughput and cost-efficient technique. Nevertheless, applied research studies are needed with the aim of addressing plasma potentialities optimizing devices and processes for future industrial applications.

In this framework, the aim of this dissertation is to report on the activities carried out and the results achieved concerning the development and optimization of plasma techniques for nanomaterial synthesis and processing to be applied in the biomedical field. In the first section, the design and investigation of a plasma assisted process for the production of silver (Ag) nanostructured multilayer coatings exhibiting anti-biofilm and anti-clot properties is described. With the aim on enabling in-situ and on-demand deposition of Ag nanoparticles (NPs), the optimization of a continuous in-flight aerosol process for particle synthesis is reported. The stability and promising biological performances of deposited coatings spurred further investigation through *in-vitro* and *in-vivo* tests which results are reported and discussed. With the aim of addressing the unanswered questions and tuning NPs functionalities, the second section concerns the study of silver containing droplet conversion in a flow-through plasma reactor. The presented results, obtained combining different analysis techniques, support a formation mechanism based on droplet to particle conversion driven by plasma induced precursor reduction. Finally, the third section deals with the development of a simulative and experimental approach used to investigate the in-situ droplet evaporation inside the plasma discharge addressing the main contributions to liquid evaporation in the perspective of process industrial scale up.

# Introduction

Aimed at improving the substrate performances and introducing surface functionalities, surface engineering science moved its first steps from the trailblazing and revolutionary work done by Irvin Langmuir and Katherine Blodgett during the first years of the last century. In the last few decades the astonishing achievements of the research field, together with the raise of the industrial interest for interface phenomena gave birth to totally new branches, entirely devoted to the investigation and application of surface driven interactions. Sometimes inspired by the nature architecture (e.g. lotus effect, hexagonal packed array-based wings, nacre), the possibility to tailor material functionalities with the aim of controlling their surface properties without affecting the bulk material has become the main focus of the so called “biointerface science”. The great achievements in the field of nanotechnology and nanofabrication have further increased the variety of techniques and functionalities achievable. Simultaneously, the growing need for clear-cut functionalities able to face the wider knowledge gained in the biology field and to cope with new diseases (e.g bacterial resistance) has risen even more the expectations from surface engineering science.

In this framework, the unique features and the non-equilibrium chemistry of low-temperature plasma discharges have intrigued material scientists keen to modify surface functionalities of thermosensitive biomaterials. The possibility to customize surface topography, tune surface free energy and deposit functional coatings exploiting low pressure plasmas was achieved thanks to important works done during the second part of the last century. Only recently, thanks to the efforts done in the field of high voltage generation and design of plasma reactors, plasma scientists were able to reproduce the results accomplished at reduced pressure and move further steps in the tailoring of biomaterial properties at atmospheric pressure. While great achievements were obtained in terms of material properties (e.g. biocompatibility, selectivity) and introduced functionalities, the lack of comprehensive approaches has currently limited industrial application of the technology at ambient pressure. Unanswered questions and, sometimes, the unbalance between fundamental and applied research have indeed hindered the scale up of atmospheric plasma

sources and processes. Nevertheless, the impact of plasma as flexible and solvent-free alternative to traditional chemical processes appears immense. Moreover, the recent interest of research scientists with different background (e.g. material scientists, chemists, biologists, physicians) together with the feasibility of in-situ and localized (down to micron dimensions) plasma assisted functionalization bodes well for future industrial application of plasma science and technology.

# Outline

My PhD program has been focused on the design, development and optimization of novel non-equilibrium plasma processes to support the surface functionalization of biomaterials through the deposition of nanostructured coating. In the perspective of the development of a new class of plasma treated biomaterials able to prevent biofilm adhesion and proliferation, my PhD grant was funded and supported by Democenter-Sipe foundation ([www.democentersipe.it](http://www.democentersipe.it), Modena, Italy) in cooperation with the Technopole of Mirandola ([www.tpm.bio](http://www.tpm.bio), Mirandola (MO), Italy), top-level Italian research centre in the biomedical device field. The main part of the research activities related to plasma process design and diagnostic were carried out in the laboratories of the Research Group for Industrial Application Plasmas (IAP group; <http://plasmagroup.ing.unibo.it/>) at the Department of Industrial Engineering of the Alma Mater Studiorum-Università di Bologna under the supervision of Prof. Vittorio Colombo and Dott. Matteo Gherardi. The fruitful cooperation with the Technopole of Mirandola enabled us to focus the problem to be solved related to the study here presented and to carry out the biological characterization of the treated biomaterials. To gain a better knowledge on the role of process parameters and shed some light on plasma-aerosol interaction, a fruitful international scientific cooperation with the research group headed by Prof. Mohan Sankaran at Case Western Reserve University (Cleveland, Ohio, US) has been established.

This dissertation is organized in five main sections, reporting the results achieved during the PhD studies with respect to the current state of the art of plasma applications in the field of biomaterials treatment and functionalization. After a brief overview of the literature published so far, the second chapter presents the results achieved regarding the design and optimization of a plasma assisted process for the deposition of anti-clot and anti-biofilm silver nanostructured coating on 2D and 3D substrates. Having in view the final industrial application, the process was designed exploiting the possibility to in-situ and on-demand synthesized silver nanoparticles through plasma reduction of an aerosol containing silver salt solution. The results obtained with regards to the chemical, morphological and biological

characterization of treated biomaterials spurred the research activities in the direction of a better understanding of the synthesis step, with the aim of controlling nanoparticles properties and tuning material functionalities. A deep investigation of in-flight synthesis carried out in the framework of a joint project with Case Western Reserve University is then described in the third and fourth chapter, mainly focused on the synthesis mechanism and on plasma-aerosol interactions, respectively. Finally, the last chapter summarizes the reached achievements, outlining future perspectives.

In the framework of this applied research project, the proof of concept of plasma process feasibility and the promising results achieved, brought up unanswered scientific questions on possibility to tailor nanostructure characteristics with the aim of controlling material functionalities. The challenging task of balancing efforts between fundamental and applied approach has been achieved thanks to a fruitful collaboration among researchers belonging to different research fields. While offering a unique opportunity for a personal and scientific growth, the cooperation with different research groups has enabled a multidisciplinary view on results achieved and improved the quality of the work here presented.

Part of the results obtained during my PhD studies are discussed in the following papers published in international journals:

- i. Liguori A, Galligani T, Padmanaban D B, Laurita R, Velusamy T, Jain G, Macias-Montero M, Mariotti D and Gherardi M 2018 *Synthesis of Copper-Based Nanostructures in Liquid Environments by Means of a Non-equilibrium Atmospheric Pressure Nanopulsed Plasma Jet* Plasma Chem. Plasma Process. **38** 1209-1222;
- ii. Stancampiano A, Galligani T, Gherardi M, Machala Z, Maguire P, Colombo V, Pouvesle J-M M and Robert E 2019 *Plasma and Aerosols: Challenges, Opportunities and Perspectives* Appl. Sci. **9** 3861.

Moreover, the research activities presented in the second and third chapters will be presented in two scientific papers that are currently under preparation:

- i. Galligani T, Abuyazid N, Gherardi M, Colombo V, Sankaran RM, *In-flight Synthesis and Online Characterization of Silver Nanoparticles from Aerosol Droplets Reacting in a Non-thermal Plasma*, to be submitted to Journal of Physics D: Applied Science (late 2019);
- ii. Galligani T, Laurita R, Gherardi M, Colombo V, Resca E, Mari G, Petrachi, T, Dominici M, Veronesi E, *Atmospheric Non-Thermal Plasma Assisted Deposition of Silver-Based Nanostructured Coatings to Prevent Biofilm Proliferation and Clot Formation*, to be submitted to Scientific Reports (late 2019).

The results achieved during the three years of program have also been disseminated as oral and poster presentations (where underlined, I have been the presenter):

- i. M. Gherardi, V. Colombo, F. Barletta, A. Bisag, C. Bucci, F. Capelli, R. Laurita, E. Mezzofanti, T. Gallingani, G. Girolimetti, S. Colucelli, L. Amato, G. Gasparre, M. Perrone, AM. Porcelli, PA. De Iaco, “*On the Versatility of Atmospheric Non-equilibrium Plasmas: Material Synthesis, Packaging Sanitation and Oncological Applications*» invited presentation at AVS66, 66<sup>th</sup> American Vacuum Society International Symposium & Exhibition, Columbus, Ohio, US, 20-25 October 2019;
- ii. T. Gallingani, N. Abuyazid, M. Gherardi, V. Colombo, C. Hogan, M. Sankaran “*In-flight Synthesis and Online Characterization of Silver Nanoparticles from Aerosol Droplets Reacting in a Non-thermal Plasma*» accepted as oral presentation at AVS66, 66<sup>th</sup> American Vacuum Society International Symposium & Exhibition, Columbus, Ohio, US, 20-25 October 2019;
- iii. D. Duday, H. Malekzad, T. Gallingani, F. Barletta, M. Gherardi, V. Colombo, «*Single-step deposition of surface chemical gradients with a corona jet at atmospheric pressure*» poster presentation at ISPC24, 24th International Symposium on Plasma Chemistry, Naples, Italy 9-14 June 2019;
- iv. T. Gallingani, R. Laurita, A. Liguori, M. Gherardi, V. Colombo, E. Resca, G. Mari, T. Petrachi, M. Dominici, E. Veronesi, “*Cold atmospheric plasma assisted deposition of nanostructured coatings to reduce biofilm adhesion and proliferation*» oral presentation at ISPC24, 24th International Symposium on Plasma Chemistry, Naples, Italy 9-14 June 2019;
- v. M. Gherardi, V. Colombo, M. Boselli, A. Liguori, R. Laurita, T. Gallingani, “*Equilibrium and non-equilibrium atmospheric plasma routes for nanoparticle synthesis*» invited presentation at MRS Fall Meeting & Exhibit, Boston, Massachusetts, US 25-30 November 2018;
- vi. H. Malekzad, T. Gallingani, F. Barletta, M. Gherardi, V. Colombo, D. Duday, “*Generation of surface chemical gradients by an atmospheric-pressure plasma jet*» oral presentation at 5th International Workshop Plasma Science & Interfaces, St. Gallen, Switzerland 18-19 October 2018;
- vii. T. Gallingani, R. Laurita, A. Liguori, M. Gherardi, V. Colombo, E. Resca, G. Mari, T. Petrachi, M. Dominici, E. Veronesi, “*Cold atmospheric plasma assisted deposition of nanostructured coatings to reduce biofilm adhesion and proliferation*» poster presentation at 29th Annual Meeting of the European Society for Biomaterials, Maastricht, The Netherlands 9-13 September 2018;
- viii. G. Boscaini, V. Colombo, G. De Santis, R. Di Gesù, M. Dominici, M.L. Focarete, T. Gallingani, M. Gherardi, C. Gualandi, A. Liguori, G. Mari, M.S. Piccinno, V Strusi, E. Veronesi, “*Development of cold atmospheric plasma (CAP) functionalized membranes for the selective capture of adipose-derived mesenchymal stromal/stem cells*» oral presentation at 29th Annual Meeting of

- the European Society for Biomaterials, Maastricht, The Netherlands 9-13 September 2018;
- ix. T. Gallingani, R. Laurita, A. Liguori, M. Gherardi, V. Colombo, E. Resca, G. Mari, T. Petrachi, M. Dominici, E. Veronesi, “*Cold atmospheric plasma assisted deposition of nanostructured coatings to reduce biofilm adhesion and proliferation*» oral presentation at 7th International Conference on Plasma Medicine, Philadelphia, USA 17-22 June 2018;
  - x. G. Boscaini, V. Colombo, G. De Santis, R. Di Gesù, M. Dominici, M.L. Focarete, T. Gallingani, M. Gherardi, C. Gualandi, A. Liguori, G. Mari, M.S. Piccinno, V. Strusi, E. Veronesi, “*Development of cold atmospheric plasma (CAP) functionalized membranes for the selective capture of adipose-derived mesenchymal stromal/stem cells*» poster presentation at 7th International Conference on Plasma Medicine, Philadelphia, USA 17-22 June 2018;
  - xi. A. Liguori, E. Traldi, T. Gallingani, R. Laurita, A. Pollicino, M. L. Focarete, V. Colombo, M. Gherardi, “*Co-deposition of antibacterial nanocomposite coatings using a non-equilibrium atmospheric pressure plasma jet* » poster presentation at 8th International Workshop on Polymer Metal Nanocomposites (Nanoworkshop 2017), Praga, Czech Republic, 12-15 September 2017;
  - xii. A. Liguori, T. Gallingani, R. Laurita, F. Barletta, M. L. Focarete, C. Albonetti, A. Pollicino, V. Colombo, M. Gherardi, “*Deposition of polymeric films and co-deposition of nanocomposite coatings by means of a cold atmospheric pressure plasma jet* » oral presentation at 28th Annual Meeting of the European Society for Biomaterials, Athens, Greece 4-8 September 2017;
  - xiii. M. Gherardi, L. S. Dolci, T. Gallingani, A. Liguori, A. Merlettini, L. Calzà, M. Castellucci, V. Colombo, M.L. Focarete, “*Non-equilibrium atmospheric pressure plasma technology for anti-CD 10 antibody immobilization on poly(L-lactic) acid nanofibres*» poster and poster pitch presentation at 23rd International Symposium on Plasma Chemistry, Montréal, Canada 30 July – 4 August 2017;
  - xiv. A. Liguori, T. Gallingani, D.B. Padmanaban, R. Laurita, T. Velusamy, G. Jain, M. Macias-Montero, V. Colombo, D. Mariotti, M. Gherardi, “*Copper-based nanostructures synthesis in liquid environment assisted by a non-equilibrium atmospheric plasma jet* » oral presentation at 23rd International Symposium on Plasma Chemistry, Montréal, Canada 30 July – 4 August 2017;
  - xv. M. Gherardi, A. Liguori, T. Gallingani, R. Laurita, F. Barletta, M. L. Focarete, C. Albonetti, A. Pollicino, V. Colombo, “*Cold atmospheric pressure plasma for the deposition of polymeric films and the codeposition of nanocomposite coatings* » oral presentation at 23rd International Symposium on Plasma Chemistry, Montréal, Canada 30 July – 4 August 2017;

- xvi. A. Liguori, E. Traldi, R. Laurita, T. Gallingani, F. Barletta, M. L. Focarete, A. Pollicino, C. Albonetti, V. Colombo, M. Gherardi, “*Deposition of polymeric films and co-deposition of nanocomposite coatings by means of a cold atmospheric pressure plasma jet* » invited presentation at 17th International Conference on Plasma Physics and Application, Bucarest, Romania 15-20 June 2017;
- xvii. Liguori, T. Gallingani, M. Gherardi, V. Colombo, R. Di Gesù, M. Animini, C. Gualandi, ML. Focarete, M. Dominici, T. Petrachi, E. Resca, E. Veronesi, MS. Piccinno, “*Non-equilibrium atmospheric pressure plasma assisted functionalization of electrospun mats for the selective capture of adipose-derived mesenchymal stromal/stem cells*» oral presentation at the National Congress of the Italian Society of Biomaterials, Milano, Italy 24-26 May 2017;
- xviii. F. Barletta, A. Bisag, M. Boselli, F. Capelli, V. Colombo, T. Gallingani, M. Gherardi, R. Laurita, A. Liguori, A. Miserocchi, E. Simoncelli, A. Stancampiano, E. Traldi, “*New research tools for the field of cold atmospheric plasma applications*» oral presentation at the National Congress of the Italian Society of Biomaterials, Milano, Italy 24-26 May 2017;
- xix. A. Liguori, A. Albertini, F. Barletta, A. Bigi, LS. Dolci, ML. Focarete, T. Gallingani, M. Gherardi, C. Gualandi, A. Miserocchi, MC. Oleari, N. Passerini, V. Colombo, S. Panzavolta, “*Cold atmospheric pressure plasma for the crosslinking of electrospun gelatin mats and gelatin films containing drugs*» poster presentation at the National Congress of the Italian Society of Biomaterials, Milano, Italy 24-26 May 2017;
- xx. Liguori, M.Gherardi, T. Velusamy, T. Gallingani, G. Jain, R. Laurita, E. Traldi, M. Ulivi, D. Mariotti, V. Colombo, “*Non-equilibrium atmospheric pressure plasma synthesis of copper-based nanostructures in liquid environments*» oral presentation at 15th International Conference on Plasma Surface Engineering, Garmisch-Partenkirchen, Germany 12 – 16 September 2016;
- xxi. A. Liguori, T. Gallingani , R. Laurita, F. Barletta, C. Albonetti, A. Pollicino, V. Colombo, M. Gherardi, «*Deposition of plasma-polymerized polyacrylic acid coatings by a non-equilibrium atmospheric pressure plasma jet*» oral presentation at the National Congress of the Italian Society of Biomaterials, Ischia , Italy 13-15 July 2016;
- xxii. Liguori, T. Gallingani, G. Jain, R. Laurita, E. Traldi, M. Ulivi, T. Velusamy, M. Gherardi, D. Mariotti, V. Colombo, «*Non-equilibrium nanopulsed plasma jet for the synthesis of copper-based nanostructures in liquid environments*», oral presentation at International Conference on Electrical Discharges with Liquids (ICEDL 2016), Kocaeli, Turkey 14-16 March 2016.

As part of the IAP group, I had the chance to be co-advisor for BS and MS students of the course of Industrial Applications of Plasmas:

- i. Alina Bisag, *Progettazione, sviluppo e caratterizzazione funzionale di sorgenti di plasma atmosferico di non equilibrio per trattamento di materiali e plasma medicine*, Alma Mater Studiorum-Università di Bologna, 2016 (MS);
- ii. Simona Antoci, *Studio parametrico degli effetti delle condizioni di processo sulle caratteristiche chimico-fisiche di coating a base di silicio depositati su substrati polimerici mediante plasma atmosferico di non equilibrio*, Alma Mater Studiorum-Università di Bologna, 2017 (MS);
- iii. Matteo Faglioni, *Progettazione, realizzazione e analisi prestazionale di sorgenti di plasma di non equilibrio a pressione atmosferica per il crosslinking di film di gelatina per applicazioni biomedicali*, Alma Mater Studiorum-Università di Bologna, 2017 (MS);
- iv. Matteo Castellucci, *Progettazione, sviluppo e caratterizzazione di sorgenti di plasma freddo a pressione atmosferica per la deposizione di coating barriera organici-inorganici su substrati polimerici*, Alma Mater Studiorum-Università di Bologna, 2017 (MS);
- v. Marco Bedosti, *Messa a punto di processi plasma assistiti per la funzionalizzazione di materiali e la sintesi di nanostrutture*, Alma Mater Studiorum-Università di Bologna, 2017 (BS);
- vi. Valentina Motta, *Messa a punto di processi assistiti da plasmi freddi a pressione atmosferica per la sintesi in volo di nanoparticelle e la codeposizione di film polimerici nanostrutturati per applicazioni biomedicali*, Alma Mater Studiorum-Università di Bologna, 2018 (MS);
- vii. Giulia Laghi, *Deposizione plasma assistita di coating barriera a base silicio su packaging polimerici: studio sperimentale e simulativo degli effetti dei parametri di processo*, Alma Mater Studiorum-Università di Bologna, 2018 (MS);
- viii. Davide Tonni Perucci, *Messa a punto di processi plasma assistiti per la funzionalizzazione di materiali e la sintesi di nanostrutture*, Alma Mater Studiorum-Università di Bologna, 2019 (MS).

**CHAPTER 1**  
**Plasma Processing of Bio and**  
**Nanomaterials: an Overview**

## **1.1 Introduction**

As researchers, our perception of the future impact of a new technology strongly depends on the approach used to analyse the current state of the art with the aim of forecasting what is yet to come. This is also true for non-equilibrium plasma technology, which showed great results over the last century in a limited number of industrial fields (e.g. microelectronics, ozone generation). With a view to new potential industrial applications, we should pose more attention discussing “What we can do and what we cannot do with non-equilibrium plasma?”, evolving our approach from the classical question “What do we know and what we do not know about non-equilibrium plasma?”. From the perspective of this paradigmatic shift, the following chapter reports on the achievements of plasma technologies in the field of biomaterial treatment, with a focus on antibacterial nanostructured material processing; through this chapter, peculiarities of low and atmospheric pressure discharges are pointed out, trying to highlight the technical limitations and the unanswered questions that are currently hindering a technological leap forward.

## **1.2 Plasma assisted deposition of antibacterial and antifouling coatings**

In the biomaterial science field, the rising need of a fine control of cell adhesion and proliferation has stimulated scientists’ efforts for the development of active surfaces characterized by tunable characteristics. Indeed, it’s worth remembering that in the biological environment the cell adhesion and proliferation at the liquid-solid interface are

often controlled by complex mechanisms influenced by surface topography, charge, free energy [1]. In this framework, thanks to their versatility in terms of surface patterning, modification of free energy and characteristics of deposited coating, plasma processes have been employed for the surface functionalization of a large number of polymeric materials [2]. With respect to traditional chemical processing, plasma is a solvent-free technology characterized by limited material preparation, easily scalable and highly tunable. Moreover, the great versatility of plasma processes offers the possibility to use different approaches with the aim of tailoring antibacterial and antifouling properties of biomaterials, as recently discussed in [3–7]. In this field, the strategies proposed so far for the surface functionalization can be divided in two main categories (Figure 1.1):

- Passive strategies (Figure 1.1b): aimed at preventing bacterial adhesion through surface micro-nano patterning or the deposition of functional coatings. In this case, the adhesion of bacteria and cells is usually hindered through a modification of biomaterial surface free energy and roughness.
- Active strategies (Figure 1.1c), where antibacterial agents are usually embedded in a polymer matrix or grafted on the material surface. In this regard, optimization of the coating properties requires a thorough control of the antibacterial compound release, to guarantee the antibacterial effect while ensuring a sufficient level of biocompatibility.

### 1.2.1 Passive strategies

In the last decades, plasma processes have been widely used with the aim of controlling fouling and antifouling properties of bulk materials [7–9]. In particular, an interesting review by Milella et al. [10] discussed the possible routes to modify the material morphology at the nano-scale level by means of plasma discharges, highlighting important perspectives for future applications. Furthermore, exploiting an approach based on surface chemistry modification, Sardella [11] and Bret gnol [12] reported on low pressure plasma processes for the deposition of PEO-like coatings characterized by anti-fouling performances. Interestingly, both research groups pointed out the possibility to tailor biomaterial antifouling properties through a control of monomer fragmentation, governing cell adhesion changing plasma discharge parameters (e.g. power). Similar results were achieved by Hegemann et al. [13] that were able to control the adhesion of proteins through the deposition of a coating having a graded chemical composition; according to their results, the removal of oxygen in the plasma reactor during the deposition process enabled the gradual transition from an inorganic coating to an organic one. This vertical gradient structure was found to strongly decrease the protein adsorption, even with respect to the only organic film which was characterized by low protein adhesion. Although the achieved results are promising for future applications, the low pressure nature of the processes has partially limited a widespread industrial use of the technology. In the perspective of a gradual shift to atmospheric pressure processes,

recently Da Ponte et al. [14] reported on the deposition of PEO-like coatings exploiting an aerosol assisted atmospheric plasma process. According to their results, the authors were able to achieve a good control of fouling properties changing the aerosol flow rate and the discharge power. Although a large number of works have been published on this topic, only few have addressed and discussed the stability of deposited coating with regards to long term biological performances [15]. The main limitation of the passive strategies lies in the absence of any cytotoxic effect against bacteria, whose growth is therefore not hindered.

### 1.2.2 Active strategies

Trying to overcome this limitation, the grafting of antimicrobial agents or the embedment of drugs and nanoparticles have been employed to produce active coatings.

The grafting process is usually carried out exploiting the interaction of a plasma discharge in contact with the material to be treated, resulting in the creation of surface functional groups where bioactive molecules are then covalently bonded with wet chemistry approaches. Among others, chitosan, nisin peptides and quaternary ammonium compounds are the

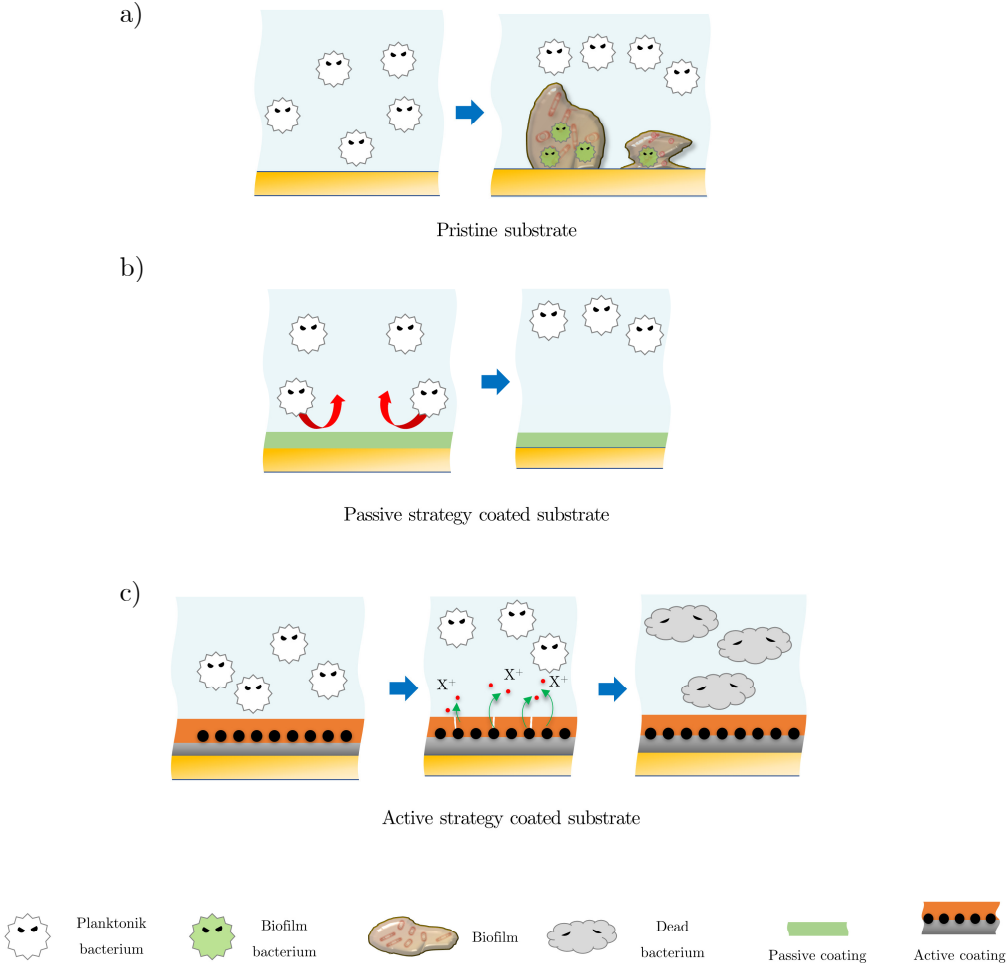


Figure 1.1 Passive (b) and active (c) strategies to control bacteria adhesion and proliferation on pristine substrate (a).

bioactive molecules most frequently immobilized on plasma functionalized polymers. An example of this approach can be found in the paper published by Chang et al. [16], where the authors reported on the antibacterial properties and biocompatibility of a plasma treated polyester fabric where chitosan was grafted. The treated mats exhibited a good level of antibacterial effect against *Staphylococcus aureus* and *Bacillus subtilis* outlining also an optimum level of biocompatibility.

Beside the grafting of antimicrobial compounds, plasma deposited coatings have been proposed for the development of active materials where nanoparticles (NPs) or other antibacterial agents are embedded. Different metal NPs, in terms of chemistry and morphology, have been studied and proposed for the production of antibacterial coatings, with a particular industrial interest for copper (Cu) and silver (Ag) containing films [17]. Even if Ag has been known for over 2000 years for its antibacterial properties against the 16 major species of bacteria, the bactericidal reaction pathways and the toxicity of metal containing coating are still under investigation. Nevertheless, Ag appears an important alternative to traditional antibiotics with the aim of fighting bacterial resistance and nosocomial infections. With respect to the traditional techniques for coating deposition, plasma films are characterized by a higher level of adhesion, thus avoiding the requirement of substrate pre-treatment [15]. Moreover, the possibility to control coating thickness, even at nanoscale [18,19], enables the application of the techniques for flexible device treatment. Finally, thin deposited layers can be employed for the control of the antibacterial agent release, with the aim of triggering and regulating the coating functionalities.

Plasma deposited nanostructured coating can usually be divided into two main categories, depending on the film nature:

- matrix structured (Figure 1.2a), where NPs are directly embedded inside the coating;
- multilayer structured (Figure 1.2b), where NPs are incorporated between a polymeric sandwich film composed by a buffer and barrier layer.

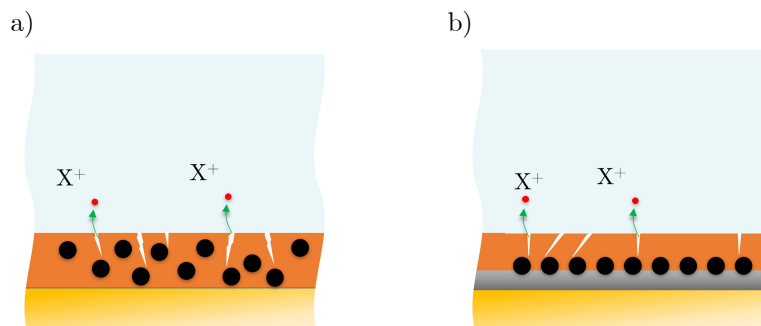


Figure 1.2 Nanostructured coating: a) matrix structure; b) multilayer structure.

From a technological point of view, these processes were firstly applied at low pressure in some pioneering works done by the groups headed by professor D'Agostino at the

University of Bari (Italy) and professor Biederman at Prague University (Czech Republic) [9,20]. Multilayer structured coatings are usually deposited in low pressure reactors through multi step processes where the particle synthesis is carried out by means of magnetron sputtering (Figure 1.3c) or gas aggregation sources (Figure 1.3d). The polymer deposition is often achieved exploiting gas phase reactions between the monomer and the plasma discharge or using a sputtering reactor equipped with a polymeric target (respectively Figure 1.3b and Figure 1.3a). At low pressure, the matrix structured deposition is usually performed by combining together the deposition and synthesis techniques described above, increasing the complexity of the system (Figure 1.3 e-g); the main advantage is that the process is single step and thus appears more attractive in the perspective of an industrial application. Achievements and limitations, with a particular focus on Ag based coatings, have been recently reviewed by Kratochvíl et al. [5]. Among the large number of published papers, it's worth highlighting the important achievements in the field obtained by Alissawi et al. [21,22]. With the aim of providing information about the effect of polymer nature on Ag ion release, the authors compared the antibacterial efficiency of different hydrophobic and hydrophilic coatings. According to the presented findings, the increase of water permeation in SiO<sub>x</sub> based coating (characterized by higher surface free energy) can be accounted as the major reason of the higher antibacterial effect with respect to hydrophobic films. However, a comparison with works recently published by Kylian [23] and Hegemann [13] points out that the antibacterial effect and cell adhesion of plasma deposited coatings are not only related to surface free energy, but also strongly influenced by the surface morphology (e.g. roughness, presence of cracks).

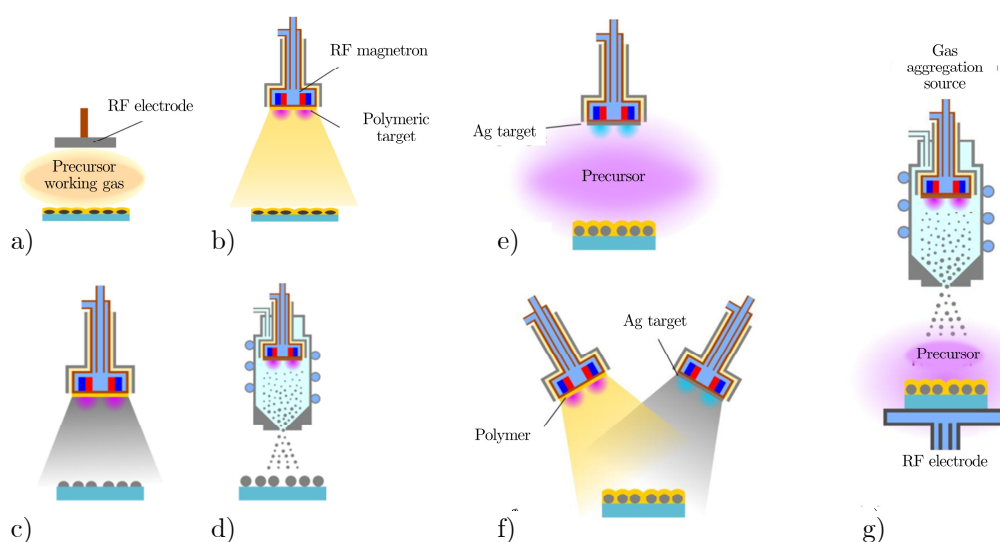


Figure 1.3 Low pressure plasma processes for the deposition of nanostructured coatings: a) gas phase deposition of polymeric coating; b) sputtering of polymeric target; c) sputtering of metal electrode; d) gas aggregation source for NPs synthesis. Codeposition of nanostructured coating: e) gas phase polymerization and metal sputtering; f) contextual sputtering of metal and polymer target; g) gas phase polymerization coupled with gas aggregation source. With permission from [5].

Even if still under investigation, following the promising results achieved with low pressure processes, recently the scientific community has moved its first step towards the use of atmospheric plasma sources to support coating deposition and particle synthesis. As with the low pressure processes, the employed approaches can be divided into matrix or multilayer strategies.

Deng et al. [24] firstly described the single step deposition of antibacterial coatings at atmospheric pressure on silicon substrates, exploiting the use of an aerosol as a carrier flow for Ag NPs and plasma gas phase reactions for the precursor polymerization. Interestingly, the authors outlined the formation of big clusters deposited on treated samples that can be ascribed to particle charging as recently discussed in literature [25]. By means of SEM and EDX techniques the clusters were found to be composed by an external coating shell characterized by the presence of cracks and pores. In their work, the authors suggested that the control of ions release, and therefore of the antibacterial effect, could be done tuning the surface characteristics of the coatings deposited on the Ag aggregates. Based on these findings and exploiting the presence of defects and cracks in the coating structure, the same research group developed a method for the deposition of multilayer coating where previously synthesized Ag NPs were embedded between two SiO<sub>x</sub> layers. While the deposition of the inorganic coating was performed by means of plasma assisted polymerization of hexamethyldisiloxane (HMDSO), the Ag NPs were deposited on the first coating layer using a dipping technique. Although great achievements were reported in terms of coating stability upon washing cycle and antibacterial properties, the presence of a wet stage in the coating manufacturing increased the complexity of the process in terms of NP processing.

Trying to overcome this limitation the scientific community has focused the attention on the development of process able to support the localized synthesis and deposition of nanostructured coatings. For this reason, in recent years plasma-droplet interaction has been proposed and used as an alternative to the processes described above with the aim of supporting in-situ and on-demand particle synthesis/delivery.

## **1.3 Plasma and droplets for biomaterial processing**

In the last few years, the possibility to couple the liquid aerosol injection in atmospheric pressure discharges has given birth to new approaches for the synthesis of NPs and the deposition of nanostructured coatings [26]. While on the one hand liquid aerosols could be employed as micro-carriers [27,28], able to deliver particles and molecules in the discharge region, on the other hand droplets introduced in the plasma discharge could act as micro-reactors [29] where reactions take place at the plasma-liquid interface (Figure 1.4).

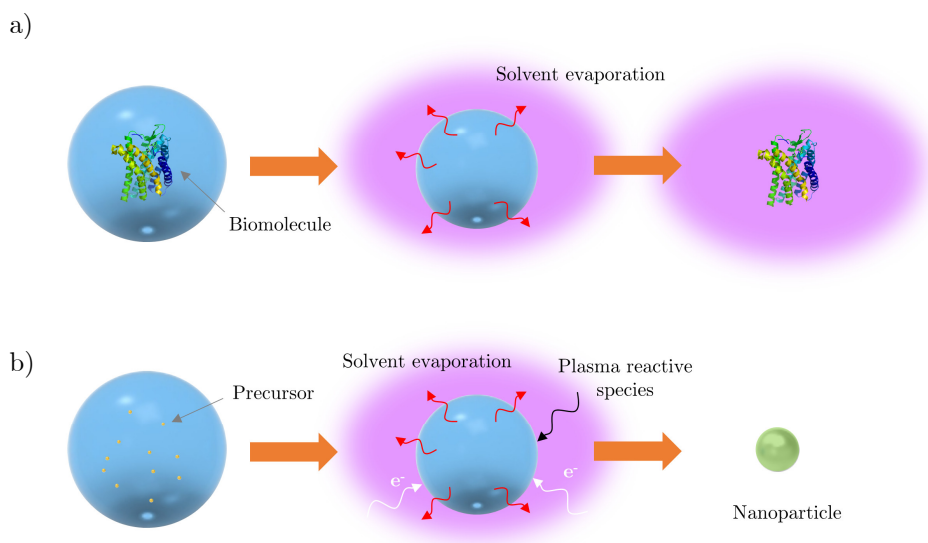


Figure 1.4 Approaches for droplet-plasma based processes: a) droplet used as microcarrier; b) droplet used as microreactor.

Concerning the former approach, our research group [30] developed an experimental setup for the nanostructured coating deposition where Ag NPs were introduced in the plasma discharge carried by an ethanol droplet flow. Contextually, the gas injected in the plasma jet was enriched with acrylic acid vapours, that were then used as a precursor for the polymerization and coating deposition. Due to the high solvent volatility, the liquid evaporation led to the presence of both Ag NPs and monomer vapour in the plasma discharge, enabling particle encapsulation in the polyacrylic acid deposited coating. While transmission electron microscopy analysis confirmed the nanostructured nature of the film, the preliminary biological results outlined a good level of antibacterial inactivation against *Escherichia coli*.

Exploring the possibility to inject drugs and biomolecules in the discharge, a pioneering work was recently presented by Palumbo et al. [28]. The authors discussed the introduction of gentamicin containing droplets in the plasma discharge, together with the injection of monomer vapour that was used to encapsulate the drug through the formation of a polymerized external shell. A strong correlation was found between the nanocapsule size and the power of the plasma discharge, suggesting a central role of evaporation rate in the particle nucleation [31].

Based on the widely reported possibility to synthesized nanoparticles from metal ions using plasma discharges in contact with liquids [32], Beier et al. [33] proposed to use droplet as microreactors, enabling the on-demand synthesis and in-situ deposition of Ag NPs. The developed approach, based on the reduction of a silver nitrate nebulized liquid flow, was applied for the co-deposition of an organic matrix structured coating using an atmospheric plasma jet. The strong antibacterial activity and good stability upon water washing outlined

challenging and promising perspectives for the localized functionalization of 3D biomaterials. Similar works were carried on also by Gerullis [34] and Zimmerman [35].

The use of droplet flow as microreactor to support the nanoparticles synthesis was recently reawakened by the interesting results achieved by Maguire et al. [29] on the in-flight and on demand synthesis of gold NPs. Coupling a nebulizer injector and a RF plasma discharge, the authors were able to produce NPs with a mean diameter of 4.4 nm.

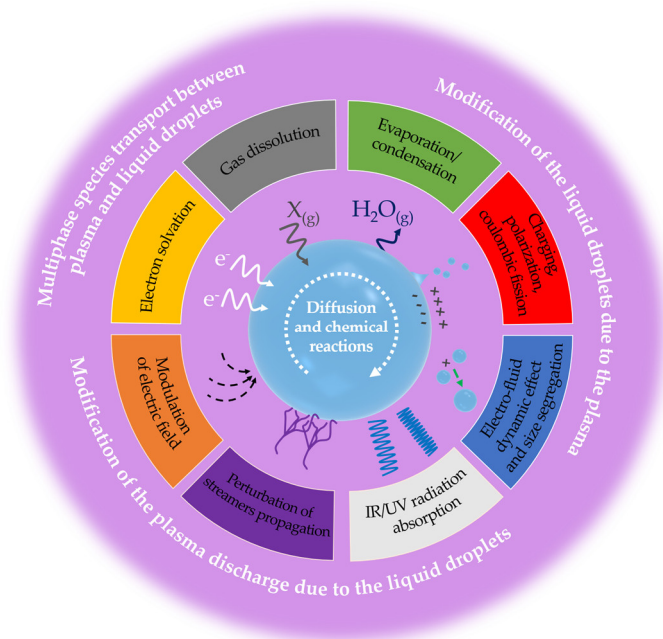


Figure 1.5 Different mechanism of plasma-droplet interaction inside an atmospheric pressure plasma discharge. With permission from [36].

Even if the results achieved outlined incredible perspectives for the development of plasma-droplet processes for biomaterial functionalization, the limited knowledge of the multiphase environment inside the discharge seems to have hindered a real control of process output. Perspectives and challenges of this field has been recently reviewed by an opinion paper with the aim of suggesting possible research activities aimed at filling the current knowledge gap (Figure 1.5) [36]. As far as the biomedical material processing is concerned, the possibility to tune particle morphology and chemistry with the aim of controlling coating functionalities and drug release is expected to be extremely important. Moreover, plasma sources can be specifically designed coupling aerosol injection devices thus enabling the direct functionalization of 3D biomaterials. Finally, it should be mentioned that the use of an in-flight synthesis approach will also improve the sustainability of the process thanks to a localized processing of NPs.

## 1.4 References

- [1] Katsikogianni M and Missirlis Y F 2004 Concise review of mechanisms of bacterial adhesion to biomaterials and of techniques used in estimating bacteria-material interactions *Eur. Cells Mater.* **8** 37–57
- [2] Desmet T, Desmet T, Morent R, Morent R, Geyter N De, Geyter N De, Leys C, Leys C, Schacht E, Schacht E, Dubruel P and Dubruel P 2009 Nonthermal Plasma Technology as a Versatile Strategy for Polymeric Biomaterials Surface Modification: A Review *Am. Chem. Soc.* **10**
- [3] D’Agostino R, Favia P, Oehr C and Wertheimer M R 2005 Low-temperature plasma processing of materials: Past, present, and future *Plasma Process. Polym.* **2** 7–15
- [4] Cvelbar U, Walsh J L, Černák M, de Vries H W, Reuter S, Belmonte T, Corbella C, Miron C, Hojnik N, Jurov A, Puliyalil H, Gorjanc M, Portal S, Laurita R, Colombo V, Schäfer J, Nikiforov A, Modic M, Kylian O, Polak M, Labay C, Canal J M, Canal C, Gherardi M, Bazaka K, Sonar P, Ostrikov K K, Cameron D, Thomas S and Weltmann K D 2019 White paper on the future of plasma science and technology in plastics and textiles *Plasma Process. Polym.* 16 1–37
- [5] Kratochvíl J, Kuzminova A and Kylián O 2018 State-of-the-art, and perspectives of, silver/plasma polymer antibacterial nanocomposites *Antibiotics* **7**
- [6] Sardella E, Favia P, Gristina R, Nardulli M and d’Agostino R 2006 Plasma-aided micro- and nanopatterning processes for biomedical applications *Plasma Process. Polym.* **3** 456–69
- [7] Da Ponte G, Sardella E, Fanelli F, D’Agostino R and Favia P 2011 Trends in surface engineering of biomaterials: Atmospheric pressure plasma deposition of coatings for biomedical applications *EPJ Appl. Phys.* **56** 1–4
- [8] Favia P and D’Agostino R 1998 Plasma treatments and plasma deposition of polymers for biomedical applications *Surf. Coatings Technol.* **98** 1102–6
- [9] D’Agostino R 1990 *Plasma Deposition, Treatment, and Etching of Polymers* ed R D’Agostino (Academic Press)
- [10] Milella A, Di Mundo R, Palumbo F, Favia P, Fracassi F and d’Agostino R 2009 Plasma nanostructuring of polymers: Different routes to superhydrophobicity *Plasma Process. Polym.* **6** 460–6
- [11] Sardella E, Gristina R, Senesi G S, D’Agostino R and Favia P 2004 Homogeneous and micro-patterned plasma-deposited PEO-like coatings for biomedical surfaces *Plasma Process. Polym.* **1** 63–72
- [12] Brétagnol F, Lejeune M, Papadopoulou-Bouraoui A, Hasiwa M, Rauscher H, Ceccone G, Colpo P and Rossi F 2006 Fouling and non-fouling surfaces produced by plasma polymerization of ethylene oxide monomer *Acta Biomater.* **2** 165–72
- [13] Hegemann D, Blanchard N E and Heuberger M 2016 Reduced Protein Adsorption on Plasma Polymer Films Comprising Hydrophobic/Hydrophilic Vertical Chemical

Gradients *Plasma Process. Polym.* **13** 494–8

- [14] Da Ponte G, Sardella E, Fanelli F, D’Agostino R, Gristina R and Favia P 2012 Plasma deposition of PEO-like coatings with aerosol-assisted dielectric barrier discharges *Plasma Process. Polym.* **9** 1176–83
- [15] Vasilev K, Griesser S S and Griesser H J 2011 Antibacterial surfaces and coatings produced by plasma techniques *Plasma Process. Polym.* **8** 1010–23
- [16] Chang Y Bin, Tu P C, Wu M W, Hsueh T H and Hsu S H 2008 A study on chitosan modification of polyester fabrics by atmospheric pressure plasma and its antibacterial effects *Fibers Polym.* **9** 307–11
- [17] Cloutier M, Mantovani D and Rosei F 2015 Antibacterial Coatings: Challenges, Perspectives, and Opportunities *Trends Biotechnol.* **33** 637–52
- [18] Morent R, De Geyter N, Van Vlierberghe S, Dubruel P, Leys C and Schacht E 2009 Organic-inorganic behaviour of HMDSO films plasma-polymerized at atmospheric pressure *Surf. Coatings Technol.* **203** 1366–72
- [19] Elam F M, Starostin S A, Meshkova A S, Van Der Velden-Schuermans B C A M, Van De Sanden M C M and De Vries H W 2017 Defect prevention in silica thin films synthesized using AP-PECVD for flexible electronic encapsulation *J. Phys. D. Appl. Phys.* **50**
- [20] Favia P, Vulpio M, Marino R, D’Agostino R, Mota R P and Catalano M 2000 Plasma-deposition of Ag-containing polyethyleneoxide-like coatings *Plasmas Polym.* **5** 1–14
- [21] Alissawi N, Peter T, Strunskus T, Ebbert C, Grundmeier G and Faupel F 2013 Plasma-polymerized HMDSO coatings to adjust the silver ion release properties of Ag/polymer nanocomposites *J. Nanoparticle Res.* **15**
- [22] Alissawi N, Zaporojtchenko V, Strunskus T, Hrkac T, Kocabas I, Erkartal B, Chakravadhanula V S K, Kienle L, Grundmeier G, Garbe-Schönberg D and Faupel F 2012 Tuning of the ion release properties of silver nanoparticles buried under a hydrophobic polymer barrier *J. Nanoparticle Res.* **14**
- [23] Kylián O, Kratochvíl J, Petr M, Kuzminova A, Slavínská D, Biederman H and Beranová J 2017 Ag/C:F Antibacterial and hydrophobic nanocomposite coatings *Funct. Mater. Lett.* **10** 3–6
- [24] Deng X, Leys C, Vujosevic D, Vuksanovic V, Cvelbar U, De Geyter N, Morent R and Nikiforov A 2014 Engineering of Composite Organosilicon Thin Films with Embedded Silver Nanoparticles via Atmospheric Pressure Plasma Process for Antibacterial Activity *Plasma Process. Polym.* 921–30
- [25] Chen X, Ghosh S, Buckley D T, Mohan Sankaran R and Hogan C J 2018 Characterization of the state of nanoparticle aggregation in non-equilibrium plasma synthesis systems *J. Phys. D. Appl. Phys.* **51** 335203
- [26] Fanelli F and Fracassi F 2013 Aerosol-Assisted Atmospheric Pressure Cold Plasma Deposition of Organic-Inorganic Nanocomposite Coatings *Plasma Chem. Plasma*

- [27] Ranieri P, McGovern G, Tse H, Fulmer A, Kovalenko M, Nirenberg G, Miller V, Fridman A, Rabinovich A and Fridman G 2019 Microsecond-Pulsed Dielectric Barrier Discharge Plasma-Treated Mist for Inactivation of Escherichia coli In Vitro *IEEE Trans. Plasma Sci.* **47** 395–402
- [28] Palumbo F, Treglia A, Lo Porto C, Fracassi F, Baruzzi F, Frache G, El Assad D, Pistillo B R and Favia P 2018 Plasma-Deposited Nanocapsules Containing Coatings for Drug Delivery Applications *ACS Appl. Mater. Interfaces* **10** 35516–25
- [29] Maguire P, Rutherford D, Macias-Montero M, Mahony C, Kelsey C, Tweedie M, Pérez-Martin F, McQuaid H, Diver D and Mariotti D 2017 Continuous In-Flight Synthesis for On-Demand Delivery of Ligand-Free Colloidal Gold Nanoparticles *Nano Lett.* **17** 1336–43
- [30] Liguori A, Traldi E, Toccaceli E, Laurita R, Pollicino A, Focarete M L, Colombo V and Gherardi M 2016 Co-Deposition of Plasma-Polymerized Polyacrylic Acid and Silver Nanoparticles for the Production of Nanocomposite Coatings Using a Non-Equilibrium Atmospheric Pressure Plasma Jet *Plasma Process. Polym.* **13** 623–32
- [31] Lo Porto C, Palumbo F, Fracassi F, Barucca G and Favia P 2019 On the formation of nanocapsules in aerosol-assisted atmospheric-pressure plasma *Plasma Process. Polym.* 1–7
- [32] Mariotti D and Sankaran R M 2010 Microplasmas for nanomaterials synthesis *J. Phys. D. Appl. Phys.* **43** 323001
- [33] Beier O, Pfuch A, Horn K, Weisser J, Schnabelrauch M and Schimanski A 2013 Low temperature deposition of antibacterially active silicon oxide layers containing silver nanoparticles, prepared by atmospheric pressure plasma chemical vapor deposition *Plasma Process. Polym.* **10** 77–87
- [34] Gerullis S, Pfuch A, Spange S, Kettner F, Plaschkies K, Küzün B, Kosmachev P V, Volokitin G G and Grünler B 2018 Thin antimicrobial silver , copper or zinc containing - SiO<sub>x</sub> films on wood polymer composites ( WPC ) applied by atmospheric pressure plasma chemical vapour deposition ( APCVD ) and sol – gel technology *Eur. J. Wood Wood Prod.* **76** 229–41
- [35] Zimmermann R, Pfuch A, Horn K, Weisser J, Heft A, Röder M, Linke R, Schnabelrauch M and Schimanski A 2011 An approach to create silver containing antibacterial coatings by use of atmospheric pressure plasma chemical vapour deposition (APCVD) and combustion chemical vapour deposition (CCVD) in an economic way *Plasma Process. Polym.* **8** 295–304
- [36] Stancampiano A, Galligani T, Gherardi M, Machala Z, Maguire P, Colombo V, Pouvesle J-M M and Robert E 2019 Plasma and Aerosols: Challenges, Opportunities and Perspectives *Appl. Sci.* **9** 3861

## **CHAPTER 2**

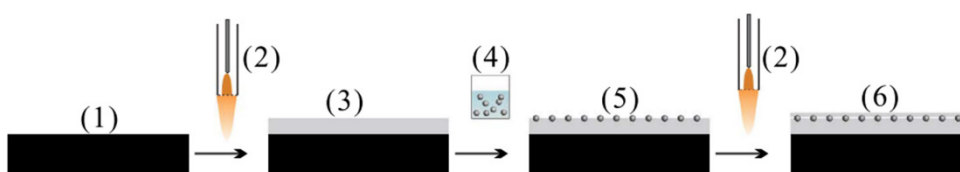
# **Non-thermal Plasma Assisted Deposition of Silver-Based Nanostructured Coatings to Prevent Biofilm Proliferation and Clot Formation**

## 2.1 Introduction

In the last decade, the urgent need of innovative solutions [1,2] able to meet the increase of hospital acquired infections (HAIs) [3] has triggered the efforts of several scientific communities working in the field of implantable biomedical devices [4–6] (e.g. central venous catheters, stents, prosthesis, grafts). Likewise, the prominent issue of drug resistance bacteria [7,8] affecting patient morbidity and mortality, has posed even more attention on the introduction of antibacterial functionalities to prevent biomaterials-related infections (BRIs). While the performances of new antibacterial compounds (e.g. silver, chitosan, enzyme, peptides) have been widely discussed [9], only recently the possibility to tailor biomaterials properties applying functional drug release coatings has received larger attention [10]. In this framework, developed from the pioneering works of Biederman [11], D’Agostino [12,13] and Yasuda [14], plasma assisted polymerization carried out at low and, recently, atmospheric pressure has been exploited with the aim of improving the surface properties of biomaterials [15]. It’s worth highlighting that the non-equilibrium chemistry, coupled with the low temperature of plasma functionalization enabled a wide tunability of coating characteristics and the treatment of almost all kind of thermo-sensitive materials. While a large number of works discussed possible applications of plasma deposited coatings to prevent antibacterial proliferation [16], to control cell adhesion [17] and to sustain localized drug delivery [18], only a few of them dealt with requirements for in-vivo applications. As discussed in the previous chapter, the traditional approach to support plasma assisted processing of antibacterial coating is based on the loading of nanoparticles (NPs, e.g. Ag, Cu) in a polymeric film deposited on a substrate, with the aim of avoiding particle leak and control bactericidal ion release. While low pressure setups are widely explored and reported [19],

researchers have recently improved atmospheric non-equilibrium plasma processes enabling the introduction or even the synthesis of nanoparticles in the gas discharge. Concerning the former approach, our research group recently reported on the possibility to use an ethanol aerosol flow as a carrier to enable the localized co-deposition of Ag NPs and polymeric coatings [20]. Although the deposited coating displayed promising performances in terms of antibacterial properties against *Escherichia coli*, the weak stability upon water immersion actually limited practical applications. With respect to the in-situ synthesis, Beier et al. [21,22] presented a novel approach for the deposition of water stable antibacterial coatings, where silver nitrate ( $\text{AgNO}_3$ ) containing droplets reacting in a plasma discharge were embedded in a  $\text{SiO}_x$  matrix. Even if the authors reported on coating stability upon washing cycles and ion release in liquid media, the lack of a biocompatibility assays limited possible scale up and *in-vivo* application of the technology. With the aim of preventing NPs dispersion in liquid environment and control the ions release, Deng and Nikiforov [23–25] discussed the key role of a barrier film deposited on non-woven fabrics were a reservation layer and Ag NPs were previously deposited through a three step process (Figure 2.1a). Unfortunately, even if the authors carried out a thorough investigation on the role of barrier layer thickness and cracks for silver ion release (Figure 2.1b), the use of a wet process for Ag NPs deposition seems to be poorly scalable. From an engineering point of view, the limited interaction between discharge and surface has enabled the treatment of small bidimensional samples, hindering further steps towards industrial applications. While the use of planar dielectric barrier discharge geometry seems promising only for the treatment of textile and films, recent developments in the development of plasma sources handled by computer numerical

a)



b)

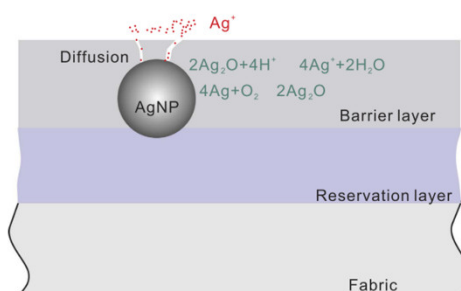


Figure 2.1 a) Nanostructured coating deposition of silver containing Ag NPs proposed by Deng and Nikiforov b) Suggested silver ion release mechanism. With permission from [24].

controlled (CNC) systems has enabled large-area treatment [26–28]. According to the state of the art, plasma assisted deposition of antibacterial coatings at atmospheric pressure has been applied only to 2D substrates and the treatment of 3D biomaterials has been limited to low pressure reactors [15]. Only recently, Omran et al. [29] deposited hydrophilic films on the internal wall of polymeric tubes, by means of transporting plasma discharges. While the achieved results have spurred plasma communities towards the development of plasma sources tailored for *in-situ* [30] material processing and several coating configurations and compositions have been explored [5,31], a comprehensive and multidisciplinary approach is required to shed some light on the role of coating characteristics on biological performances and compatibility.

In light of these issues, we carried out a wide study on silver-based atmospheric-pressure plasma deposited nanostructured coatings with the aim of investigate both the anti-biofilm performances and the biocompatibility properties of 2D and 3D treated materials. Since published data reported that 20-30% [32,33] of HAIs are currently related to the implant of central venous catheters (CVCs), we focused our attention on the development of a potential solution to prevent the incidence of catheter related bloodstream infections (CRBSIs) [33,34]. Beside septicaemia that is often related to medical device cross-contamination and multi-resistant biofilm formation [8], clot formation affects CVC implants , increasing the risk of thromboembolism [35,36]. In this framework, the aim of the presented work is to gain insight on the anti-biofilm properties of Ag NPs, preserving material hemocompatibility with a view for future applications. In-situ synthesis of Ag NPs was carried out through plasma assisted reduction of a AgNO<sub>3</sub> containing aerosol. Synthesized particles were embedded in a multilayer organic coating deposited on 2D polyurethane substrate already in use for medical device manufacturing and selected as a gold standard. Once completed the chemical and-morphological analysis of deposited coatings and assessed their stability, biological assays were carried out to evaluate the substrates biocompatibility and anti-biofilm performances. The promising performances of 2D treated biomaterials boosted further research activities, investigating the use of optimized process for mini catheter coating. After the analysis of coating stability upon ethylene oxide (EtO) sterilization and soaking, processed biomaterial functionalities were studied through *in-vivo* tests in animal models.

## 2.2 Materials & Methods

### 2.2.1 Plasma assisted deposition on 2D substrate

#### 2.2.1.1 Plasma source and process

Coating deposition and in-flight synthesis of Ag NPs were carried out by means of a single electrode atmospheric pressure plasma jet (APPJ) developed at the Alma Mater Studiorum-Università di Bologna, already studied and employed to support plasma assisted polymerization, nanostructured film deposition and liquid treatments (Figure 2.2) [20,37,38]. The plasma discharge was generated at the tip of the high voltage electrode where the primary argon (Ar) flow was introduced enabling the propagation of the plume through a small orifice. The plasma source was equipped with a specifically designed secondary gas diffuser suitable for the introduction of precursors directly in the plasma region. Gas flows were controlled by means of two mass flow controllers (El-Flow, Bronkhorst). The formation of a plasma plume at the exit of the plasma jet enabled the generation of a semi-controlled discharge, where the gas fluid dynamics was employed to limit ambient gas intake. A

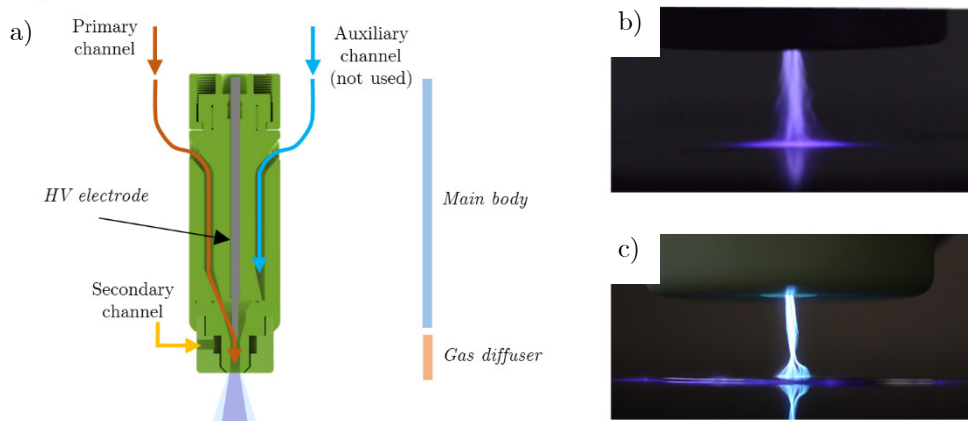


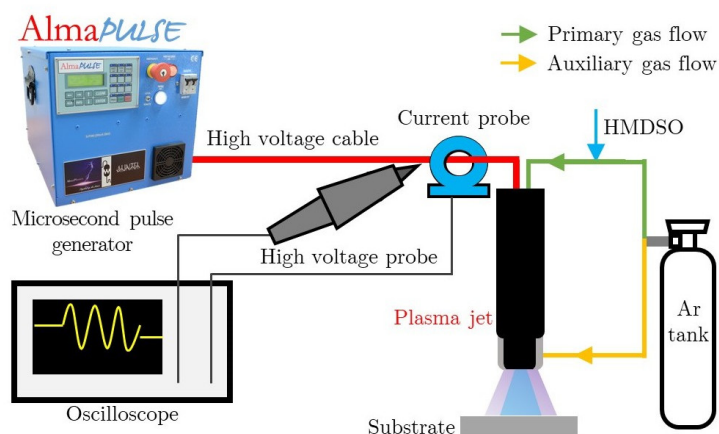
Figure 2.2 Plasma jet employed for the present study: a) Schematic; b) Plasma discharge on dielectric substrate; ; c) Plasma discharge on conductive substrate.

complete description of the gas fluid dynamics has been published by Colombo et al. [38,39]. The APPJ was driven by a commercial high voltage generator (AlmaPULSE, Almaplasma srl, Italy) working at 10 kV of peak voltage, with a pulse repetition frequency set at 14 kHz. Electrical characterizations of the plasma source were carried out measuring the voltage and current waveform along the high voltage cable by means of a high voltage probe (P6015A, Tektronix) and current probe (6585, Pearson). Real-time power measurements were performed processing the current and voltage waveforms acquired using an oscilloscope (DPO4043, Tektronix) connected to a computer through in-house developed MatLab® script. Power delivered to the plasma source was calculated by integration of instantaneous power along the period taking into account a large number of acquisitions (~450). A

schematic of the experimental setup used for coating deposition and particle synthesis are reported in Figure 2.3a and Figure 2.3b, respectively.

Nanostructured coating deposition was carried out in three different process stages (Figure 2.4) that allowed the embedment of plasma synthesized Ag NPs between a buffer layer and a barrier layer able to prevent particles release and dispersion in the liquid phase. A first buffer layer was deposited on polyurethane samples introducing 0.2 g/h of

a)



b)

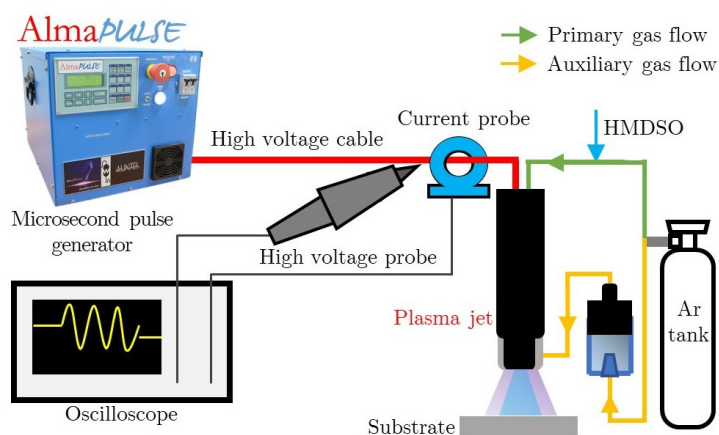


Figure 2.3 Schematic of setup used for the deposition of coating (a) and synthesis of Ag NPs(b).

hexamethyldisiloxane (HMDSO, Sigma Aldrich) carried in the plasma discharge by 1.7 liter per minute (l/min) flow of Ar. An Ar flow of 2.4 l/min was introduced through the secondary gas diffuser, with the aim of increasing the discharge volume and, thus, the deposition area.

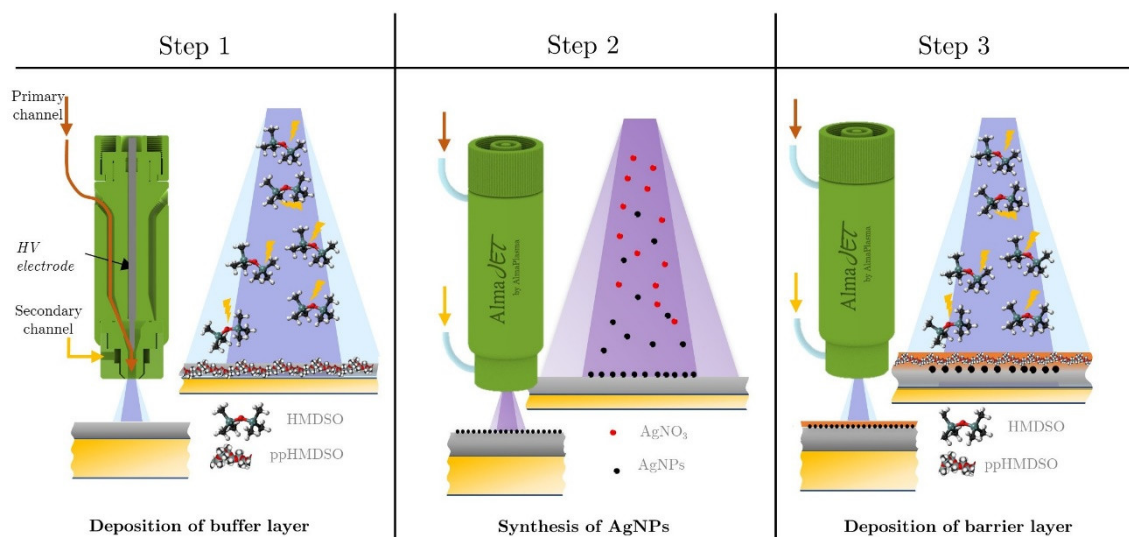


Figure 2.4 Schematic of plasma process for nanostructured coating deposition: a) deposition of the buffer layer; b) in-flight synthesis and deposition of Ag NPs; c) deposition of the barrier layer.

The deposition of the buffer layer lasted 60 seconds. Afterwards, Ag NPs synthesis was performed injecting in the plasma region silver nitrate ( $\text{AgNO}_3$ ) containing droplets carried by 2.4 l/min flow of Ar: the aerosol was introduced in the discharge through the secondary diffuser. The concentration of the nebulized solution was kept constant at 250 mM for all the experiments: the solution was prepared dissolving  $\text{AgNO}_3$  in distilled water (Sigma Aldrich, HPLC grade) and stirring for 15 minutes at room temperature. Finally, the deposition of the barrier layer was carried out in the same operating condition used for the buffer layer deposition. The in-flight Ag NPs synthesis and barrier layer deposition lasted 300 and 30 seconds, respectively. A summary of all the operating conditions and parameters used in the experiments is reported in Table 2.1

	Buffer layer deposition	Ag NPs synthesis and deposition	Barrier layer deposition
<i>Primary gas flow</i>			
Ar flow rate	1.7 l/min	1.7 l/min	1.7 l/min
HMDSO flow rate	0.2 g/h	-	0.2 g/h
<i>Secondary gas flow</i>			
Ar flow rate	2.4 l/min	2.4 l/min	2.4 l/min
Precursor	-	250 mM $\text{AgNO}_3$ aerosol	-
Treatment time	60 s	300 s	30 s
Plasma power	11.7 $\pm$ 0.2W	9.2 $\pm$ 0.2 W	11.7 $\pm$ 0.2W

Table 2.1 Operating conditions used for plasma assisted coating deposition and Ag NPs synthesis.

Deposition of multilayer films were performed on polyurethane substrates widely employed in the biomedical field for the manufacturing of medical devices. It's worth

mentioning that usually central venous catheters (CVCs) are loaded with barium sulphate ( $\text{BaSO}_4$ ) NPs to ensure radiology detection of the medical device once placed inside the body. For this reason, coatings were deposited on polymeric plates ( $30 \times 30 \times 3 \text{ mm}^3$ ) produced by a moulding process and loaded with  $\text{BaSO}_4$ . Pristine substrates were placed 7 mm below the plasma source and exposed to the plasma discharge. Expanding from the APPJ orifice, the interaction of the plasma discharge and the treated substrate took place up to  $\sim 7$  mm in the radial direction from the tip of the electrode (as can be observed in the pictures reported in the next paragraph and in literature [40,41]), leading to a deposition area of  $\sim 150 \text{ mm}^2$ .

#### **2.2.1.2 Chemical and morphological characterization**

While chemical characteristics of the coatings were analyzed by means of Fourier transform infrared spectroscopy in ATR mode (ATR-FTIR, Agilent Cary 660), substrate morphological characteristics were investigated using a scanning electron microscopy and energy dispersive X-ray microanalysis (SEM-EDX, Phenom G2 ProX) on preliminary gold palladium sputter coated samples (SC7620 mini sputter coater, Quorum Technologies). Static contact angle (CA) measurements were performed by means of drop shape analyser (DSA30, KRUSS): a distilled water droplet ( $2 \mu\text{l}$ ) was deposited on the sample substrate and the contact angle was measured using the Young-Laplace method.

#### **2.2.1.3 Water stability test**

According to ISO-10993-13 [42] and ISO-3781 [43], the stability of deposited coatings was assessed through the immersion of the treated samples in 50 ml of phosphate-buffered saline solution (PBS) for 7 days in a shaking plate incubator at  $37^\circ\text{C}$ . After stability tests, coating morphological and chemical characteristic were investigated using ATR-FTIR, SEM and CA analysis. For each characterization technique, the analyses were carried out on two replicates.

#### **2.2.1.4 In-vitro biological assay**

All biological assays were carried out in cooperation with the Technopole of Mirandola, where the author personally performed the experiments and analyzed the results.

With the aim of evaluating the hemocompatibility of the deposited coatings, dynamic blood contact tests were performed: plasma treated substrates were dipped in human blood and incubated at  $37^\circ\text{C}$  for 24 hours using an orbital shaker. Cell lysis of blood samples was evaluated by haemoglobin free assay (Haemoglobin Assay Kit Sigma MAK115) according to ISO10993-4 [44]. The value of free haemoglobin (freeHGB) was then calculated through a calibration curve, as suggested by the assay procedure. After blood contact test, biomaterials were stained with haematoxylin/eosin: substrates were fixed in formalin (10% v/v, 15 minutes), stained with haematoxylin, washed with tap water, counterstained with eosin (20 seconds) and finally washed in double distilled water (ddH<sub>2</sub>O).

Antibiofilm performances were evaluated by soaking the treated substrates in a four strains broth bacterial culture (*Bacillus subtilis*, *Staphylococcus aureus*, *Pseudomonas aeruginosa*, *Enterococcus hirae* 1:1:1:1,  $10^8$  CFU/ml) for 10 days at 37°C. According to the methodology proposed by Petrachi et al. [45], crystal violet (CV) staining was used to estimate biofilm adhesion and proliferation on the coated biomaterials: substrates were fixed in methanol (-20°C) for 2 minutes, washed in ddH2O and dipped in crystal violet (0.4%) for 5 minutes.

After substrate staining procedures, clots and biofilm formation was evaluated by means of stereo microscope imaging (Microscope for Large Fields AxioZoom V16, Carl Zeiss Microscopy GmbH). All the analyses were carried out on three biological replicates.

## 2.2.2 Plasma assisted deposition on mini catheters

### 2.2.2.1 Plasma process

Following the promising results achieved in terms of anti-biofilm and anti-clot properties with respect to the 2D substrates, polyurethane mini catheters (50 mm length, OD 0.8 mm, ID 0.4 mm) were coated using the plasma assisted process previously described. The treatment of the sample was performed using a specifically designed holder, able to guarantee the processing of the entire catheter surface. Process was carried out following the three steps reported below:

1. Step 1: Deposition of buffer layer coating (60 s) for each side of the catheter, rotating the substrate by 90° every 60 s (total treatment time 4 x 60 s);

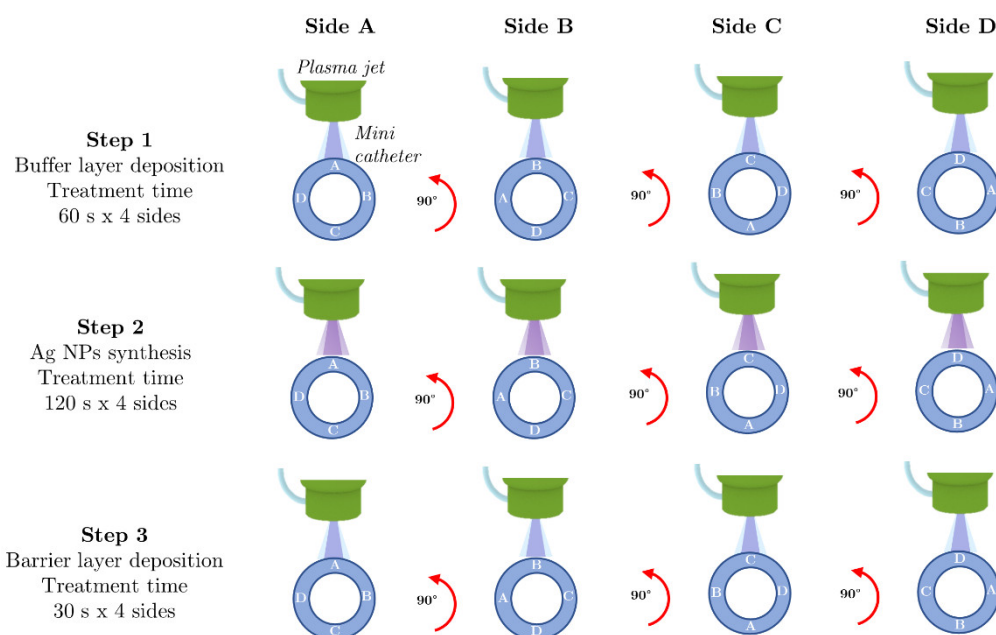


Figure 2.5 Schematic of the deposition of nanostructured coating deposition performed on mini catheters.

2. Step 2: Synthesis and deposition of Ag NPs (120 s) for each side of the catheter, rotating the substrate by 90° every 120 s (total treatment time 4 x 120 s);
3. Step 3: Deposition of barrier layer coating (30 s) for each side of the catheter, rotating the substrate by 90° every 60 s (total treatment time 4 x 30 s);

While the operating condition for the three different steps has been already reported above in this dissertation (Figure 2.4 and Table 2.1), a brief schematic of the deposition process is reported below (Figure 2.5). The deposition of multilayer coatings (buffer layer deposition, Ag NPs synthesis, barrier layer deposition) was performed in two different spots along the length of the mini catheter, located respectively at 10 mm and 30 mm from its tip (Figure 2.6).

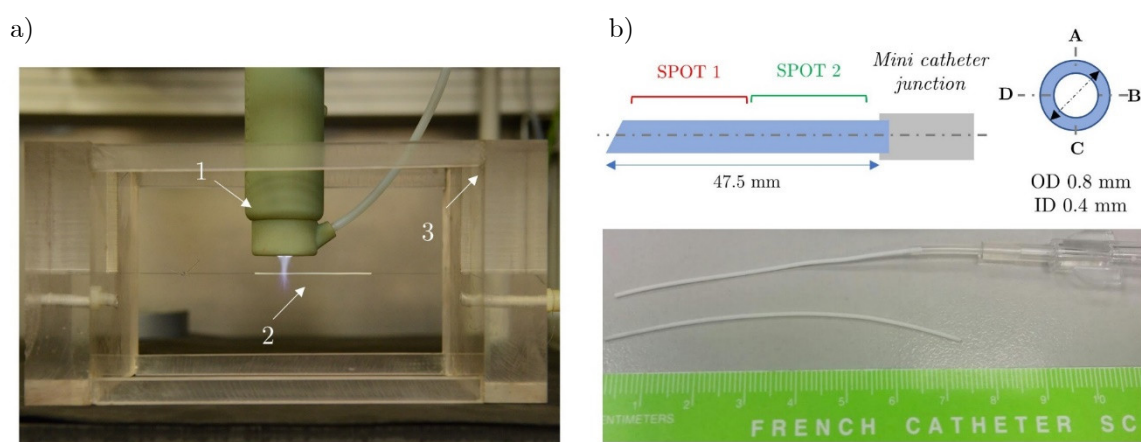


Figure 2.6 Plasma process for the deposition of nanostructured coating on mini catheters: a) coating deposition on mini catheter (1 Corona Jet, 2 Mini catheter, 3 Sample holder); b) schematic and picture of the used mini catheter.

The distance between the plasma source and the catheter was kept constant at 7 mm. The treatment time was set to 60 seconds and 30 seconds respectively for buffer layer and barrier layer deposition. Ag NPs were in-flight synthesized introducing 250 mM of AgNO<sub>3</sub> aerosol containing droplets inside the plasma discharge for 120 s.

### 2.2.2.2 Chemical and morphological characterization

After deposition, the treated catheters were sterilized using ethylene oxide (EtO): the sterilization process lasted for 20 hours and was performed at 44°C in a 10% ethylene oxide and 90% CO<sub>2</sub> atmosphere. Coating stability upon sterilization and immersion in tryptic soy broth (TSB) solution (72 hours at 37°C) was assessed by means of SEM analysis. Furthermore, microanalysis was employed to qualitatively confirm the presence of embedded Ag NPs after sterilization and stability test.

### 2.2.2.3 *In-vitro* biological assay

Finally, *in-vitro* compatibility of treated mini catheters was assessed by MTT test according ISO 10993-5[46]: after biomaterial elution in cell culture medium for 24 hours at 37°C, the eluate was added to L292 culture and cell viability was assessed by colorimetric

evaluation through MTT reduction (Microplate Reader, Perkin Elmer). As suggested by the standard, latex and high-density polyethylene (HDPE) were used as positive and negative controls, respectively.

#### **2.2.2.4 *In-vivo* biological assay/ 1**

Anti-biofilm performances of treated mini catheters were evaluated by means of *in-vivo* mouse models using the experimental approach reported by Kucharíková et al. [47]. Briefly, sterilized samples (length 0.5 mm) were coated with fetal bovine serum (FSB), soaking the catheters overnight at 37°C in serum solution (1.8 ml, 100% for each catheter). Contaminated medium ( $5 \times 10^4$  cells/ml) was prepared suspending BioLuminescent (BL) *Pseudomonas* cells in 1 ml of phosphate buffer solution (PBS) and performing serial dilutions. BL bacteria were engineered using luciferase gene that reacting with coelenterazine produces light emission. FSB coated catheters were incubated at 37°C for 90 minutes. Samples were then gently washed with 1 ml of PBS. For each animal model, three contaminated catheters were introduced in a subcutaneous tunnel created on the back of mice under anaesthesia. Non-invasive bioluminescent imaging (BLI) techniques was then used to monitor bacteria and biofilm growth, measuring luciferase light intensity.

All the procedures involving animals and their care were conducted in conformity with national and international laws and policies and were approved by Italian Ministry of Health through the Ethical Committee (1017/2015\_Pr 23/9/2015).

#### **2.2.2.5 *In-vivo* biological assay/ 2**

With the aim of further investigating the future potential of the developed approach to prevent biofilm adhesion on medical devices, tests were carried out of evaluating the biocompatibility of the treated mini catheters in *in-vivo* model. Six animal models for each tested condition were employed. Following the approach proposed by Feng et al. [48], EtO sterilized catheters were implanted on rat jugular vein and blood tests were carried out during the 30 days of implant. Among the others, it's important to highlight that inflammatory status was investigated through the analysis of granulocyte, lymphocyte, monocyte concentrations. Moreover, rat weight was measured with the aim of highlighting possible animal discomfort. After the explant of the implanted mini catheters, samples were gently washed and stored in ethanol until the SEM morphological analysis. Due to surgical procedures, it was possible to analyze only 10 mm of the removed mini catheters and no information on the catheter section (47.5 mm length) was possible. Nevertheless, preliminary hypothesis regarding coating stability and performances were carried out.

All the procedures involving animals and their care were conducted in conformity with national and international law and policies and were approved by Italian Ministry of Health through the Ethical Committee (65/2018-PR, prot. CBCC2.0, 24/10/2017).

## 2.3 Results & Discussion

### 2.3.1 Plasma assisted coating deposition on 2D substrate

Electrical power delivered to the APPJ was measured during all the steps of the multilayer coating deposition. Recorded data, reported in Table 2.1, outlined that the coating deposition took place at higher power value (11.7 W) with respect to the Ag synthesis step (9.2 W). The slight decrease of plasma power for NPs synthesis phase can be ascribed to the presence of water vapour that increased the breakdown voltage, thus limiting the energy that can be transferred to the gas phase. Even if the voltage-current waveform, reported in Figure 2.7a/c, were characterized by similar trends, it's important to highlight that the discharge appearances for the two phases are different: while a glow-like discharge was achieved when the HMDSO precursor was introduced in the plume (Figure 2.7b), the synthesis process was characterized by a filamentary discharge where streamers propagated from the electrode tip to the substrate (Figure 2.7d). As reported in literature [49], the presence of vapour molecules during the deposition process decreases the electron temperature and increases the energy transferred to heavier species through collisions, enabling the transition to glow-like discharges [50,51]. Conversely, Tardiveau et al. [52] reported that the introduction of droplets in the plasma discharge can locally affect the

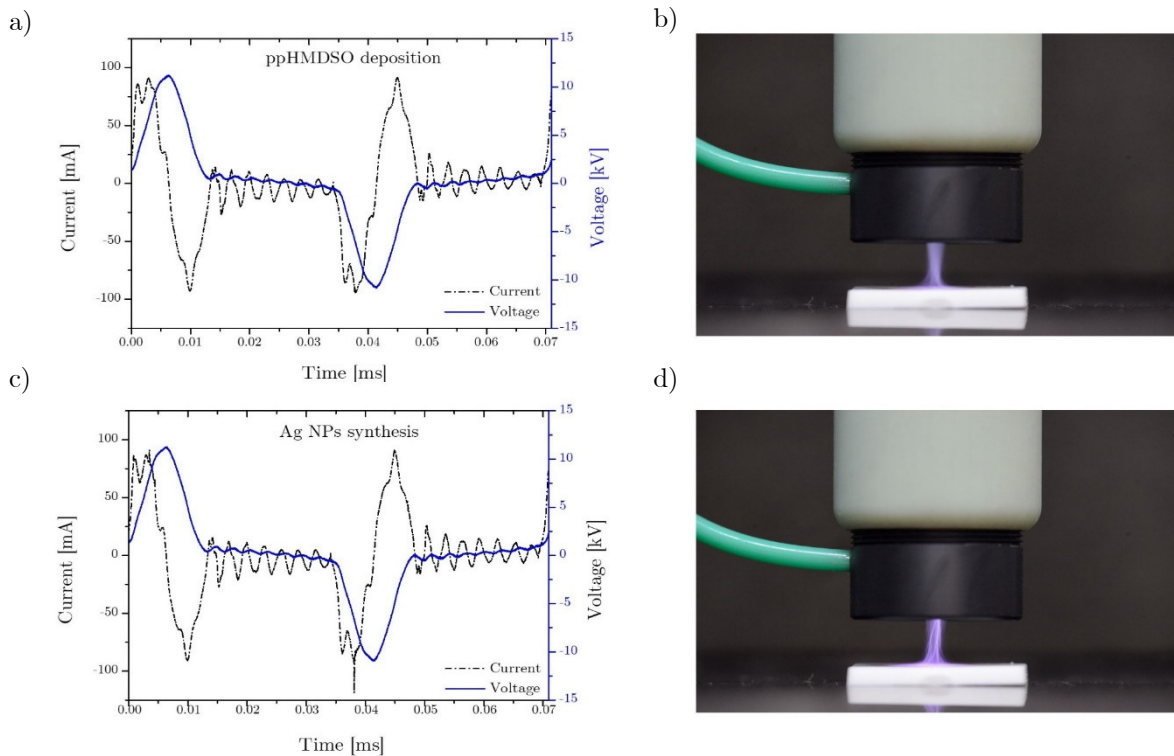


Figure 2.7 Voltage-current waveforms and picture of the plasma discharges during ppHMDSO deposition (a,b) and Ag NPs synthesis (c,d).

electric field, allowing the formation of streamers at lower voltage and affecting the discharge propagation.

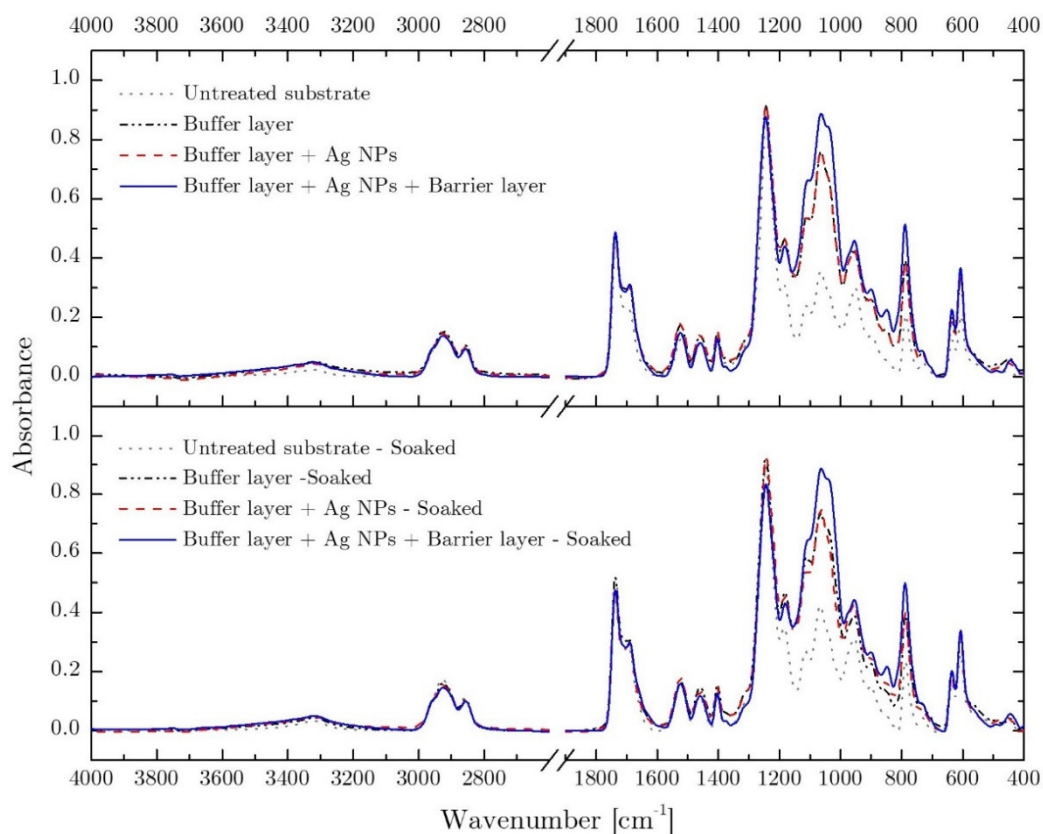
In order to investigate the chemical and morphological properties of deposited coatings, ATR-FTIR analyses were performed after each deposition/synthesis step (Figure 2.8a). A brief analysis of pristine sample spectrum highlighted the presence of CH<sub>2</sub> (2864 cm<sup>-1</sup>), C-O (1713 cm<sup>-1</sup>) and N-H/C-N (1241 cm<sup>-1</sup>) bands, thus confirming the polyurethane structure of the material. With respect to that, the treated samples on which a buffer layer was deposited exhibited a characteristic peak centred at 1020 cm<sup>-1</sup> that can be ascribed to Si-O-Si stretching vibrational mode [53]. The lower absorption bands at 445 cm<sup>-1</sup> and 790 cm<sup>-1</sup> were related to Si-O-C asymmetric and Si-CH<sub>3</sub> rocking vibration [54]. While the deposition of Ag NPs did not affect the IR spectrum of the buffer layer, the deposition of the barrier layer led to higher absorbance value; in line with the presence of a thicker coating [55]. Although the presence of characteristics organo-silicon peaks confirmed the deposition of plasma polymerized HMDSO with a retention of C bonds [56,57], the IR spectrum of untreated material partially covers the organic characteristics peaks usually used to fully address organic-inorganic properties of the coating [57]. For this reason, to gain insight into the chemical composition of the coating, water CA measurements were carried out. Obtained data, reported in Table 2.2, highlighted that deposited coatings were characterized by higher contact angle (lower surface energy) with respect to the pristine substrate. Even if not statistically significative, the increase of contact angle of the sample where Ag NPs were deposited on the buffer layer can be ascribed to changes in surface morphology, as reported by Yuce et al. [58] and accordingly to Wenzel [59]. Finally, the deposition of the barrier layer further decreased the surface energy leading to a CA of 101°. The hydrophobic behaviour of the deposited coating, together with the presence of CH<sub>3</sub> bonds highlighted in IR spectra, supported the hypothesis of the deposition of organic coating, characterized by a good retention of CH functionalities. Achieved results are in line with what was reported by Morent et al. [53] that discussed the deposition of organic and inorganic HMDSO plasma polymerized coating. The authors reported on the different wettability of coatings deposited through plasma polymerization of HMDSO in an oxygen-free environment (CA~100°) with respect to the ones processed when oxygen/air was added to the discharge (CA~20°). The presence of oxygen molecules indeed increases the fragmentation of the monomer and enables the formation of higher number of O-Si-O bonds, leading to inorganic and wettable films. Since our process was carried out in “semi-controlled” environment where the presence of

	<b>WCA</b>
Untreated substrate	75.1 ± 2.3 °
Buffer layer	95.5 ± 1.9 °
Buffer layer + Ag NPs	99.2 ± 3.1 °
Buffer layer + AgNPs + Barrier layer	101.4 ± 0.7 °
Buffer layer+ Barrier layer	98.8 ± 3.1 °

Table 2.2 WCA of deposited coatings.

ambient air (and therefore oxygen) was limited control thanks to gas fluid dynamics, the high CA obtained for coated substrates confirmed the organic PDMS-like nature of deposited coatings.

a)



b)

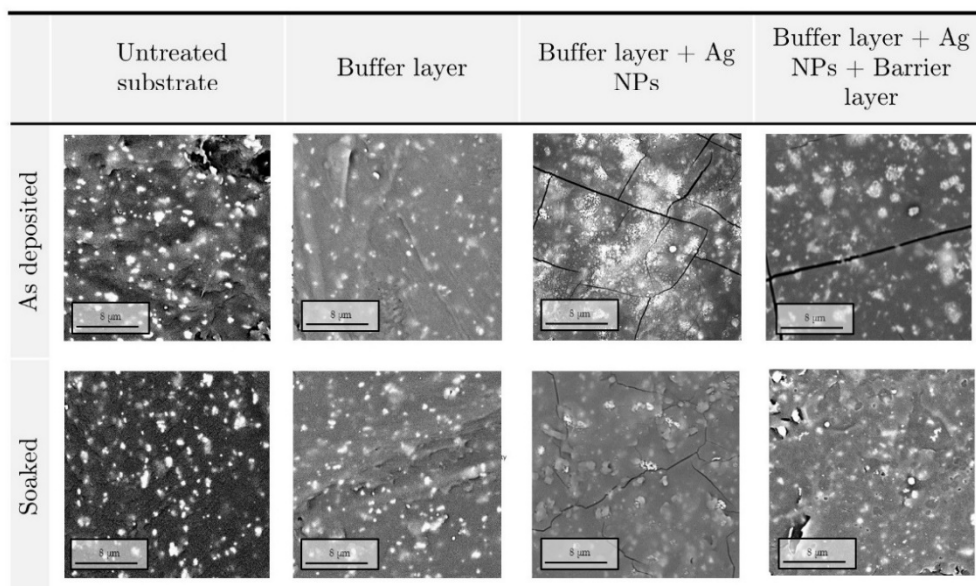


Figure 2.8 ATR-FTIR (a) and SEM (b) analysis of deposited coatings before and after stability test.

Chemical and morphological analysis were completed investigating the surface characteristics of deposited coatings using SEM and microanalysis techniques. As reported in Figure 2.8b, the presence of defects resulting from the moulding process increased the surface roughness of the pristine sample. Moreover, the picture outlined the presence of BaSO<sub>4</sub> particles, confirmed by EDX microanalysis (Figure 2.19, Appendix). When the buffer layer was deposited on the untreated samples, they exhibited a smoother surface, consistent with polymeric film deposition. The presence of Ag NPs after the synthesis step was confirmed both from SEM and EDX analysis. In particular, Ag NPs deposited on the buffer layer were widely spread on all the treated samples and were characterized by nanometric dimension. Nanostructure dimensions were analyzed by means of a high-resolution SEM-FEG, able to reach higher magnification and better resolution with respect to the desktop SEM used for coating analysis. Microscopy analyses were carried out on Ag NPs deposited on glass slides (with the aim of removing pristine substrate background morphology) and highlighted the synthesis of NPs with a broad particle sized centred at 28.4 nm (Figure 2.9). Moreover, even if not fully detectable because of limited instrument resolution, the presence of small particle (<10 nm) was found. The morphology of particles synthesized and deposited on the sample was in line with what was reported by Hong et al. [60]. Droplets to particles conversion in plasma flow-through reactor is still unexplored and different studies are currently ongoing with the aim of deeper investigate the synthesis process.

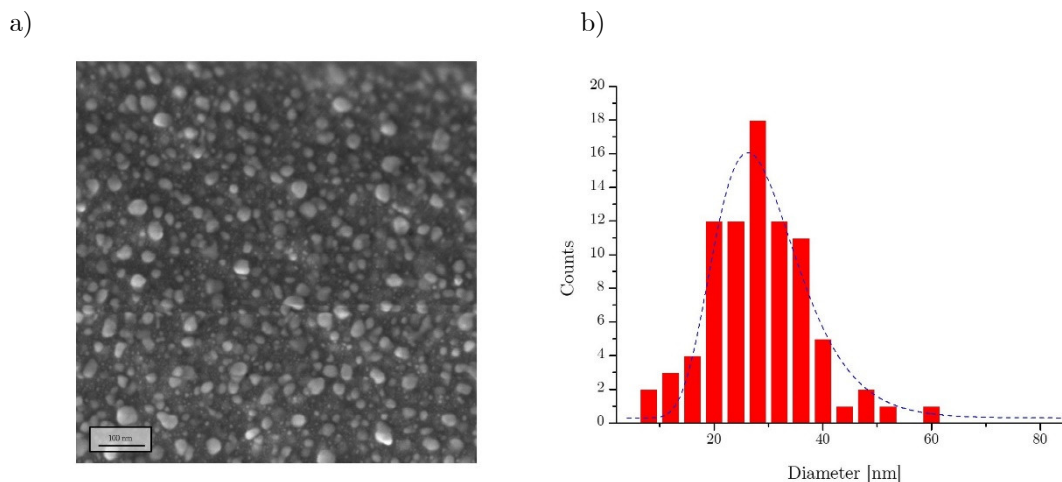


Figure 2.9 FE-SEM image of Ag NPs deposited on glass slide (a) and synthesized particle distribution (b).

To prevent nanoparticles dispersion in the biological environment, a polymeric barrier layer was deposited on Ag NPs. The SEM analysis outlined that the coating embedded the deposited particles in the ppHMDSO matrix. A deeper morphological analysis of the coating after Ag NPs synthesis and barrier layer deposition revealed the presence of cracks. With the aim of providing insight on cracks formation these results were compared with the control experiment where only buffer and barrier layer were deposited. Results (buffer layer + barrier layer, Figure 2.10) outlined the lack of cracks where only polymeric coating were

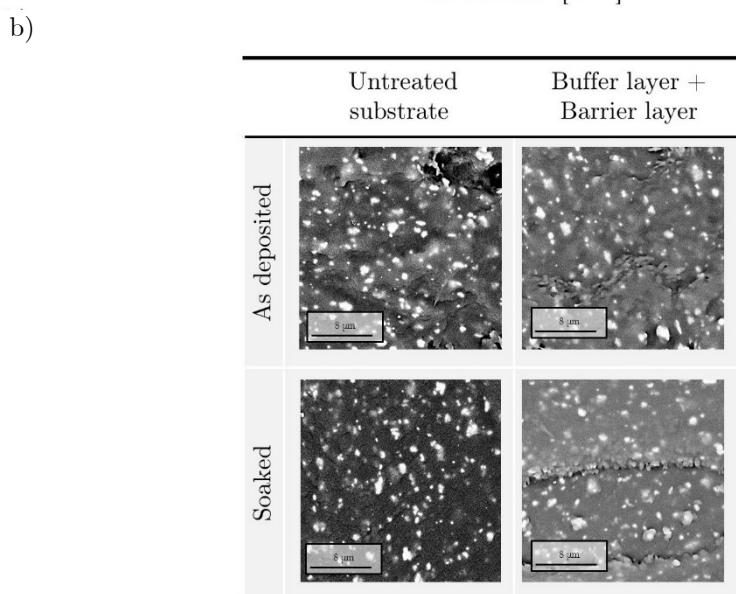
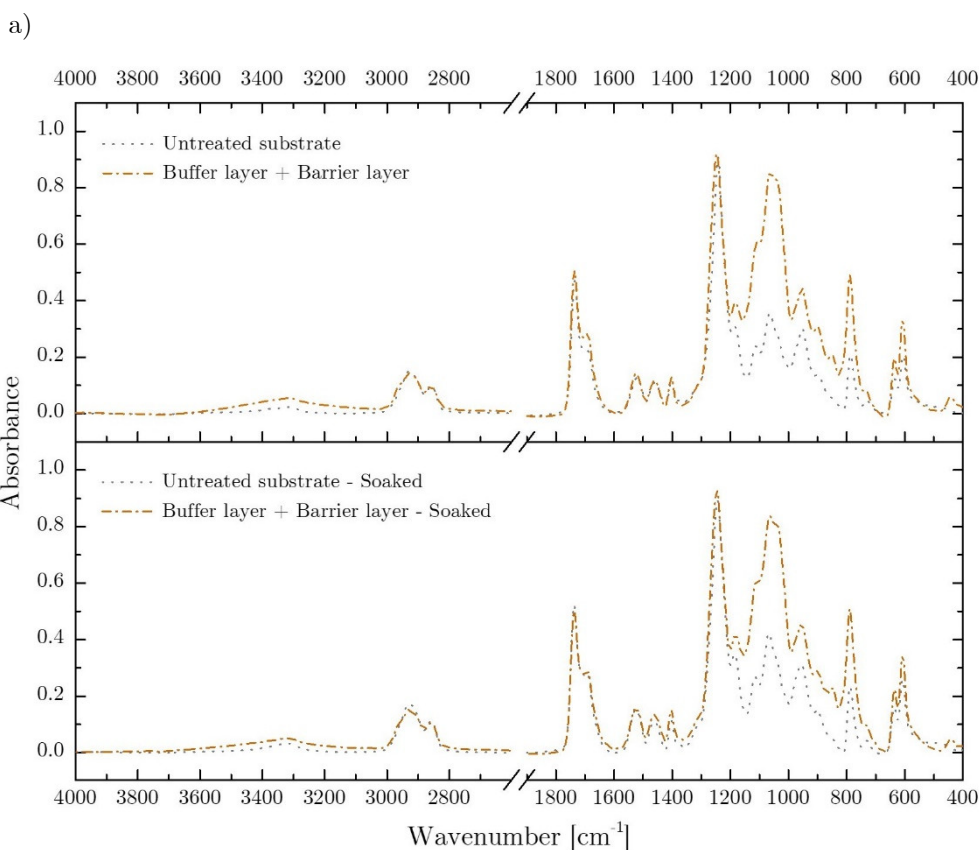


Figure 2.10 ATR-FTIR (a) and SEM (b) analysis of buffer layer + barrier layer sample before and after stability test.

deposited, suggesting that the presence of cracks was mainly due to the synthesis phase. A possible explanation of the cracks formation can be ascribed to the higher discharge temperature when water droplets (and water vapour) were introduced in the discharge [61]: indeed thermal stress of the deposited coatings and treated substrates could have induced crack and defect production [62]. Even if defects of plasma coating deposition are usually undesired [63,64], Nikiforov et al. [24,25] reported on the key role of cracks for the delivery of silver ions from nanostructured films deposited on non-woven fabrics.

As far as coating thickness is concerned, the high surface roughness of untreated sample ( $R_a = 1.77 \mu\text{m}$ ) hindered the possibility to have information about the deposition rate through atomic force microscopy or profilometer analysis. Published literature suggests that in similar plasma configuration and precursor concentration, the deposition rate was in the range of 220 nm/min [65].

In the perspective of an *in-vivo* application, beside antibacterial properties, deposited film should exhibit stability towards delamination, that is known to be responsible for medical devices failure and medical complications. For this reason, according to regulations [42,43], we investigated coating stability upon liquid solution immersion. IR spectra (Figure 2.8a) collected from treated samples after 7 days of stability test at 37°C outlined a limited reduction of coating characteristic peaks with respect to each *as deposited* film. While the presence of Si-O-Si, Si-O-C Si-CH<sub>3</sub> highlighted the stability of plasma polymerized coatings, the small reduction in peak absorbance can be related to morphological surface modification due to liquid permeation, generally described as swelling [66]. This hypothesis was supported by the result of SEM analyses which outlined changes in coating morphology. After the prolonged soaking in the liquid solution, the buffer and barrier layers displayed a slight variation of the superficial roughness, leading to smooth and swollen surface. The key role of the barrier layer can be highlighted comparing the SEM images and EDX results of Ag NPs deposited coatings with and without the upper protective layer. The presence of the barrier layer prevents the dispersion of Ag NPs in the liquid environment, maintaining a high level of Ag retain after immersion while controlling the Ag ions release, as already discussed in the literature [24,67,68].

Following the assessment of coating stability, the biological performances of plasma treated sample were assessed by means of dynamic blood contact test and biofilm adhesion assay. In this framework, we tested the properties of three different types of substrates: beside untreated samples, anticlot and antibiofilm performances were analyzed on polymeric (buffer layer + barrier layer) and nanostructured (buffer layer + Ag NPs + barrier layer) coatings. In this way, we separately investigated the role of Ag NPs with respect to the polymeric matrix. It's also worth remembering that the untreated substrate is already in use for the production of medical devices (in particular of central venous catheters) and can be thereafter used as a reference gold standard.

The dynamic blood contact test was used to investigate both the hemocompatibility and the surface clot formation of deposited coatings, in the perspective of future *in-vivo* assay and application. While blood coagulation induced by shear forces between biomaterials surface and liquid phase should be kept under control to prevent thrombosis [69], clots formation has been reported as one of the major causes of device failure [35] and biofilm proliferation [70]. For this reason, after 24 hours of contact with treated biomaterials, the free haemoglobin (freeHGB) content of blood samples was assessed using a colorimetric technique. It's worth remembering that higher content of free haemoglobin can be related to red cell lysis and to a higher coagulation rate. As reported in Figure 2.11, the deposition of the only polymeric coating (buffer layer+barrier layer) reduced the cell lysis and therefore increased the hemocompatibility of the treated samples. Conversely, the introduction of the Ag nanoparticles in deposited coatings (buffer layer + Ag NPs + barrier layer) displayed the same level of blood haemolysis of untreated substrate, our gold standard. Generally, obtained results showed that blood contact with treated and untreated substrates increase the freeHGB content. A possible explanation of the different haemolysis rate can be carried out, following what has been already reported in literature; according to what was discussed by Offeman [71], the dynamic contact between biomaterial and blood increases red cells stress and induces the haemolysis. More recently, other studies [72,73] highlighted that, beside shear forces, also surface roughness has an important effect on haemolysis rate. These findings supported the achieved experimental results and can also explain the decrease of freeHGB when the polymeric coating was applied to the pristine substrate: the decrease in surface roughness, as discussed previously, can be accounted for the reduction of the shear-

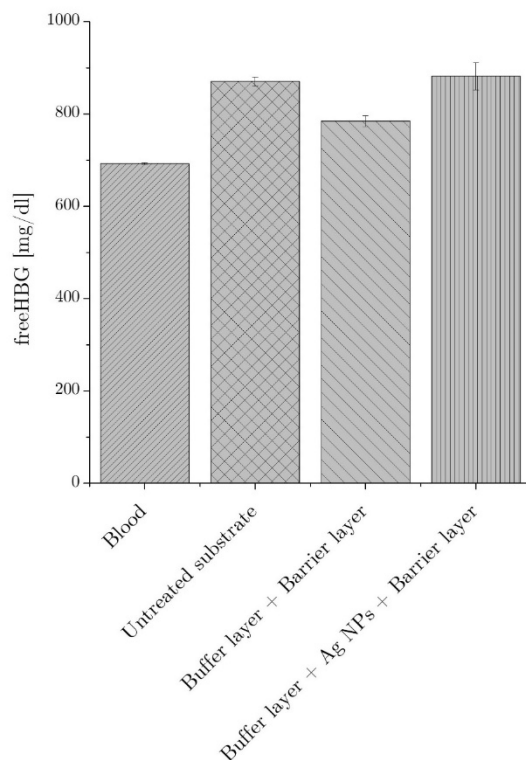


Figure 2.11 Free haemoglobin content after blood-biomaterial dynamic contact test.

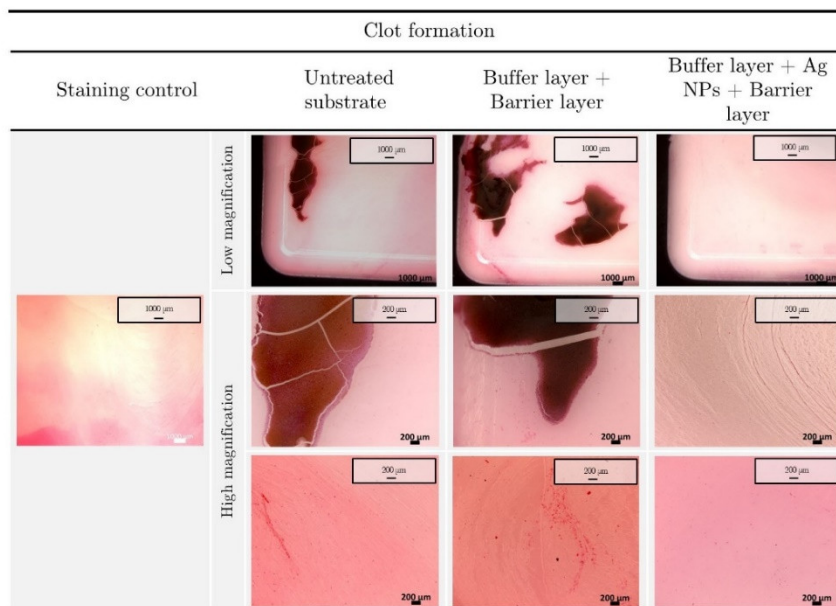
induced cell stress, limiting the haemolysis rate. Even if polar opposite views have also been reported regarding the effect of Ag NPs on blood haemolysis [74–76], recent works [77,78] have clarified that the release of silver ions induced direct platelets and red cells stress. The slight increase of haemolysis rate measured for the nanostructured coating corroborates these findings. We can therefore highlight that the deposited coating displayed an adequate level of hemocompatibility keeping under control the material-induced stress, even when the Ag NPs were embedded in the film matrix.

The analysis of blood-biomaterial contact test was completed staining the substrate surface in order to evaluate the formation of clots. According to low magnification images of the stained samples, reported in Figure 2.12, nanostructured coatings were able to reduce the formation of clots with respect to the pristine and polymeric coated substrates. The analysis of higher magnification fields of view highlighted that when Ag NPs were embedded in the coating matrix, the adhesion of procoagulant fibrine/platelets and the presence of small clots was completely avoided. A comparison with results on haemolysis rate underlined that the higher cell lysis for nanostructured coatings corresponded also to lower clots formation. Although the complex pathways of clot formation on biomaterials surface is a function of surface-blood interaction and it's not the focus of this study, our results were in line to what was presented by Stevens et al. [79]. According to our findings, the authors reported on the increase of haemolysis rate and the contextual reduction of platelets adhesion when nanostructured Ag coated catheters were put in contact with human blood. Even if the mechanism was not fully described, the decrease of platelets adhesion can be accounted as the main reason for a reduction in clot formation on silver coated samples [69].

Following the assess of hemocompatibility, biomaterial biofilm colonization was investigated through a 10 days bacterial broth contact at 37°C. The use of crystal violet staining enabled the identification of bacterial colonies and of the biofilm matrix. Stereo microscope imaging (Figure 2.12b) highlighted the formation of filamentary bacterial colonies on the surface of the untreated substrate. Conversely, the deposition of a polymeric coating strongly reduced the formation of bacterial colonies, hindering the adhesion and formation of biofilm. The introduction of Ag NPs in the deposited film further improved the anti-biofilm performances, reducing the colonies adhesion, particularly in the central region of the sample where nanoparticles were deposited. The significative reduction of bacterial adhesion and biofilm formation on the treated samples can be ascribed again to the combined role of surface properties and Ag toxicity. The deposition of polymeric coatings indeed decreased the surface roughness and led to a modification of the surface free energy/charge, which are among the causes of biofilm proliferation on medical devices [70]. Furthermore, the antibacterial properties of Ag NPs [80] embedded in the nanostructured coating contributed to interfere with bacterial adhesion, improving the performances of the coating.

The results discussed above underline that deposited nanostructured coating were characterized by anti-clot and anti-biofilm performances. While the use of a thin barrier layer prevented Ag NPs dispersion during blood contact test, keeping under control the haemolysis rate, the release of Ag ions through the polymeric matrix hindered bacterial growth and the adhesion and proliferation of biofilm.

a)



b)

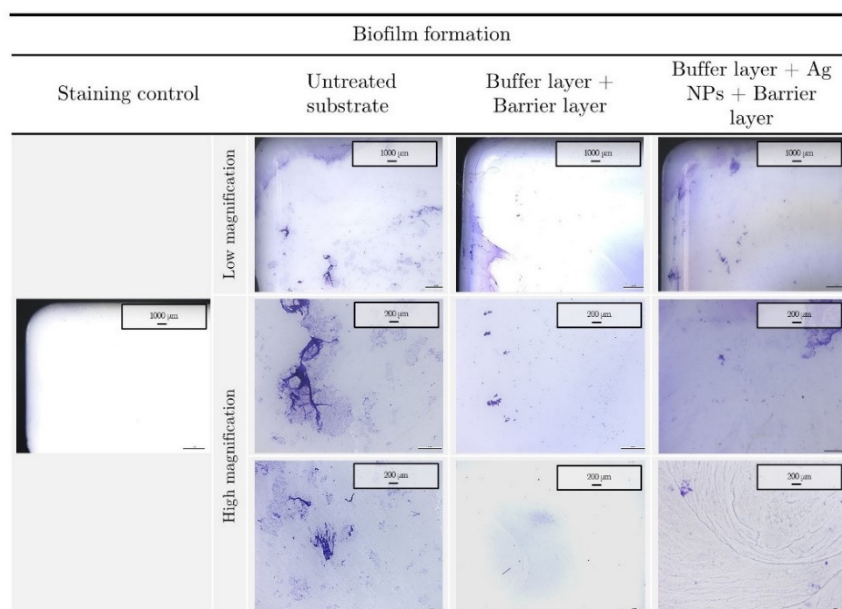


Figure 2.12 Images of untreated and treated biomaterials stained with hematoxylin/eosin and crystal violet after blood (a) and bacterial broth contact tests (b), respectively.

### 2.3.2 Plasma assisted coating deposition on mini catheters

Following the promising results obtained on bidimensional substrates, a new experimental setup was developed with the aim of coating the surface of mini catheters for *in-vivo* testing. The chemical and morphological analysis of treated samples was carried out using both ATR-FTIR and SEM-EDX. Due to the small dimensions of the substrates (OD 0.8 mm) and the softness of the mini catheter, the IR measurements affected coating morphology, probably inducing crack formation and delamination. For this reason, ATR-FTIR techniques was used only to qualitatively assess the presence of the coating after deposition. Conversely, SEM-EDX analysis was employed to perform chemical and morphological analysis all along the mini catheter length. IR spectra outlined the deposition of an organosilicon film, in line with what has been reported above; SEM images (Figure 2.14) highlighted the presence of a coating in all the analyzed fields of view. The nanostructured nature of the film was confirmed by EDX analysis, revealing the presence of Si and Ag in the whole scanned area. With the aim of having qualitative information about the thickness of the deposited coating, a treated mini catheter was sectioned using a cryogenic procedure and analyzed using SEM. Figure 2.13 reports the side views of the treated catheter where the deposited coating is clearly visible. A series of different measurement outlined a coating thickness in the range of 0.5 to 0.8  $\mu\text{m}$ .

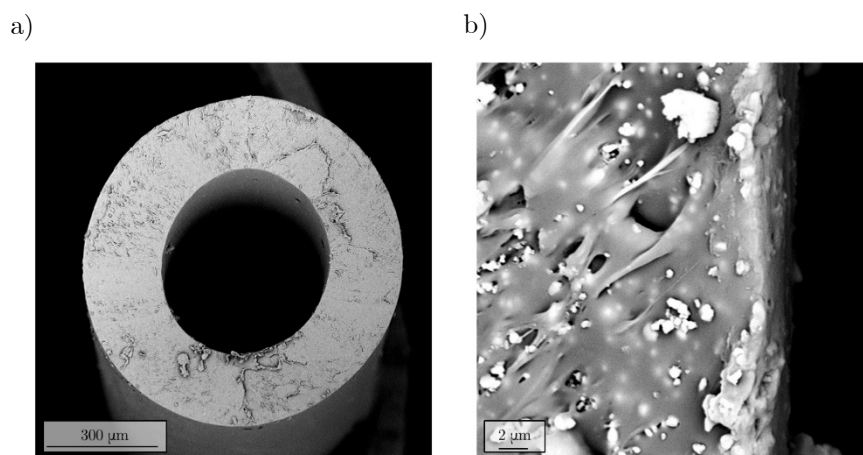


Figure 2.13 SEM images of mini catheter side view after coating deposition.

EtO treatment was carried out with the aim of removing bacterial contamination from the treated substrates before *in-vivo* application. The stability of the coatings after the sterilization processes was assessed using SEM-EDX techniques, performed before and after sample soaking. Achieved results (Figure 2.14) highlighted slight modifications of the surface morphology, probably due to a minimal swelling as reported for 2D substrates and a good retain of Ag and Si content (Appendix, Figure 2.21). Once assessed the coating stability upon sterilization and liquid immersion, the biocompatibility of treated catheters was studied. In this perspective, according to regulations, we carried out an MTT test with the aim of evaluating the release of cytotoxic eluates in the liquid environment. It's important

to remember that ISO guidelines suggest a minimum viability threshold of 70% to identify non-cytotoxic biomaterials. According to our findings reported in Figure 2.15 and normalized

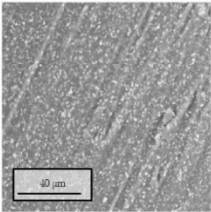
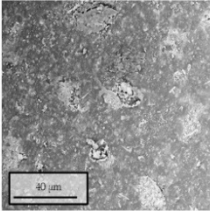
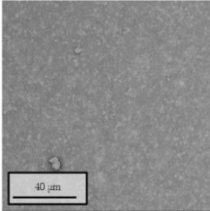
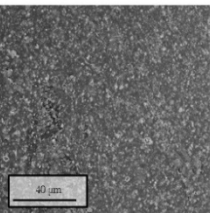
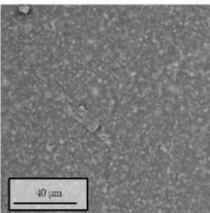
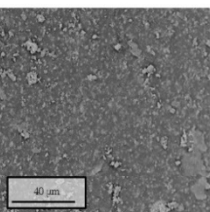
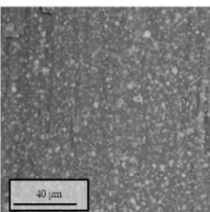
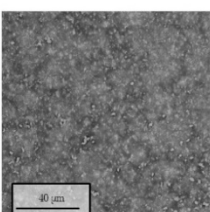
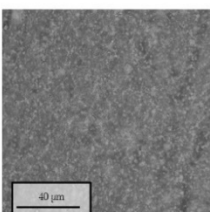
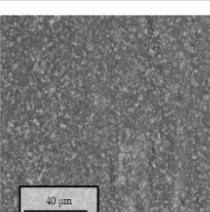
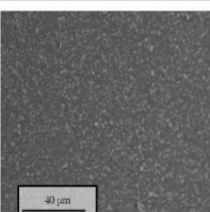
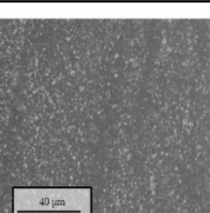
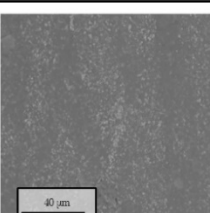
Untreated catheter		EtO sterilized	EtO sterilized after TSB stability test
	0 mm		
	10 mm		
	20 mm		
	30 mm		
	40 mm		
	47.5 mm		

Figure 2.14 SEM images of plasma coated EtO sterilized mini catheter before and after stability test. The length reported in the table is distance from the tip of the catheter.

with respect to untreated cell sample, coated substrates displayed a sufficient level of viability with respect to positive controls (Latex and SDS). The presence of Ag NPs in the nanostructured coatings did not induce significant decrease of cell viability, confirming the good level of hemocompatibility already displayed by the 2D substrates.

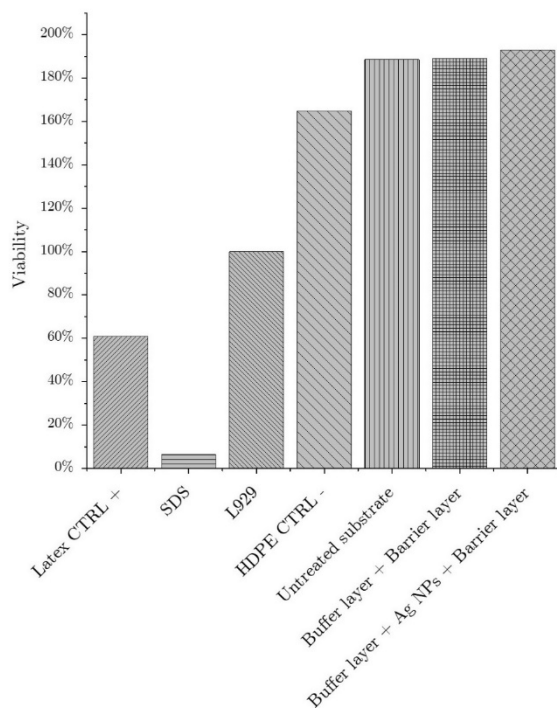


Figure 2.15 Cell viability from indirect MTT assay as suggested by ISO-10993-5: all the tests were normalized to L922 cell viability. HDPE/Latex and SDS were used as internal and positive and negative cellular control respectively.

With the aim of exploring the biological performances of nanostructured coatings, plasma treated mini catheters were used for *in-vivo* assay on mice. Anti-biofilm properties of untreated and nanostructured coated (buffer layer + Ag NPs + barrier layer) samples were investigated exploiting the bioluminescence of an engineered *Pseudomonas aeruginosa* bacterial strain. Once sterilized, mini catheters were contaminated and introduced through subcutaneous surgery under mouse skin. After 2 and 6 days of implant reagents were injected on the mouse backs and the reaction between coelenterazine and bacteria luciferase gene enabled the production of a luminescent signal that was recorded using a BLI camera. Relative luminescent was then used to evaluate the amount of biofilm formed on the mouse back, offering the possibility to online monitor biofilm formation and growth. Raw images and intensity plots are reported in Figure 2.16. Even if not statistically significant, the comparison of bioluminescent light intensity after 2 days showed that Ag NPs coatings were able to reduce biofilm formation with respect to the untreated substrates. Likewise, the

analysis carried out at the sixth day confirmed the significant anti-biofilm performances of nanostructured coatings, able to strongly limit the infection proliferation.

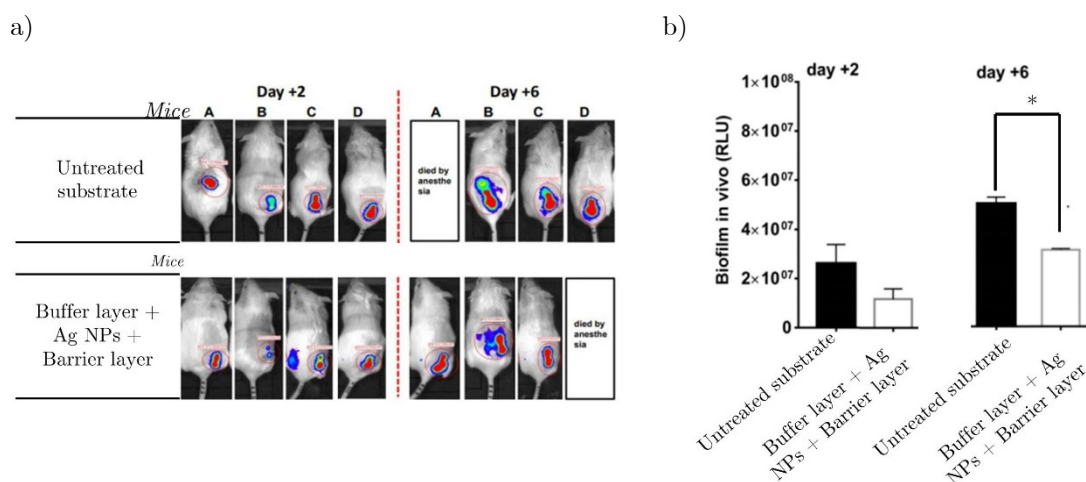


Figure 2.16 Relative luminescence pictures (a) and results (b) of biofilm formation on mini catheters during in-vivo test at the 2nd and 6th day of implant.

Following the *in-vivo* analysis of coating anti-biofilm properties, further experiments were carried out to evaluate the mini catheters biocompatibility for *in-vivo* models. Plasma treated substrates were sterilized using EtO and implanted for 30 days in the jugular vein of rats, following the procedure reported by Feng [48]. Blood count analysis carried out on blood sample after 30 days of implant highlighted no statistical differences in the relative amount of cell components. In particular, results (Figure 2.17) showed that the percentual number of granulocytes, lymphocytes and monocytes remain stable after 30 days of implant.

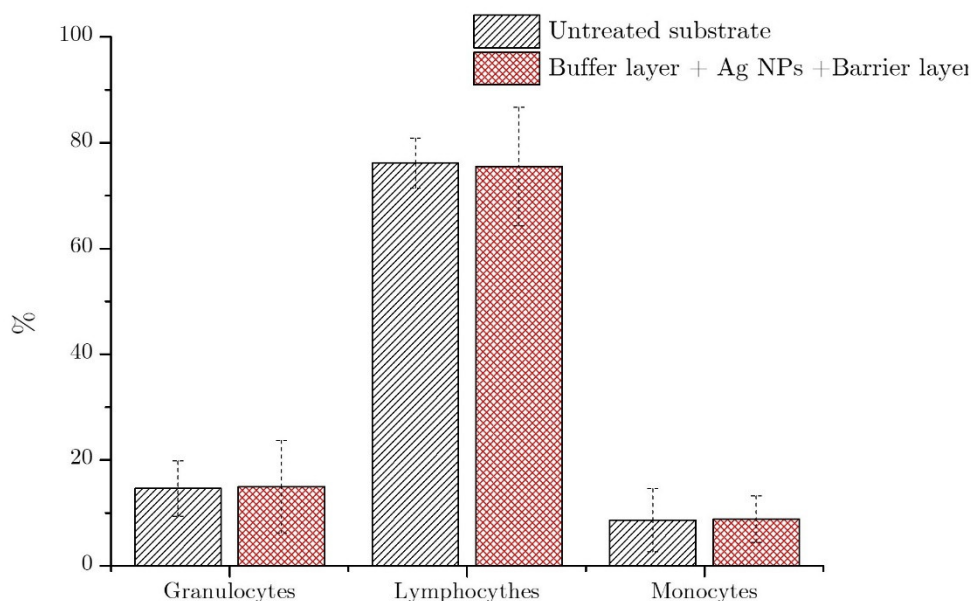


Figure 2.17 Hemochrome analysis of blood samples after 30 days of in-vivo implant of untreated and plasma coated mini catheters.

Moreover, the absence of any significant variation in animal weights was interpreted as signal of animal comfort and state of health (not shown).

While the results reported above can be used to support the macro-biocompatibility of the samples where nanostructured coating were deposited, further histological analyses are currently on-going with the aim to assess the localized effects of silver ions release on jugular cells. As far as the post-explant chemical and morphological characteristics of the biomaterial is concerned, SEM analysis were performed on part of used mini catheters. Even if the assay was carried out only on a small portion of the surface of the catheters (10 mm from 47.5 mm length sample) and without biological replicates, collected data can support preliminary and qualitative hypotheses. The lower and higher magnification pictures (Figure 2.18) pointed out the presence of cells and aggregates on the surface of untreated samples. Conversely, plasma coated mini catheters exhibited a cleaner surface, where only the cracks belonging to the coating were detected. Besides the interesting performances in terms of prevention of cells adhesion, the presence of the deposited coating after 30 days of *in-vivo* implant is a notable result, confirming coating integrity under working conditions.

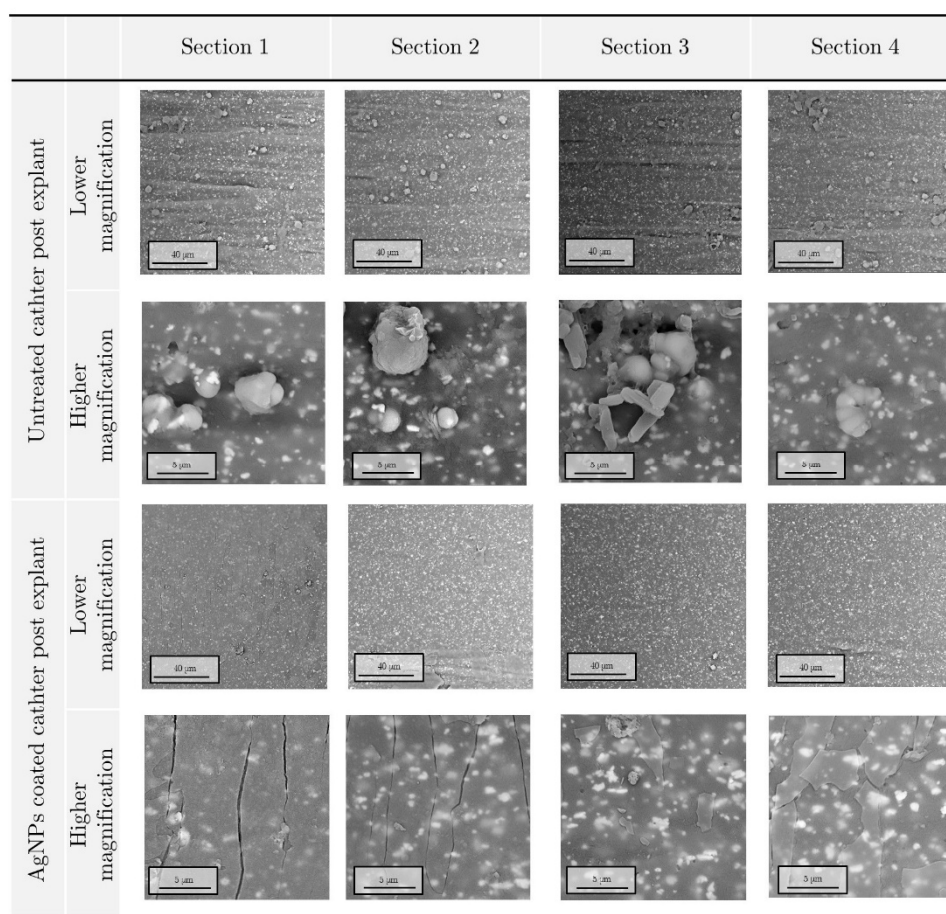


Figure 2.18 SEM images of untreated and plasma treated catheter post-explant after *in-vivo* test.

## 2.4 Conclusions

The present study illustrates the potentialities of nanostructured silver coatings deposited through atmospheric pressure plasma technology. With the aim of reducing biofilm adhesion and control the clot formation on polyurethane substrates already employed for CVC production, Ag NPs were synthesized in the plasma discharge and deposited in between two polymeric layers. While organic characteristics of deposited films were confirmed by means of FTIR spectroscopy and CA analysis, electron microscopy outlined coating stability upon liquid immersion. The presence of Ag NPs provided antibacterial properties to the coating, reducing biofilm formation and adhesion on biomaterial surface. Clot formation and haemolysis was also kept under control with respect to the untreated substrates, probing material biocompatibility. The developed approach, suitable for in-situ and localized surface functionalization, offered the possibility to continue the study investigating the deposition of multilayer coating on mini catheters. Besides chemical and morphological characterization and EtO stability of treated samples, mini catheters biocompatibility was assessed. The absence of any cytotoxic effect granted the possibility to carry on in-vivo tests on animal model. While confirming the coating hemo and biocompatibility, preliminary results suggested a positive effect of nanostructured coating deposition in terms of biofilm proliferation. Presented achievements suggests the importance of a comprehensive approach for the investigation of plasma treated biomaterial performances. Indeed, in the perspective of in-vivo testing and future applications, material biocompatibility and coating stability are mandatory requirements that need to be investigated. Although plasma technology offers unique features in terms of material processing and properties tunability, forthcoming applications will gain advantages of a better understanding of the role of coating surface free energy and morphology both on antibacterial properties and on cell compatibility.

## 2.5 References

- [1] Curtis L T 2008 Prevention of hospital-acquired infections: review of non-pharmacological interventions *J. Hosp. Infect.* **69** 204–19
- [2] Reed D and Kemmerly S A 2009 Infection Control and prevention: A review of hospital-acquired infections and the economic implications *Ochsner J.* **9** 27–31
- [3] World Health Organization 2011 The Burden of Health Care-Associated Infection Worldwide: A Summary *World Heal. Organ.* **3**
- [4] Cloutier M, Mantovani D and Rosei F 2015 Antibacterial Coatings: Challenges, Perspectives, and Opportunities *Trends Biotechnol.* **33** 637–52
- [5] Cvelbar U, Walsh J L, Černák M, de Vries H W, Reuter S, Belmonte T, Corbella C, Miron C, Hojnik N, Jurov A, Puliyalil H, Gorjanc M, Portal S, Laurita R, Colombo V, Schäfer J, Nikiforov A, Modic M, Kylian O, Polak M, Labay C, Canal J M, Canal C, Gherardi M, Bazaka K, Sonar P, Ostrikov K K, Cameron D, Thomas S and Weltmann K D 2019 White paper on the future of plasma science and technology in plastics and textiles *Plasma Process. Polym.* **16** 1–37
- [6] Bekeschus S, Favia P, Robert E and von Woedtke T 2019 White paper on plasma for medicine and hygiene: Future in plasma health sciences *Plasma Process. Polym.* **16** 1–12
- [7] Donlan R M 2001 Biofilms and device-associated infections *Emerg. Infect. Dis.* **7** 277–81
- [8] Neubeiser A, Bonsignore M, Tafelski S, Alefelder C, Schwegmann K, Rüdén H, Geffers C and Nachtigall I 2019 Mortality attributable to hospital acquired infections with multidrug-resistant bacteria in a large group of German hospitals *J. Infect. Public Health*
- [9] Bouaidat S, Berendsen C, Thomsen P, Petersen S G, Wolff a and Jonsmann J 2004 Micro patterning of cell and protein non-adhesive plasma polymerized coatings for biochip applications. *Lab Chip* **4** 632–7
- [10] Tiwari G, Tiwari R, Sriwastawa B, Bhati L, Pandey S, Pandey P and Bannerjee S K 2012 Drug delivery systems: An updated review *Int. J. Pharm. Investig.* **2** 2
- [11] Biederman H 2004 *Plasma polymer films* (World Scientific)
- [12] D’Agostino R 1990 *Plasma Deposition, Treatment, and Etching of Polymers* ed R D’Agostino (Academic Press)
- [13] d’Agostino R, Favia P and Fracassi F 1997 *Plasma processing of polymers* vol 346 (Springer Science & Business Media)
- [14] Yasuda H K 2012 *Plasma Polymerization*
- [15] Agarwala M, Barman T, Gogoi D, Choudhury B, Pal A R and Yadav R N S 2014 Highly effective antibiofilm coating of silver-polymer nanocomposite on polymeric medical devices deposited by one step plasma process *J. Biomed. Mater. Res. - Part*

- [16] Vasilev K, Griesser S S and Griesser H J 2011 Antibacterial surfaces and coatings produced by plasma techniques *Plasma Process. Polym.* **8** 1010–23
- [17] Hegemann D, Blanchard N E and Heuberger M 2016 Reduced Protein Adsorption on Plasma Polymer Films Comprising Hydrophobic/Hydrophilic Vertical Chemical Gradients *Plasma Process. Polym.* **13** 494–8
- [18] Palumbo F, Treglia A, Lo Porto C, Fracassi F, Baruzzi F, Frache G, El Assad D, Pistillo B R and Favia P 2018 Plasma-Deposited Nanocapsules Containing Coatings for Drug Delivery Applications *ACS Appl. Mater. Interfaces* **10** 35516–25
- [19] Kratochvíl J, Kuzminova A and Kylián O 2018 State-of-the-art, and perspectives of, silver/plasma polymer antibacterial nanocomposites *Antibiotics* **7**
- [20] Liguori A, Traldi E, Toccaceli E, Laurita R, Pollicino A, Focarete M L, Colombo V and Gherardi M 2015 Co-Deposition of Plasma-Polymerized Polyacrylic Acid and Silver Nanoparticles for the Production of Nanocomposite Coatings Using a Non-Equilibrium Atmospheric Pressure Plasma Jet *Plasma Process. Polym.* **13** 623–32
- [21] Beier O, Pfuch A, Horn K, Weisser J, Schnabelrauch M and Schimanski A 2013 Low temperature deposition of antibacterially active silicon oxide layers containing silver nanoparticles, prepared by atmospheric pressure plasma chemical vapor deposition *Plasma Process. Polym.* **10** 77–87
- [22] Beier O, Pfuch A, Horn K, Spange S, Ramm M, Jäger E, Grünler B and Schimanski A 2013 Novel possibilities to create functional thin films by using cold atmospheric pressure plasma enhanced CVD techniques *NANOCON 2013 - Conf. Proceedings, 5th Int. Conf.* 128–34
- [23] Deng X, Leys C, Vujosevic D, Vuksanovic V, Cvelbar U, De Geyter N, Morent R and Nikiforov A 2014 Engineering of Composite Organosilicon Thin Films with Embedded Silver Nanoparticles via Atmospheric Pressure Plasma Process for Antibacterial Activity *Plasma Process. Polym.* 921–30
- [24] Deng X, Yu Nikiforov A, Coenye T, Cools P, Aziz G, Morent R, De Geyter N and Leys C 2015 Antimicrobial nano-silver non-woven polyethylene terephthalate fabric via an atmospheric pressure plasma deposition process *Sci. Rep.* **5** 1–10
- [25] Yu Nikiforov A, Deng X, Onyshchenko I, Vujosevic D, Vuksanovic V, Cvelbar U, De Geyter N, Morent R and Leys C 2016 Atmospheric pressure plasma deposition of antimicrobial coatings on non-woven textiles *Eur. Phys. J. Appl. Phys* **75** 1–6
- [26] AlmaPlasma srl AlmaPLUS
- [27] Soulié S 2019 *Étude de l'asclépiade pour des applications de régénération osseuses* (University of Laval)
- [28] Soulié S, Bilem I, Chevallier P, Elkoun S, Naudé N, Laroche G, Soulié S, Bilem I, Chevallier P and Elkoun S 2019 Milkweed scaffold: a new candidate for bone cell growth *Int. J. Polym. Mater. Polym. Biomater.* **0** 1–12

- [29] Valinataj Omran A, Baitukha A, Pulpytel J, Sohbatzadeh F and Arefi-Khonsari F 2018 Atmospheric pressure surface modification and cross-linking of UHMWPE film and inside HDPE tube by transporting discharge *Plasma Process. Polym.* **15** 1–12
- [30] Maguire P, Rutherford D, Macias-Montero M, Mahony C, Kelsey C, Tweedie M, Pérez-Martin F, McQuaid H, Diver D and Mariotti D 2017 Continuous In-Flight Synthesis for On-Demand Delivery of Ligand-Free Colloidal Gold Nanoparticles *Nano Lett.* **17** 1336–43
- [31] Nikiforov A, Deng X, Xiong Q, Cvelbar U, DeGeyter N, Morent R and Leys C 2016 Non-thermal plasma technology for the development of antimicrobial surfaces: a review *J. Phys. D. Appl. Phys.* **49** 204002
- [32] Patil H V, Patil V C, Ramteerthkar M N and Kulkarni R D 2011 Central venous catheter-related bloodstream infections in the intensive care unit *Indian J. Crit. Care Med.* **15** 213
- [33] Gahlot R, Nigam C, Kumar V, Yadav G and Anupurba S 2014 Catheter-related bloodstream infections *Int. J. Crit. Illn. Inj. Sci.* **4** 161
- [34] Esposito S, Purrello S M, Bonnet E, Novelli A, Tripodi F, Pascale R, Unal S and Milkovich G 2013 Central venous catheter-related biofilm infections: An up-to-date focus on methicillin-resistant *Staphylococcus aureus* *J. Glob. Antimicrob. Resist.* **1** 71–8
- [35] Jaffer I H, Fredenburgh J C, Hirsh J and Weitz J I 2015 Medical device-induced thrombosis: What causes it and how can we prevent it? *J. Thromb. Haemost.* **13** S72–81
- [36] Allen A W, Megargell J L, Brown D B, Lynch F C, Singh H, Singh Y and Waybill P N 2000 Venous thrombosis associated with the placement of peripherally inserted central catheters *J. Vasc. Interv. Radiol.* **11** 1309–14
- [37] Barletta F, Liguori A, Leys C, Colombo V, Gherardi M and Nikiforov A 2018 Novel method for NH-rich coatings engineering by means of aerosol assisted atmospheric pressure plasma deposition *Mater. Lett.* **214** 76–9
- [38] Stancampiano A, Simoncelli E, Boselli M and Colombo V 2018 Experimental investigation on the interaction of a nanopulsed plasma jet with a liquid target
- [39] Boselli M, Colombo V, Ghedini E, Gherardi M, Laurita R, Liguori A, Sanibondi P and Stancampiano A 2014 Schlieren high-speed imaging of a nanosecond pulsed atmospheric pressure non-equilibrium plasma jet *Plasma Chem. Plasma Process.* **34** 853–69
- [40] Barletta F and Nikiforov A 2019 Insights into plasma - assisted polymerization at atmospheric pressure by spectroscopic diagnostics *Plasma Process. Polym.* 1–15
- [41] Liguori A, Pollicino A, Stancampiano A, Tarterini F, Focarete M L, Colombo V and Gherardi M 2016 Deposition of Plasma-Polymerized Polyacrylic Acid Coatings by a Non-Equilibrium Atmospheric Pressure Nanopulsed Plasma Jet *Plasma Process. Polym.* **13** 375–86

- [42] International Organization for Standardization 2010 Biological evaluation of medical devices - Part 4: Selection of tests for interactions with blood EN ISO 10993-13:2010
- [43] International Organization for Standardization 2017 Implants for surgery — Homopolymers, copolymers and blends on poly(lactide) — In vitro degradation testing BS ISO 13781:2017
- [44] International Organization for Standardization 2017 Biological evaluation of medical devices - Part 4: Selection of tests for interactions with blood EN ISO 10993-4:2017
- [45] Petrachi T, Resca E, Piccinno M S, Biagi F, Strusi V, Dominici M and Veronesi E 2017 An Alternative Approach to Investigate Biofilm in Medical Devices: A Feasibility Study *Int. J. Environ. Res. Public Health* **14** 1587
- [46] Wallin B R F 2018 A Practical Guide to ISO 10993-5: Cytotoxicity Testing for cytotoxicity is a good first step toward ensuring the biocompatibility of a medical device . 1–6
- [47] Kucharíková S, Vande Velde G, Himmelreich U and Van Dijck P 2015 *Candida albicans* Biofilm Development on Medically-relevant Foreign Bodies in a Mouse Subcutaneous Model Followed by Bioluminescence Imaging *J. Vis. Exp.* 1–9
- [48] Feng J, Fitz Y, Li Y, Fernandez M, Cortes Puch I, Wang D, Pazniokas S, Bucher B, Cui X and Solomon S B 2015 Catheterization of the Carotid Artery and Jugular Vein to Perform Hemodynamic Measures, Infusions and Blood Sampling in a Conscious Rat Model *J. Vis. Exp.* 2–7
- [49] Massines F, Gherardi N, Naudé N and Ségur P 2009 Recent advances in the understanding of homogeneous dielectric barrier discharges *EPJ Appl. Phys.* **47**
- [50] Sarani A, Nikiforov A Y and Leys C 2010 Atmospheric pressure plasma jet in Ar and Ar/H<sub>2</sub>O mixtures: Optical emission spectroscopy and temperature measurements *Phys. Plasmas* **17** 063504
- [51] Urabe K, Yamada K and Sakai O 2011 Discharge-mode transition in jet-type dielectric barrier discharge using argon/acetone gas flow ignited by small helium plasma jet *Jpn. J. Appl. Phys.* **50** 116002
- [52] Tardiveau P and Marode E 2003 Point-to-plane discharge dynamics in the presence of dielectric droplets *J. Phys. D. Appl. Phys.* **36** 1204–11
- [53] Morent R, De Geyter N, Van Vlierberghe S, Dubruel P, Leys C and Schacht E 2009 Organic-inorganic behaviour of HMDSO films plasma-polymerized at atmospheric pressure *Surf. Coatings Technol.* **203** 1366–72
- [54] Socrates G 2004 *Infrared and Raman characteristic group frequencies: tables and charts* (John Wiley & Sons)
- [55] Tolstoy V P, Chernyshova I and Skryshevsky V A 2003 *Handbook of infrared spectroscopy of ultrathin films* (John Wiley & Sons)
- [56] Morent R, De Geyter N, Van Vlierberghe S, Dubruel P, Leys C, Gengembre L, Schacht E and Payen E 2009 Deposition of HMDSO-based coatings on PET substrates

- using an atmospheric pressure dielectric barrier discharge *Prog. Org. Coatings* **64** 304–10
- [57] Deng X, Nikiforov A Y, De Geyter N, Morent R and Leys C 2013 Deposition of a TMDSO-based film by a non-equilibrium atmospheric pressure DC plasma jet *Plasma Process. Polym.* **10** 641–8
- [58] Yüce M Y and Demirel A L 2008 The effect of nanoparticles on the surface hydrophobicity of polystyrene *Eur. Phys. J. B* **64** 493–7
- [59] Wenzel R N 1936 Resistance of solid surfaces to wetting by water *Ind. Eng. Chem.* **28** 988–94
- [60] Hong J, Yick S, Chow E, Murdock A, Fang J, Seo D H, Wolff A, Han Z, Van Der Laan T, Bendavid A, Ostrikov K and Murphy A B 2019 Direct plasma printing of nano-gold from an inorganic precursor *J. Mater. Chem. C* **7** 6369–74
- [61] Srivastava N and Wang C 2011 Effects of water addition on OH radical generation and plasma properties in an atmospheric argon microwave plasma jet *Journal of Applied Physics* vol 110 pp 1–9
- [62] Petersen J, Bardou J, Dinić A, Ruch D and Gherardi N 2012 Organosilicon coatings deposited in atmospheric pressure townsend discharge for gas barrier purpose: Effect of substrate temperature on structure and properties *ACS Appl. Mater. Interfaces* **4** 5872–82
- [63] Elam F M, Starostin S A, Meshkova A S, Van Der Velden-Schuermans B C A M, Van De Sanden M C M and De Vries H W 2017 Defect prevention in silica thin films synthesized using AP-PECVD for flexible electronic encapsulation *J. Phys. D: Appl. Phys.* **50**
- [64] Grüniger A and Von Rohr P R 2004 Influence of defects in SiO<sub>x</sub> thin films on their barrier properties *Thin Solid Films* **459** 308–12
- [65] Bashir M and Bashir S 2015 Hydrophobic–Hydrophilic Character of Hexamethyldisiloxane Films Polymerized by Atmospheric Pressure Plasma Jet *Plasma Chem. Plasma Process.* **35** 739–55
- [66] Dušek K, Dušková-Smrčková M and Douglas C B 2017 Swelling of Coating Films *Protective Coatings* (Springer) pp 271–91
- [67] Kylián O, Kratochvíl J, Petr M, Kuzminova A, Slavínská D, Biederman H and Beranová J 2017 Ag/C:F Antibacterial and hydrophobic nanocomposite coatings *Funct. Mater. Lett.* **10** 3–6
- [68] Alissawi N, Peter T, Strunskus T, Ebbert C, Grundmeier G and Faupel F 2013 Plasma-polymerized HMDSO coatings to adjust the silver ion release properties of Ag/polymer nanocomposites *J. Nanoparticle Res.* **15**
- [69] Gorbet M B and Sefton M V. 2006 Biomaterial-associated thrombosis: Roles of coagulation factors, complement, platelets and leukocytes *Biomater. Silver Jubil. Compend.* **25** 219–41

- [70] Katsikogianni M and Missirlis Y F 2004 Concise review of mechanisms of bacterial adhesion to biomaterials and of techniques used in estimating bacteria-material interactions *Eur. Cells Mater.* **8** 37–57
- [71] Offeman R D and Williams M C 1979 Material Effects in Shear-Induced Hemolysis **7** 359–91
- [72] Umezu M, Yamada T, Fujimasu H, Fujimoto T, Ranawake M, Nogawa A and Kijima T 1996 Effects of Surface Roughness on Mechanical Hemolysis *Artif. Organs* **20** 575–8
- [73] Maruyama O, Nishida M, Yamane T, Oshima I, Adachi Y and Masuzawa T 2006 Hemolysis resulting from surface roughness under shear flow conditions using a rotational shear stressor *Artif. Organs* **30** 365–70
- [74] Bandyopadhyay D, Baruah H, Gupta B and Sharma S 2012 Silver nano particles prevent platelet adhesion on immobilized fibrinogen *Indian J. Clin. Biochem.* **27** 164–70
- [75] Shrivastava S, Bera T, Singh S K, Singh G, Ramachandrarao P and Dash D 2009 Characterization of antiplatelet properties of silver nanoparticles *ACS Nano* **3** 1357–64
- [76] Huang H, Lai W, Cui M, Liang L, Lin Y, Fang Q, Liu Y and Xie L 2016 An Evaluation of Blood Compatibility of Silver Nanoparticles *Sci. Rep.* **6** 1–15
- [77] Bian Y, Kim K, Ngo T, Kim I, Bae O N, Lim K M and Chung J H 2019 Silver nanoparticles promote procoagulant activity of red blood cells: A potential risk of thrombosis in susceptible population *Part. Fibre Toxicol.* **16** 1–14
- [78] Laloy J, Minet V, Alpan L, Mullier F, Beken S, Toussaint O, Lucas S and Dogné J M 2014 Impact of Silver Nanoparticles on Haemolysis, Platelet Function and Coagulation *Nanobiomedicine* **1** 1–9
- [79] Stevens K N J, Crespo-Biel O, van den Bosch E E M, Dias A A, Knetsch M L W, Aldenhoff Y B J, van der Veen F H, Maessen J G, Stobberingh E E and Koole L H 2009 The relationship between the antimicrobial effect of catheter coatings containing silver nanoparticles and the coagulation of contacting blood *Biomaterials* **30** 3682–90
- [80] Monteiro D R, Gorup L F, Takamiya A S, Ruvollo-Filho A C, Camargo E R de and Barbosa D B 2009 The growing importance of materials that prevent microbial adhesion: antimicrobial effect of medical devices containing silver *Int. J. Antimicrob. Agents* **34** 103–10

## 2.6 Appendix

### 2.6.1 Plasma assisted deposition on 2D substrates

#### 2.6.1.1 EDX spectra

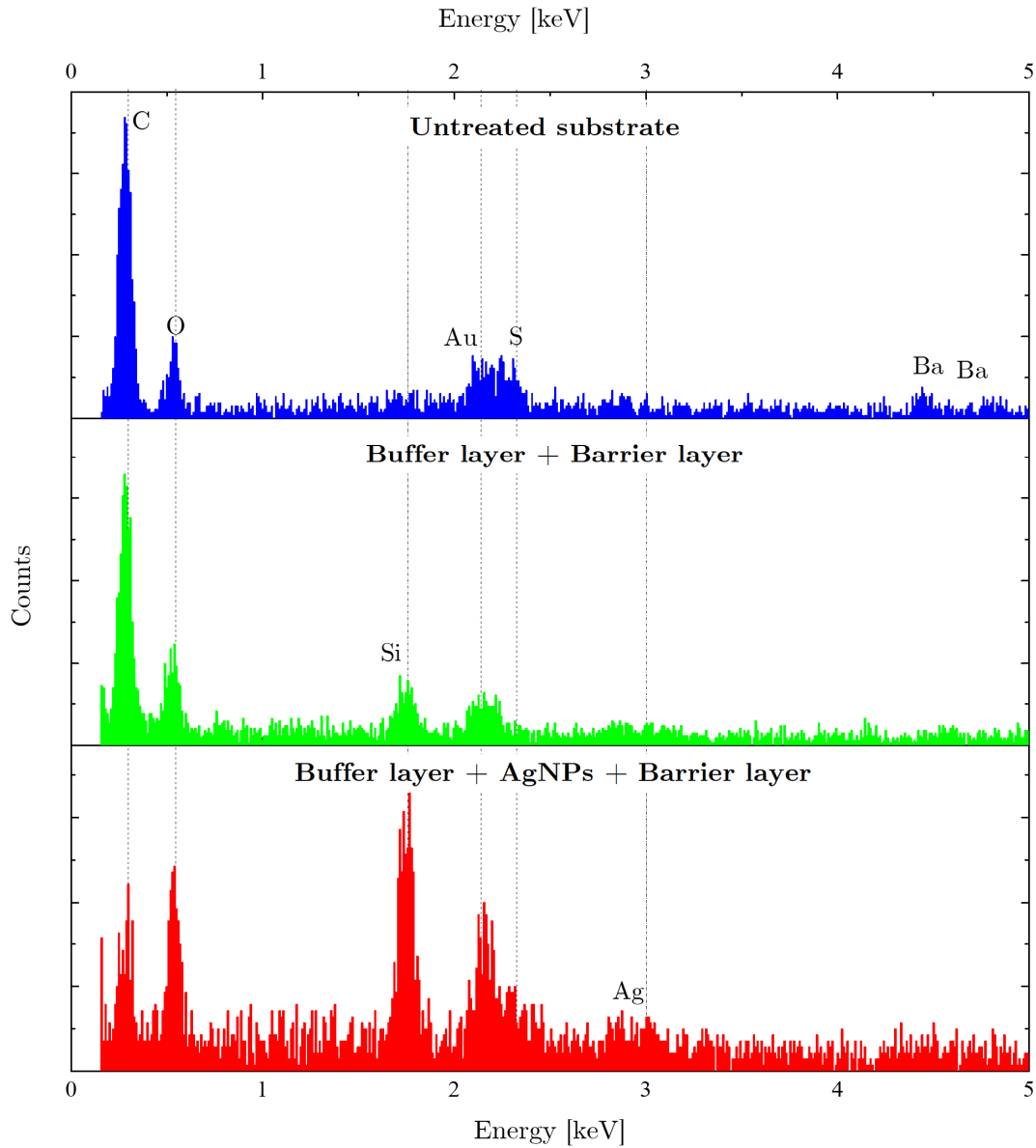


Figure 2.19 EDX spectra of untreated, buffer layer + barrier layer, buffer layer + Ag NPs + barrier layer coatings.

Figure 2.19 reports the EDX spectra of deposited polymeric (buffer layer + barrier layer) and nanostructured coating (buffer layer + Ag NPs + barrier layer) with respect to the untreated sample. While confirming the presence of  $\text{BaSO}_4$  particles, the characteristic peak

of Si was found in both polymeric and nanostructured coating. The latter one also outlined the presence of Ag peak due to NPs embedded in the multilayer structure.

### 2.6.1.2 In-vitro tests, coloration control

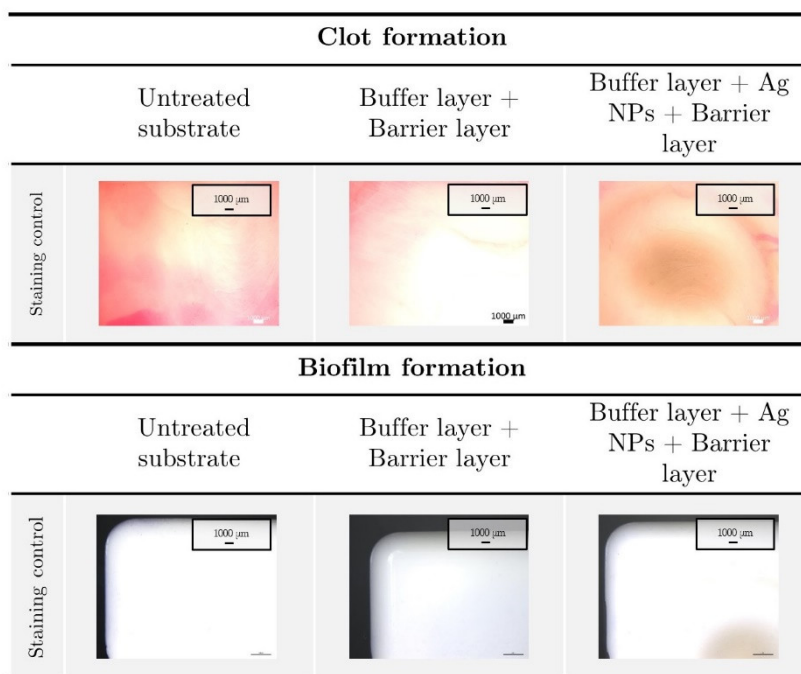


Figure 2.20 Coloration control for hematoxylin/eosin and crystal violet staining.

Figure 2.20 reports the coloration control for dynamic blood and bacterial broth contact tests. Samples were stained according the procedure described in the Materials and Methods paragraph and afterwards stereo microscopy was used to analyzed the surface of biomaterials.

## 2.6.2 Plasma assisted deposition on mini catheters

### 2.6.2.1 EDX spectra

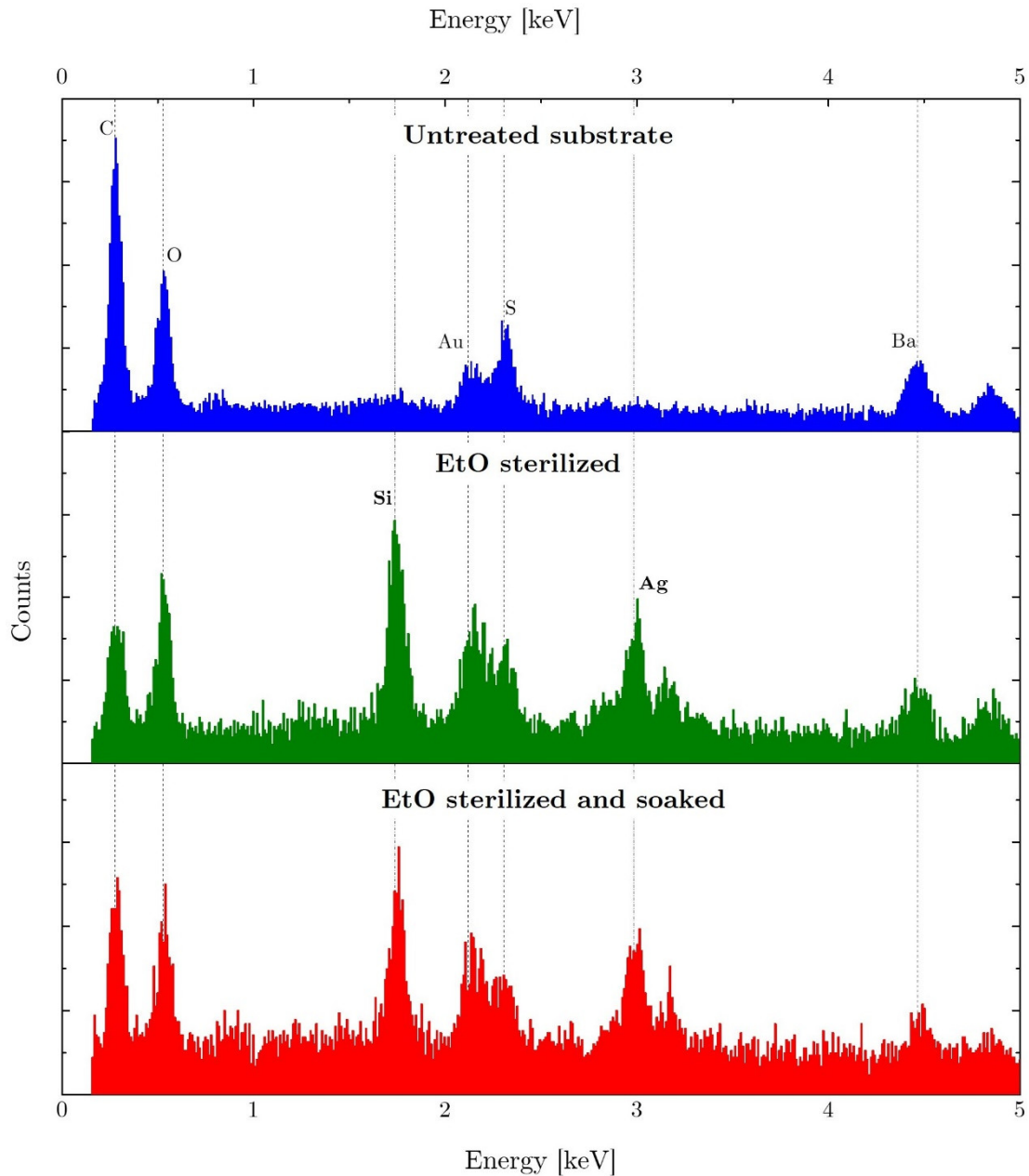


Figure 2.21 EDX spectra of untreated, plasma treated EtO sterilized mini catheter before and after stability test (all spectra were collected from a region located at 30 mm from the tip of the catheter).

EDX spectra collected from mini catheters after EtO sterilization are reported in Figure 2.21. Untreated biomaterial outlined the presence of C and O characteristics peaks, confirming the polymeric nature of the substrate. While the presence of Au can be ascribed to the coating procedure (see Materials and Methods paragraph), Ba and S peaks confirmed that during the moulding process the mini catheters were loaded with  $\text{BaSO}_4$ , with the aim of conferring radiopaque properties. When the nanostructured coating was deposited on biomaterials,

EDX spectrum outlined the presence of Si and Ag. Finally, the retain of Si and Ag after stability test corroborated materials suitability for in-vivo testing.

**CHAPTER 3**  
**In-flight Synthesis and Online  
Characterization of Silver Nanoparticles  
from Aerosol Droplets Reacting in a Non-  
thermal Plasma**

### 3.1 Introduction

The unique features and chemo-physical characteristics of non-equilibrium discharges in contact with liquid interface have brought to the development of innovative applications of atmospheric pressure plasma (APP) with large impact in different fields [1,2]. The unique non-equilibrium and multiphase environment at plasma-liquid interface is characterized by the presence of different reactive species, such as electrons, radicals, ions, that can promote a large number of chemical reaction mechanisms, both in the gas and the liquid phase (Figure 3.1). In this framework, the interaction of gas discharges with liquid solutions have attracted particular interest in the field of material processing, supporting nanostructure synthesis and

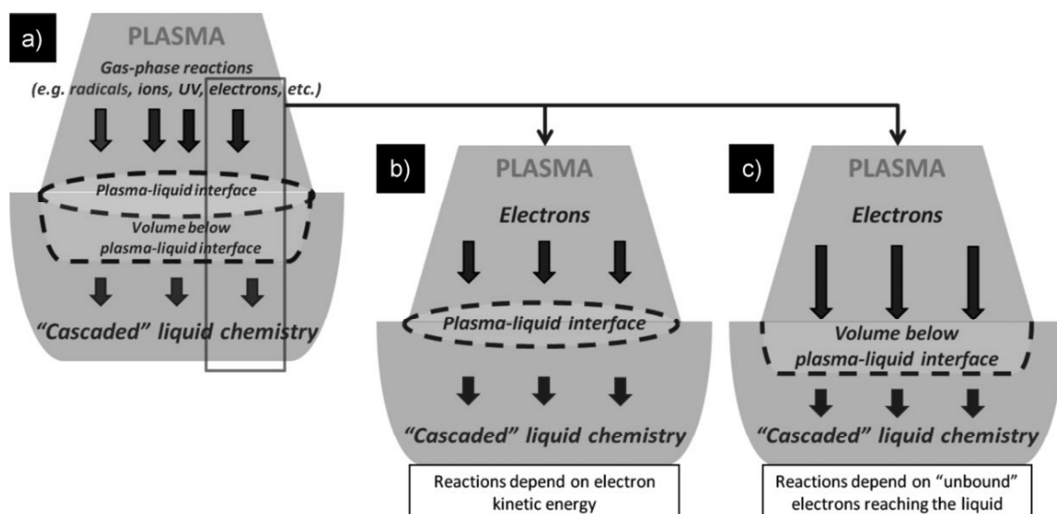


Figure 3.1 Description of plasma induced liquid chemistry. With permission from [2].

surface functionalization for various applications [2–6]. Nanomaterials are usually produced in the liquid phase through the plasma assisted reduction of dissolved salt ions or solid metal dissolution. Major works in this field were spurred by the promising results achieved by Sankaran [7] and Mariotti [8]. Starting from an electrochemical reactor, Richmonds and Sankaran [7] replaced one of the two electrodes with a plasma discharge enabling the synthesis of silver (Ag) and gold (Au) nanoparticles in the liquid phase (Figure 3.2). The plasma is usually generated by means of a capillary characterized by internal diameter in the range of 0.1-1 mm placed few mm above the treated solution leading to a contact-less electrode configuration. This configuration is usually referred as microplasma discharge.

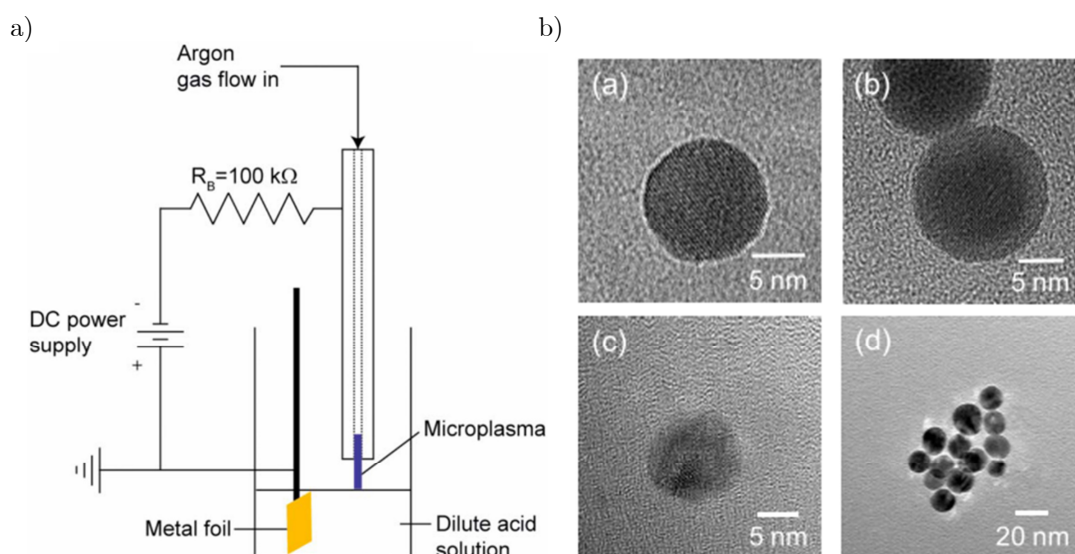


Figure 3.2 a) Schematic of the setup used by Richmonds et al. for the synthesis of Ag and Au nanoparticles. b) TEM images of synthesized particles. With permission from [7].

Plasma generated reactive species, both in the gas and liquid phase, were responsible for the reduction of metal ions in the liquid phase, leading to spherical particle nucleation and growth (Figure 3.2b). Due to the versatility of the setup, great achievements have been obtained so far in terms of synthesized materials and particle functionalities [6,9–12]. Likewise, deeper investigations on the reduction driving mechanisms have been carried out. While the formation of reactive oxygen and nitrogen species was already widely reported for liquid in contact with gas discharges [13,14], only recently evidence of electron solvation has been achieved [15–18]. The key role of aqueous electrons in the reduction of silver ions was highlighted by Vos et al. [19] and more recently discussed by Ghosh et al. [20]. Conversely, the main mechanism leading to gold nanostructure synthesis was found to be strongly related to hydrogen peroxide produced through plasma-liquid interaction [21]. The gain of deeper knowledge of the reaction pathways, recently enabled the use of microplasma setups for the production and tailoring of silver containing composite particles to be employed in the biomedical field with the aim of preventing bacterial growth [22]. Even if plasma and liquid interaction are still under investigation and fundamental studies are currently ongoing [23], part of the research community is moving the first steps towards the practical process

application [24], facing the limitations of the current setups. Indeed, because of long treatment time ( $\sim$  tens of minutes) and limited solution mixing, capping agents are often required to prevent particle aggregation and ensure their stabilization in solution. Moreover, the most common plasma-liquid configurations employed for material synthesis are characterized by severely localized reaction regions which may lead to mass transport limitation and inhomogeneities. Considering these issues, the latest efforts of the scientific community have been devoted to overcome the low conversion efficiency and avoid possible nanomaterial contamination due to undesired reaction in the gas and liquid phases often present in batch processes. In this perspective, the direct contact of a plasma discharge with a continuous flowing liquid has been reported by Ghosh [25] and Bouchard [26] for the plasma assisted synthesis of Ag and Au particles, respectively. In Ghosh's work, reaction rate was enhanced with respect to a traditional microplasma batch process exploiting the presence of a liquid jet in contact with the plasma discharge. Together with the work done by Bouchard, the proposed setups offered the possibility to produce continuous nanoparticles flow, opening opportunities for future scale up. Nevertheless, the colloidal nature of synthesized nanoparticles and the complexity of the setup have so far limited further experimental efforts and improvement in this direction. Only recently, following the approach used for APP assisted gas-phase nucleation [27–29], flow-through plasma reactor coupled with liquid aerosol injection has been proposed by Maguire et al. [30] as an alternative strategy to overcome the limitations associated with batch processes, enabling the on-demand and in-situ synthesis of Au NPs. The authors developed a complex setup (Figure 3.3<sup>1</sup>) where aerosol injector was coupled with a RF plasma reactor here reported in [31], enabling the synthesis of small (4 nm) and high quality Au particles. The approach introduces liquid droplets in the plasma discharge where each individual droplet acts as a micro-reactor characterized by enhanced surface to volume ratio and with diameter in the range of 1-50  $\mu\text{m}$ . The proposed setup offers the possibility to exploit liquid phase nucleation reactions, producing nanomaterials that otherwise could hardly be processed at ambient condition because the

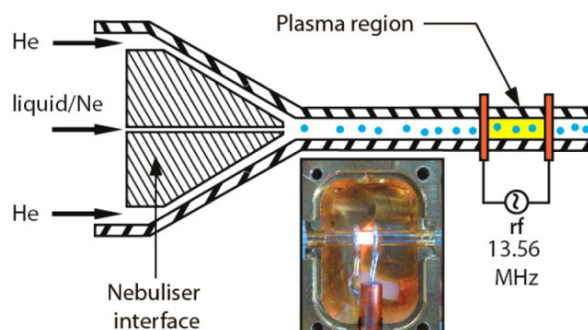


Figure 3.3 Schematic of the plasma reactor developed by Mariotti et al. to support nanomaterial processing. With permission from [30]<sup>1</sup>.

<sup>1</sup> <https://pubs.acs.org/doi/10.1021/acs.nanolett.6b03440>. Further permissions related to the material excerpted should be directed to the ACS.

lack of gas precursors at ambient condition due to their high boiling temperature. In the plasma discharge, microdroplets experience a unique environment, rich with charge carriers and energetic neutral gas species that can react with liquids through different pathways modifying its physico-chemical characteristics [32–34]. Although various research groups have already reported on the use of plasma-aerosol reactors, both for material processing [35–37] and bacterial decontamination [38–40], a deeper knowledge on multiphase phenomena is desired and would be a great achievement for future applications in nanomaterial processing [41]. In light of this perspective, the aim of this work is to provide insights on droplet to particle conversion in atmospheric non equilibrium plasma discharges through a deep investigation of plasma and particle characteristics.

Here, we present the analysis of a plasma multiphase reactor for the synthesis of inorganic materials through the reduction of droplets containing metal salts: in particular, this study is focused on  $\text{AgNO}_3$ . Plasma-assisted reduction of  $\text{AgNO}_3$  has been well-studied in liquid-batch configurations [19,20,42–44] and offers straightforward chemistry to benchmark new results. Since the first reported experiment of plasma assisted reduction of Ag ions in liquid solution carried out by Gubkin [45], several works have investigated APP treatment of  $\text{AgNO}_3$  containing solution, pointing out the key role of solvated electrons [20,46] and of hydrogen radical [47] in the synthesis of NPs. The plasma through-flow reactor used in this work and previously described [29,48] enables the formation of a volumetric discharge where droplets are injected and processed continuously. In our process, the effluent from the dielectric barrier discharge (DBD) plasma reactor, where silver nitrate containing droplets react in the plasma discharge, were monitored on-line using scanning mobility particle spectroscopy (SMPS). Particle size distribution for different operating conditions were analyzed comparing the SMPS results with chemical and -morphological analysis (UV-Vis spectroscopy and transmission electron microscopy, TEM) carried out on particles collected through electrostatic precipitation and filtering. A control experiment was performed removing the liquid water in order to assess the role of solvated electrons in plasma-assisted reduction of metal salts. Based on our findings, the reduction mechanism of  $\text{AgNO}_3$  dissolved in the liquid droplet in contact with the plasma discharge is proposed and discussed.

## 3.2 Materials & Methods

### 3.2.1 Plasma reactor

The atmospheric pressure DBD plasma reactor used in this study is composed of a quartz tube (OD 6.35 mm, ID 4 mm) equipped with two external clamp ring electrodes (aluminium, OD 12 mm, ID 6.35 mm) with a distance of 30 mm in between. The powered electrode (HV) is upstream with respect to the gas flow, while the downstream one (GND) is connected to ground. A schematic of the plasma reactor is reported below in Figure 3.4. Power is supplied to the gas by an alternate current high voltage (HV) power supply (PVM500-2500, Information Unlimited) operating at 34 kHz. The gas discharge occurred primarily between the electrodes inside the quartz tube, avoiding possible contamination from etching due to direct plasma-metal interaction [49].

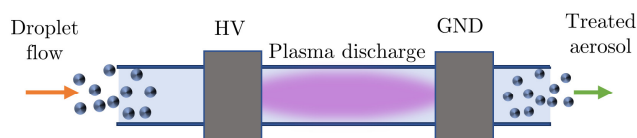


Figure 3.4 Non-equilibrium atmospheric DBD flow through reactor.

Silver nitrate containing droplets were produced by a Venturi-effect collision nebulizer (BLAM, CH Technologies Inc.) and carried by 1300 standard cubic centimetre per minute (sccm) of argon (Ar) flow in the DBD reactor. The collision nebulizer was filled with 40 ml of 1 mM  $\text{AgNO}_3$  (Alfa Aesar 99.9%) solution prepared by dissolving the silver salt in high purity water (HPLC grade, Fischer Chemical) at room temperature. The nebulizer was weighed before and after 30 minutes of use to estimate a liquid flow rate of 0.04 ml/min of the  $\text{AgNO}_3$  solution. All gas flow rates were controlled using digital mass flow controllers (MFC, El-Flow, Bronkhorst).

### 3.2.2 Electrical characterization

Current-voltage (I-V) characteristics of the discharge were measured using a high voltage (P6015A, Tektronix, Inc.) and a current probe (6585, Pearson Electronics) coupled with a real-time controlled oscilloscope (DPO4043, Tektronix, Inc.). Charge deposition for each cycle was calculated by measuring the voltage drop across a 0.94 nF capacitor connected in series with the plasma reactor on the grounded (GND) branch of the circuit. Data were recorded using a MatLab® (MathWorks, Inc.) script. Following the well-established approach detailed in literature [50,51], Lissajous figures were then used to calculate the plasma power and the amount of charge deposited during the each period .

Renderings of the setups used for particle synthesis and electrical characterization is reported in Figure 3.5

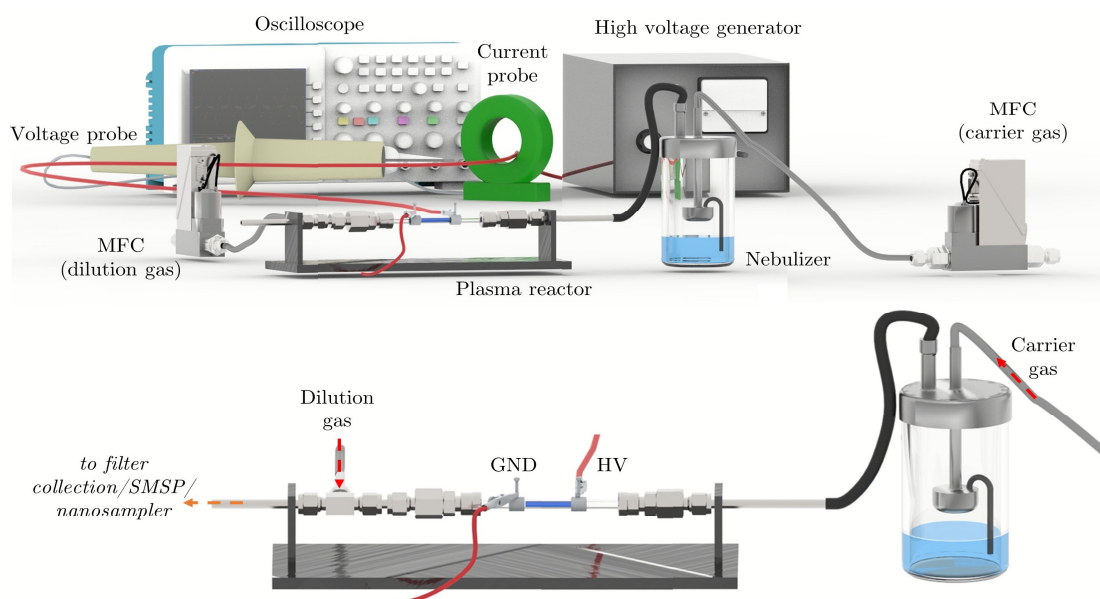


Figure 3.5 Rendering of the setup used for particle synthesis and process electrical characterization.

### 3.2.3 Droplets characterization

The size distribution of the droplet flow at the exit of the nebulizer was quantified using a light diffraction technique (Spraytec, Malvern), based on the analysis of diffraction patterns produced by the interaction of a He-Ne laser with droplets. The incident laser beam passes through the aerosol flow and the resulting light intensity is measured by a photodetector. The instrument correlates the measured light intensity to the angle of diffraction to calculate

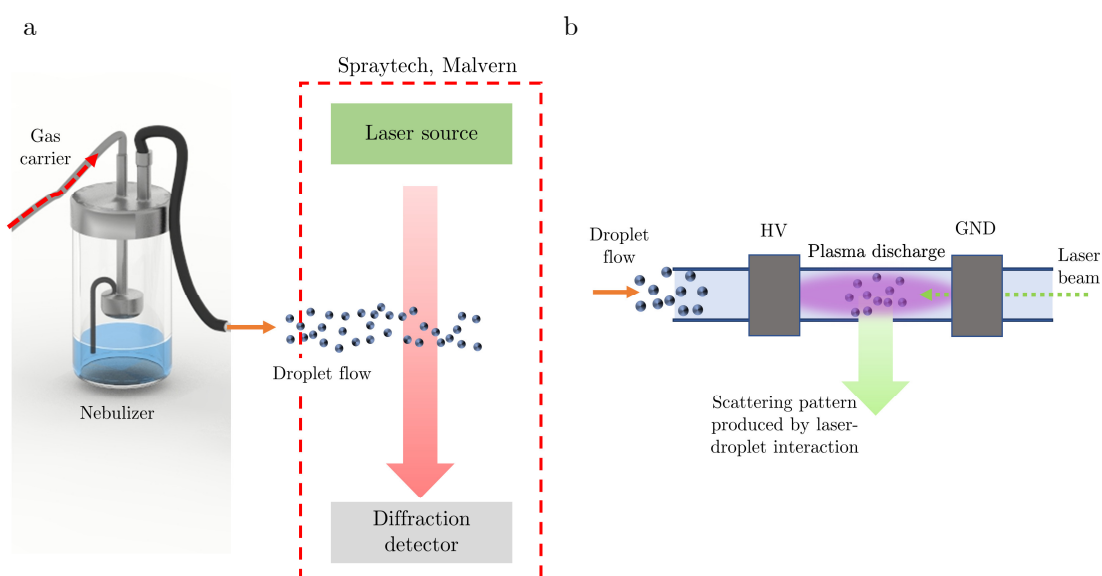


Figure 3.6 Experimental setup used for: a) droplet size characterization; b) droplet flow track inside the DBD reactor.

the droplet sizes, providing a volumetric droplet distribution under the Fraunhofer approximation. Measurements were made on the aerosol flow expanding in open air at the inlet and the outlet of the plasma reactor, as reported in the schematic in Figure 3.6a. The number droplet size distribution was then calculated from the volumetric droplet size distribution, assuming spherical droplets.

In addition, observations of droplet transport in the reactor was carried out using an inexpensive laser pointer (LT-301, 532 nm, 500 mW) fixed near the outlet of the reactor, as shown in Figure 3.6b. The particle flow was tracked inside the plasma reactor exploiting the laser scattering pattern with the aim of providing qualitative information on the presence of water droplets both inside and at the exit of the reactor.

## 3.2.4 Nanoparticle characterization

### 3.2.4.1 Aerosol size distribution

On-line particle size distributions were obtained using a SMPS, consisting of an electrostatic classifier (Model 3080N, TSI Inc.) fitted with a nano differential mobility analyser (DMA, Model 3085, TSI Inc.) and an ultrafine condensation particle counter (UCPC, Model 3776, TSI Inc.). A simple schematic of the setup used during experimental tests is reported in Figure 3.7a. Before particles are classified with the aim of separating them by size, the sample aerosol is conducted through a bipolar charger ( $^{85}\text{Kr}$   $\beta$ -source) to impart a known charged particle distribution [52,53]. Once charged, the sample aerosol is carried by a 3000 sccm dilution flow (sheath flow) through the DMA, where charged particles are conducted under action of a high-voltage electric field. This allows classification of the aerosol flow by the particle electrical mobility based on a balance of the particle drag and coulombic attraction. The result is a monodispersed aerosol flow. The SMPS instrument calculates the particle diameter, assuming a singly charged, spherical particle. Finally, the particle number concentration of monodisperse aerosol flow is obtained by the condensation particle counter. This routine is performed for varying electric field strengths within the DMA in order to classify a spectrum of particle electrical mobility. To prevent discharges from taking place within the DMA, the plasma reactor effluent was diluted with an 8000 sccm flow of nitrogen ( $\text{N}_2$ ).

It is well understood that particle electrical mobility depends on charge and particle geometry. According to Fuchs [53] particle charge distribution in a bipolar environment, it is unlikely for particles smaller than 100 nm in diameter to obtain multiple charges. Thus, we can assume singly charged particles at the outlet of the bipolar charger. Non-spherical particles have larger associated drag forces compared to a similar volume spherical one. As a consequence, it's worth highlighting that the instruments could overestimate particle diameters for non-spherical particles.

For each operating condition, at least four sets of data were obtained and then average concentration and its standard deviation were calculated.

### 3.2.4.2 Chemo-morphological characteristics of synthesized NPs

Particles were collected for a duration of 30 minutes by PTFE filters (0.45  $\mu\text{m}$  pore size, JHWP-2500, Millipore Sigma) placed downstream the reactor (Figure 3.7b). The particle-laden filters were dipped into a 1% w/w poly vinyl alcohol solution (PVA, Acros Organics) for two hours before placing the solution in a sonication bath for one hour. UV-Vis absorbance analysis was carried out on prepared colloids to measure the presence of the localized surface plasmon resonance (LSPR) peak characteristic to Ag NPs. Prepared samples stored in quartz cuvette (1 cm path length) were analyzed using a UV-Vis spectrometer (UV-1800, Shimadzu) subtracting the background of the pristine solution to the acquired absorbance spectra.

The morphological characteristics of the plasma synthesized particles were investigated by means of transmission electron microscopy (TEM, FEI Tecnai F30 300kV). Particles were collected on the TEM grids using an electrostatic precipitator (Nanometer Aerosol Sampler, TSI) operating at a voltage potential of -9.6 kV for three minutes (Figure 3.7c). The effluent from the reactor was diluted with 1000 sccm of  $\text{N}_2$  in order to prevent undesired corona discharges. The post-processing analysis of particle diameter (projected area diameter) from TEM images was carried out using Image-J software.

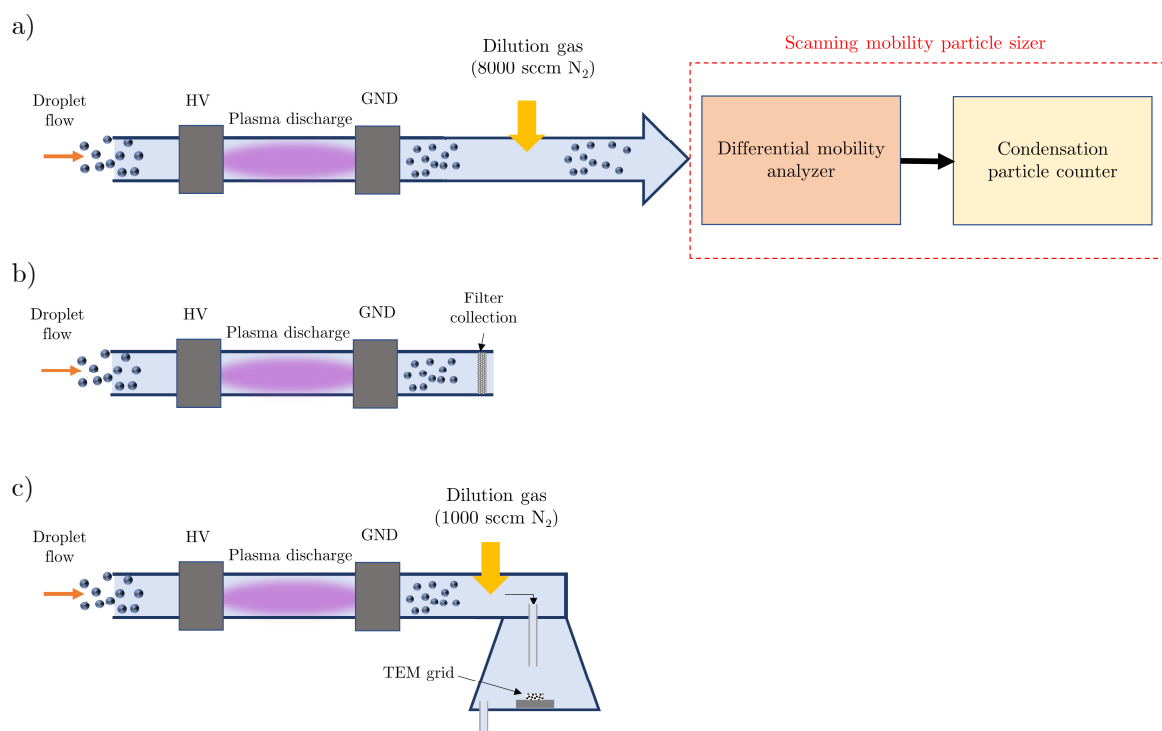


Figure 3.7 Experimental setups used for the synthesized particle analysis through: a) SMSP; b) particle filtering; c) particle collection on TEM grid.

### 3.2.5 Diffusion dryer experiment

In order to perform a control experiment where dried  $\text{AgNO}_3$  particles were introduced in the discharge, the water content of aerosol was reduced using a diffusion dryer with silica bead packing (DD, Model 3062, TSI Inc.) placed between the nebulizer and the plasma reactor (Figure 3.8). The particles were conducted into the plasma discharge by the carried gas flow. Following the methodology described above, UV-Vis and SMPS analysis were carried out. In the following, the experiments carried out with diffusion dryer are referred as “diffusion dryer” tests, while when droplet flow reached the plasma reactor and reacted with the plasma discharge, the achieved data are labelled as “standard experiment”.

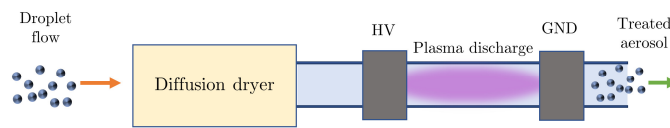


Figure 3.8 Experimental setup used for the diffusion dryer experiments.

### 3.2.6 Effect of residence time

With the aim of changing the residence time of droplet inside the discharge, gas flow rate through the reactor was modified. Keeping constant the flow rate used for liquid nebulization, the aerosol flow was split using a needle valve coupled with a vacuum pump placed before the plasma reactor (Figure 3.9): the residence time was then increased or decreased, by purging part of the 1300 Ar carrying the droplets or introducing an additional Ar dilution flow through a mass flow controller, respectively.

All the data related to material properties and characteristics [54,55] used for the Results and Discussion section are reported in Table 3.2 of the Appendix.

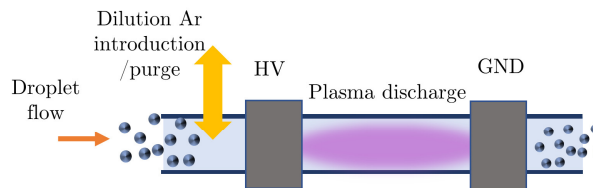


Figure 3.9 Experimental setup used for the investigation of the effect of the residence time.

### 3.3 Results & Discussion

For all experiments, plasma electrical characteristics were measured: particularly, power and charge supplied by the high voltage generator were monitored through Lissajous analysis. It is worth mentioning that the power was kept constant for all the experiments carried out in this work, allowing a comparison between the achieved results. Lissajous plot for the experimental condition when 1300 sccm of droplet aerosol were injected in the reactor and the gas discharge took place between the two electrodes (plasma on) is compared to the control condition with no discharge (plasma off) in Figure 3.10.

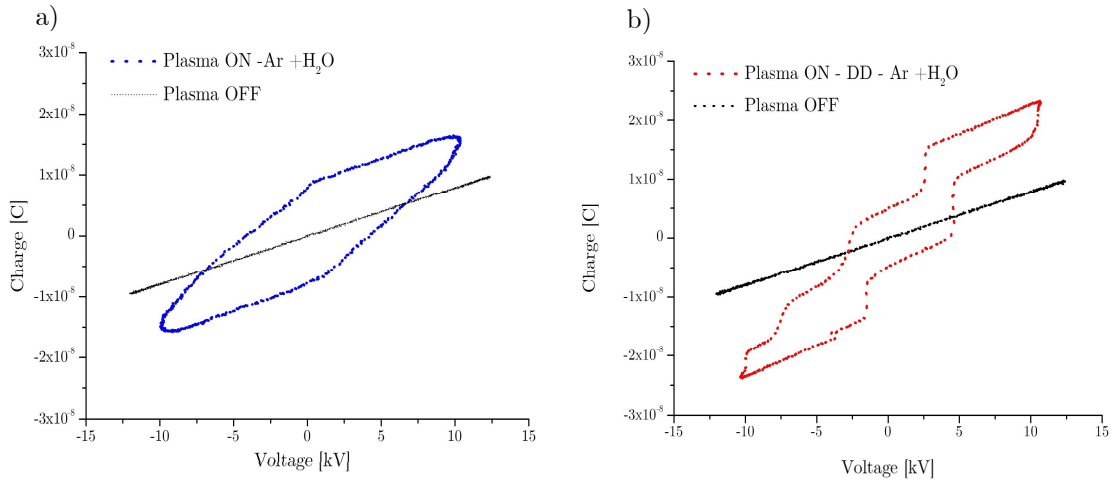


Figure 3.10 Charge-voltage (Lissajous) plots for the standard (a) and diffusion dryer experiment(b).

The energy supplied by the kHz power supply for each cycle was calculated from the area enclosed in the Lissajous plot for a single plasma period (29.4  $\mu$ s). The mean plasma power was then evaluated through the product of the energy supplied for each cycle and the driving voltage frequency. The net power calculated by subtracting the power when the plasma was off (0.4 mW) for the experiments carried out is reported in Table 3.1. The charge injected for each cycle was evaluated by measuring the charge difference during the plasma on phases (both positive and negative half period), as detailed by Mussard et al. [51]. As reported in Table 1, in the standard experiments were droplets were introduced in the discharge, charge transfer during the positive and negative half cycle was estimated +22.8 nC and - 24.4 nC, respectively.

	Standard experiment						Diffusion dryer
Flow rate [sccm]	650	1000	1300	1600	1900	2200	1300
Residence time [ms]	35	23	17	14	12	10	17
$d_{off}$ [nm]	35.5 $\pm$ 0.2	36.4 $\pm$ 0.2	38.1 $\pm$ 0.4	37.1 $\pm$ 0.4	38.5 $\pm$ 0.1	38.8 $\pm$ 0.2	38.2 $\pm$ 0.1
$d_{on}$ [nm]	24.3 $\pm$ 0.6	25.0 $\pm$ 0.3	26.5 $\pm$ 0.2	27.6 $\pm$ 0.1	29.1 $\pm$ 0.1	31.2 $\pm$ 0.6	33.8 $\pm$ 0.5
$\gamma_v$	0.92 $\pm$ 0.05	0.92 $\pm$ 0.04	0.90 $\pm$ 0.07	0.80 $\pm$ 0.04	0.77 $\pm$ 0.02	0.65 $\pm$ 0.05	0.42 $\pm$ 0.04
Power	7.0 W						6.7 W
Charge	+ 22.8 nC/- 24.4 nC						+40.7 nC/- 38.9 nC

Table 3.1 Summary of particles geometric mean distribution and conversion efficiencies as a function of process parameters for droplets experiments and diffusion dryer experiments.

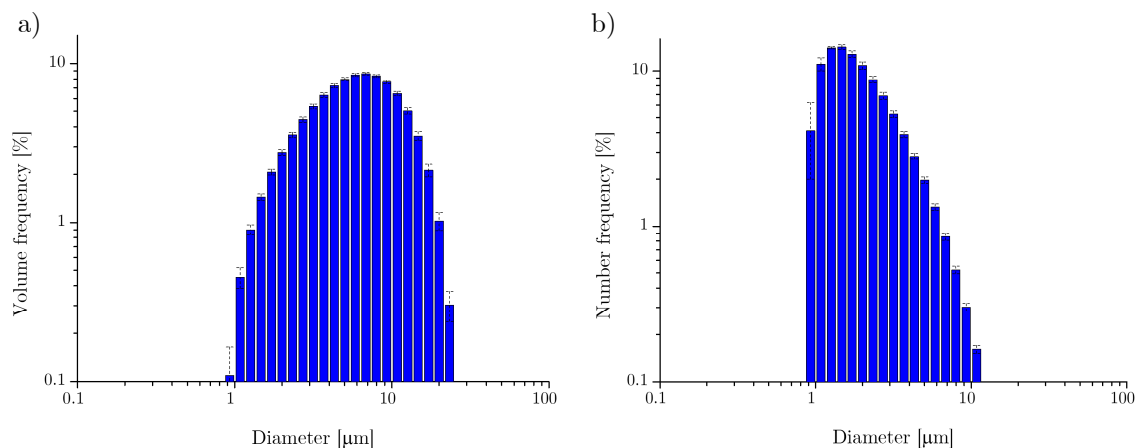


Figure 3.11 a) Droplet volume and b) number distribution at the exit of the nebulizer/inlet of the plasma reactor.

To gain insight of the plasma-aerosol process, knowledge of the injected droplet size distribution is necessary. Results from the light diffraction analysis showed a unimodal droplet volume fraction distribution, centred at  $6.83 \mu\text{m}$  (Figure 3.11a). Assuming spherical droplets, the volume fraction was converted to a number-weighted size distribution for comparison with the particle size distribution obtained from the SMPS [56]. Figure 3.11b shows the number-weighted size distribution of the aerosol droplets, centred between  $1.26$  and  $1.47 \mu\text{m}$ . The deviation from the log-normal shape of number-weighted distribution can be ascribed to several factors. Firstly, it's worth remembering that volume-based measurements are affected by larger error for small particle diameter: in terms of volume, in fact, a single  $10 \mu\text{m}$  droplet is equivalent to  $10^3$   $1 \mu\text{m}$  particles. For this reason, while calculating the number length mean ( $D_{1,0}$ ) [57] and converting the experimental distribution to a number-weighted one, the error becomes more significant. Moreover, as reported in the Materials and Methods section, measurements were carried out at the exit of the nebulizer in open air ( $20^\circ\text{C}$ ,  $41\%$  U.R.). Since the liquid evaporation rate is highly affected by droplet size and environmental humidity and temperature, jet propagation in open air could have slightly affected the measurement. Finally, we found that the droplet size distribution is dependent on the gas flow rate through the nebulizer (not shown). For this reason, all experimental conditions were carried out at a fixed carrier gas flow rate of  $1300 \text{ sccm}$  Ar through the nebulizer.

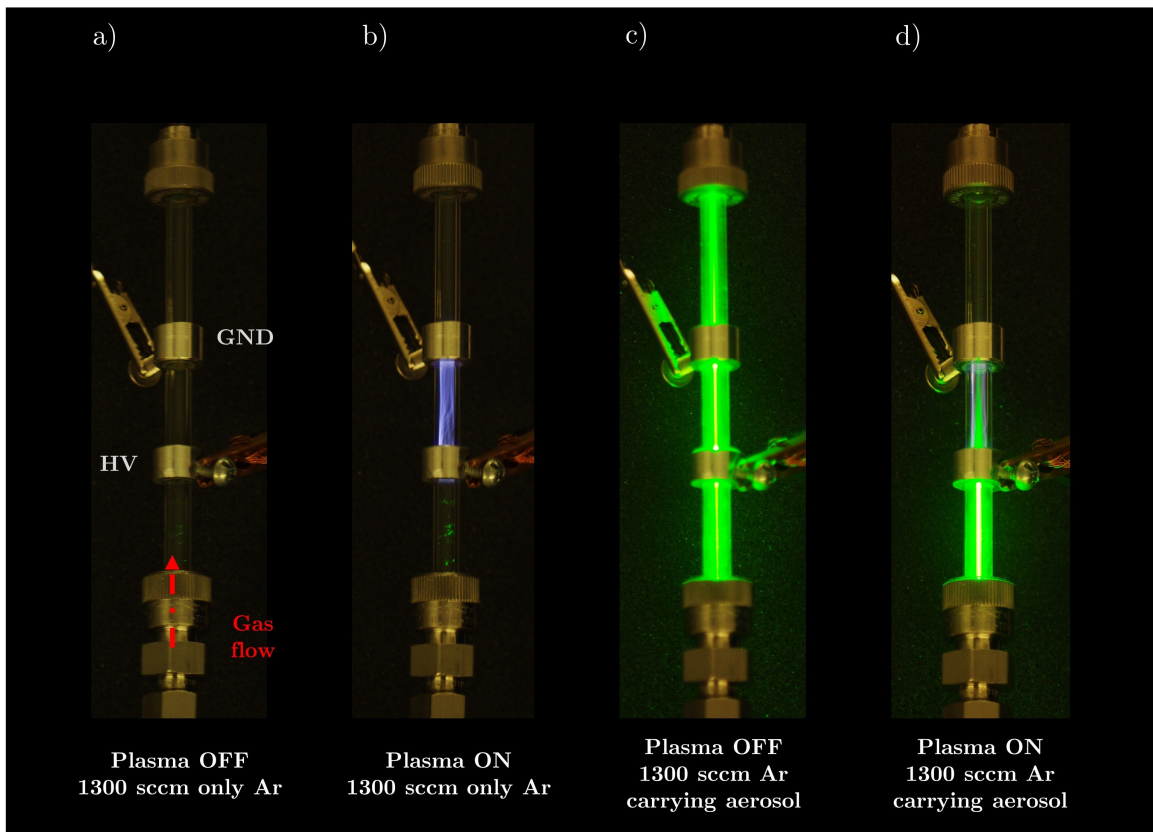


Figure 3.12 Laser diffraction pictures of the plasma reactor under different operating condition: a) Plasma OFF, 1300 sccm Ar; b) Plasma ON, 1300 sccm Ar; c) Plasma OFF, 1300 sccm Ar carrying droplet aerosol; d) Plasma ON, 1300 sccm Ar carrying droplet aerosol.

In this work, we exploited the light scattering due to droplets to qualitatively visualize the presence of droplets through the reactor at various experimental conditions. As detailed by [58,59], laser techniques have been applied to solid and liquid aerosols for flow visualization in research and industrial applications, notably from environmental and atmospheric sciences. The images presented in Figure 3.12a-b outlined the absence of laser diffraction when only Ar was flown into the reactor also when the plasma was turned on. Conversely, the presence of droplets carried by the Ar flow produced a visible difference, reaching to the outlet of the reactor volume while the plasma was off (Figure 3.12c). Droplet evaporation was observed when the plasma was on, due to interaction with plasma species. Evaporation through the plasma can be followed by analysing the laser diffraction pattern inside the plasma discharge, which suggested a progressively decrease along the plasma discharge (cone-shape green scattered light). By the end of the reactor, scattering was no longer observed meaning that nearly all the droplets evaporated. Further pictures reporting the presence of the droplet at the exit of the plasma reactor are reported in the Appendix section (Figure 3.20a).

Concerning droplet evaporation, it's widely known that the diameter ( $D$ ) reduction as a function of time ( $t$ ) can be described according to the D-squared law ( $D^2(t)=D_0^2-ct$ ) where the evaporation coefficient  $c$  is function of environmental condition (temperature, humidity)

and liquid physical properties (e.g. molar mass, density) [60]. Besides thermal effects, Maguire et al. [61] claimed that droplets exposed to an RF plasma exhibited a high evaporation coefficient, attributed to electron bombardment and charge-induced instability [33]. The authors observed a mean reduction of droplet diameter by 3  $\mu\text{m}$  under exposure to He-Ne plasma discharge for  $\sim 120 \mu\text{s}$ . In our experiments, the residence time was long enough to lead to almost complete evaporation by the end of the plasma discharge due to the small droplet size. Experimental reactor gas temperature ( $\sim 400\text{-}420 \text{ K}$ ) was found to agree with what has been reported by Maguire [61] and can be accounted in our case as the major contribution to water evaporation.

To provide insight into the mechanism behind droplet-particle conversion, the effluent of the reactor was analyzed using SMPS techniques and the obtained particle size distributions were fitted with log-normal curve to obtain geometric mean diameters under the assumption of spherical particles (Table 1). The effluent of untreated droplet flow was characterized by a log-normal particle size distribution centred at 38.07 nm (Figure 3.13a), which was ascribed to solid  $\text{AgNO}_3$  particles formed as a result of total droplet evaporation. As detailed in the Materials and Methods section in fact, the  $\text{N}_2$  dilution of 8000 sccm that was added to the aerosol flow prior to the SMPS was likely responsible for the observed enhanced droplet evaporation.

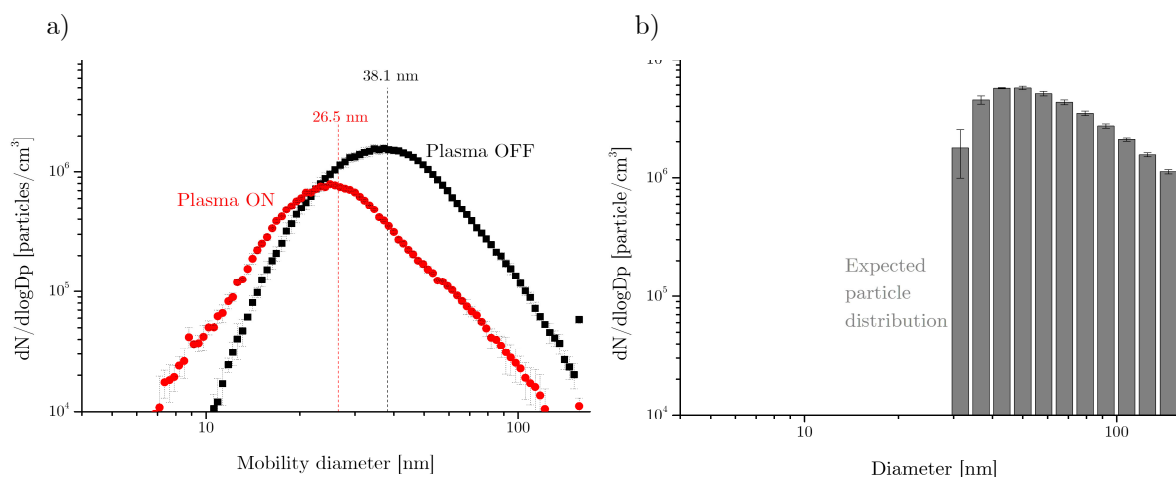


Figure 3.13 a) Particle distribution obtained from during plasma on and off experiments; b) Simulation of expected salt particle distribution from 1 mM  $\text{AgNO}_3$  containing droplets evaporation; c) Schematic of proposed conversion mechanism.

In the cases of SMPS measurement of particles from liquid aerosol flow, best practises from aerosol science field suggest that droplet evaporation may take place inside the DMA, effectively changing the particle size in-flight. In this perspective, preliminary tests were carried out by placing a diffusion dryer between the outlet of the plasma reactor and SMPS with the aim of confirming complete droplet evaporation. Comparison of measured particle size distributions indicated that there were no significant differences between experiments

with and without the diffusion dry, showing that the nitrogen dilution and the DMA sheath flow induced complete droplets evaporation. Since the experiments were carried out as a control test and result does not provide information useful for the following discussion, particle distributions are reported in the Appendix section (Figure 3.21).

Results obtained from SMSP analysis of the “plasma off” condition can be discussed according to the widely accepted mechanism of salt containing droplet evaporation. As a solute-containing droplet undergo evaporation, solid particles begin to nucleate and grow until all the water is removed leaving only the non-volatile residue. According to literature [62,63], the size of residual particles can be evaluated from the initial droplet size and the initial salt concentration, assuming spherical and dense particles [60]. The expected residue particle diameter  $d_{\text{off}}$ , can be calculated using Equation (3-1). As shown, the size is directly proportional to the droplet diameter ( $d_{\text{droplet}}$ ) and the cube root of the product of salt concentration ( $[AgNO_3]$ ) and its molar mass ( $M_{AgNO_3}$ ) divided by the salt density ( $\rho_{AgNO_3}$ ).

$$d_{\text{off}} = d_{\text{droplet}} \cdot \left( \frac{[AgNO_3] \cdot M_{AgNO_3}}{\rho_{AgNO_3}} \right)^{1/3} \quad (3-1)$$

Using this approach, the measured droplet size distribution was used to calculate the expected particle size distribution while the plasma was turned off, as reported in Figure 3.13b. The expected distribution was centred at 42 nm, which is in good agreement with the SMPS results. The slight differences between the two distributions can be attributed to the respective errors associated with the different measurement techniques. It’s also important to remember that the contribution of smallest droplets is much more significant for the number-weighted distribution than for volume-weighted distribution, as already discussed above.

Following the same approach, SMSP measurement were carried out on the effluent of plasma treated droplets. The analysis outlined a shift in the particle size number distribution to lower diameters with respect to the “plasma off” experiment, reporting a distribution centred at 26.5 nm and a reduction in total particle concentration by about a factor two (Figure 3.13a). The decrease in particle concentration can be related to losses associated with electrophoretic and thermophoretic effects [49]. We can argue that the reduction of the mean particle diameter was due to the electrochemical reduction of  $AgNO_3$  to  $Ag$  facilitated by the electrons and other energetic species present in the discharge according to Reaction R1 already reported in literature[19].



The reduction of aqueous silver ions induced a decrease of the volume of the non-volatile residues, which led to the formation of smaller diameter particles. In this perspective, reduction efficiency can be studied by comparing the amount of reacted material with respect

to the ideal one (total AgNO<sub>3</sub> conversion). Process conversion efficiency ( $\eta_v$ ) can be introduced and evaluated using Equation (3-2), where  $d_{\text{exp}}$  is the experimentally measured particle diameter and  $d_{100\% \text{ conversion}}$  is the expected particle diameter under the hypothesis of a complete silver nitrate reduction.

$$\eta_v = \left( \frac{d_{\text{off}}^3 - d_{\text{exp}}^3}{d_{\text{off}}^3 - d_{100\% \text{ conversion}}^3} \right) \quad (3-2)$$

$d_{100\% \text{ conversion}}$  can be calculated according to Equation (3-3).

$$d_{100\% \text{ conversion}} = d_{\text{droplet}} \left( \frac{[\text{AgNO}_3] \cdot M_{\text{Ag}}}{\rho_{\text{Ag}}} \right)^{1/3} \quad (3-3)$$

where  $M_{\text{Ag}}$  and  $\rho_{\text{Ag}}$  are the molar mass and the density of silver, respectively. Following this approach, the expected particle diameter can be expressed as a function of the conversion efficiency, droplet diameter and precursor concentration (Equation (3-4)).

$$d_{\text{exp}} = d_{\text{droplet}} \left\{ \frac{[\text{AgNO}_3] \cdot M_{\text{Ag}}}{\rho_{\text{Ag}}} \left[ 1 - \eta_v \left( 1 - \frac{\rho_{\text{AgNO}_3} \cdot M_{\text{Ag}}}{\rho_{\text{Ag}} \cdot M_{\text{AgNO}_3}} \right) \right] \right\}^{1/3} \quad (3-4)$$

According to the calculations, the expected Ag particle mean diameter under the hypothesis of complete conversion is 24.4 nm. Comparing the results obtained with the SMPS data, one can observe a small difference between the expected value, and the measured value, 26.5 nm. This may be due to incomplete conversion of the silver nitrate and/or lower electrical mobility within the SMPS as a consequence of non-ideal particle geometry. The results thus far agree with the hypothesis proposed by Tsumaki et al. [35] and Yu-Ming Su et al. [36] that one droplet results in one particle during plasma treatment. Supporting their claims, the respective authors reported that synthesized particle diameters are strongly correlated with the initial salt concentration and droplet size.

The proposed plasma conversion mechanism is summarized in Figure 3.14. Briefly, the process begins with droplet generation from a solution containing soluble metal precursor, which in this work was achieved through liquid nebulization. The droplet is carried through the plasma discharge where interactions with high energy species take place, most importantly free electrons. There are evidences in the literature [15] that suggest that electrons produced by plasma discharge have a capacity to solvate in water and reduced metal ions dissolved in the liquid phase [64]. Upon solvation, the electron driven reactions proceed with the chemistry outlined previously and discussed later in further depth. Through various modes of heat transfer, nearly all the droplets have evaporated by the end of the plasma region as observed by the absence of light diffraction (Figure 3.12d).

With the aim to confirm the  $\text{AgNO}_3$  reduction in the plasma discharge and supporting the conversion mechanism proposed above, UV-Vis absorbance measurements were carried out on samples prepared from suspended Ag particles collected by filtering the effluent of the plasma reactor. Absorbance spectra of plasma treated particles dispersed in a 1% PVA solution in water exhibited the characteristic LSPR peak of Ag NPs at approximately 400 nm, whereas no peak was detected for the untreated aerosol, as shown in Figure 3.15a. PVA serves a capping agent that allows the Ag particles to be well-dispersed in water. Comparing the absorbance spectra of particles dispersed in pure water and in the PVA solution, the plasmon resonance peak intensity was more pronounced in the 1% PVA solution. Ag particles in pure water seemed to aggregate as suggested by the lower absorbance and the small red shift in the absorbance spectrum [19,65].

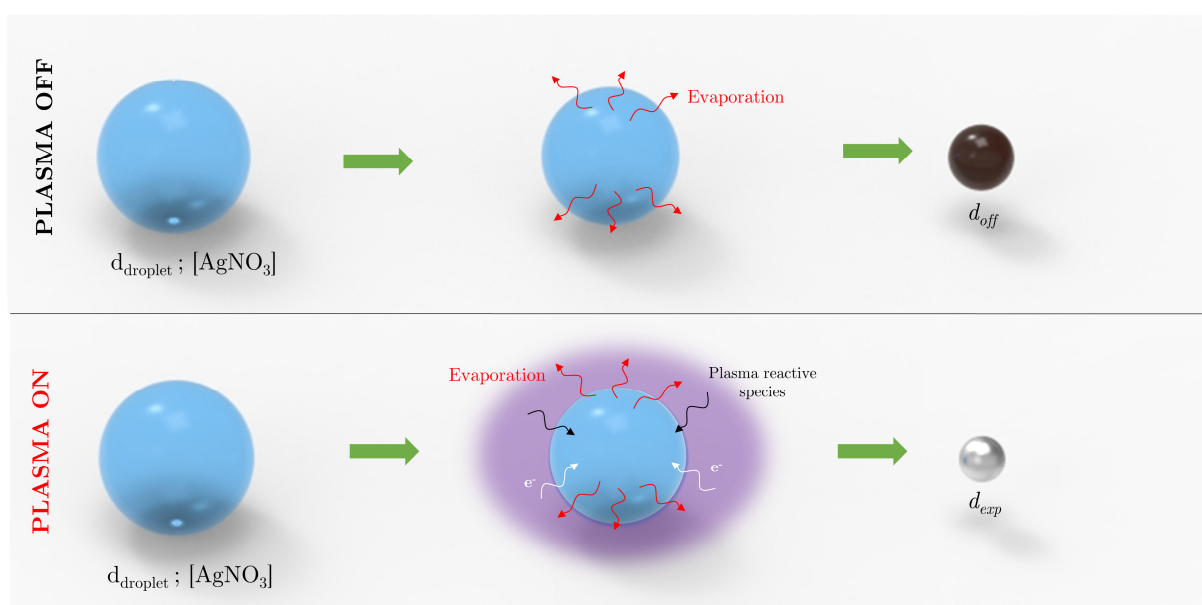


Figure 3.14 Schematic of proposed conversion mechanism.

Morphological characteristics of synthesized particles were further investigated through TEM imaging. The particles were collected on a copper TEM grid using a planar electrostatic precipitator. Collected images, shown in Figure 3.15b, revealed the synthesis of both single and aggregated spherical NPs. Single particle diameters were found to be in the range of 10-35 nm, while larger aggregates (60–70 nm) composed of primary particles in the range of 12-20 nm were observed. Aggregation of primary particles likely took place during the synthesis process as a result of collisions due to temperature gradients and particle charging. High resolution images showed crystalline particles, with an average lattice distance of 0.2 nm characteristic to Ag (200) d-spacing pattern [66]. The observed polycrystalline structure of the synthesized particles can be explained by the presence of multiple nucleation centres, eventually collapsing into a single particle during the plasma treatment and droplet evaporation.

The particle size distribution obtained from the analysis of TEM images is reported in Figure 3.16a where is also compared with the SMPS results. From the size measurement carried out on about 200 particles, synthesized Ag NPs exhibited a log-normal size distribution centred at  $23.3 \pm 0.25$  nm that is in good agreement with the SMPS results. Further analysis is made by comparing the expected particle size distribution calculated from Equation (3-4) under the hypothesis of 100%, the experimental plasma-treated distribution and the distribution obtained from the TEM images. The expected distribution and the SMPS results were compared in Figure 3.16b, with an artificial reducing factor of 2 to mirror the particle losses observed from the initial experiments. The expected and SMPS distributions were overlapped for small particle diameters and also in sizes around the mean value. We observed two main regions of interest in terms of differences in particle concentration (outlined with texture in Figure 3.16b). With the expected distribution as

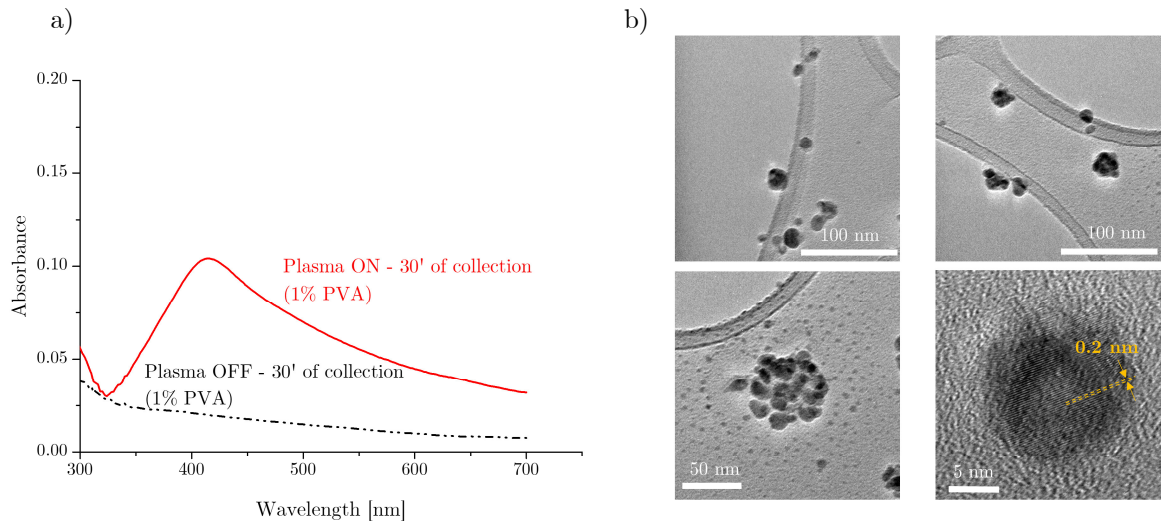


Figure 3.15 a) UV-Vis analysis of colloid from filter collected particles; b) TEM images of particle collected from plasma treated droplet flow.

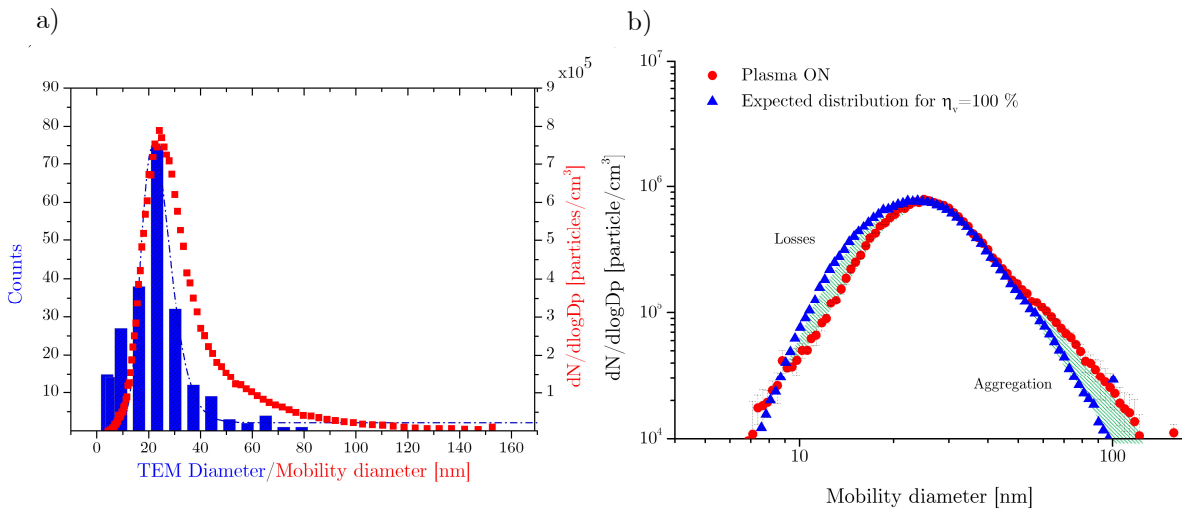


Figure 3.16 a) Particle size distribution according to TEM analysis and SMPS; b) Comparison of particle size distribution for plasma treated aerosol and simulation of expected Ag NPs distribution.

reference, the SMPS data showed lower particle concentration for particle sizes in the 9-19 nm range, while higher particle concentrations were found between 55 and 120 nm. These results suggested that aggregation of smaller particles may have taken place within the system resulted in an underestimation of concentration for larger particles. These findings were in good agreement with TEM image which showed 53-75 nm aggregates composed of 12-17 nm particles as reported in Figure 3.15b. In light of this, the formation mechanism based on droplet to particle conversion proposed above is further corroborated.

### 3.3.1 Influence of water droplets in the silver reduction

Literature reported that several complex processes occur at plasma-solution interface, involving both gas and liquid phase reactions [2,5]. Several works claimed that liquid composition [6], gas environment [67], plasma configuration [44] can strongly affect the chemical and morphological characteristics of synthesized particles. Among the reactive species responsible for nanoparticles synthesis in plasma treated solutions, solvated electrons ( $e^-_{aq}$ ) are currently accounted as the most important and therefore worthy of deep investigations [15,16,67].

Ghosh et al. [20] reported the importance of solvated electrons in a batch process producing Ag particles while highlighting the role of liquid water as a dissolution media. Based on that, we hypothesized that the presence of water droplets is key in the production of Ag particles from  $AgNO_3$  containing droplet in the aerosol phase. We tested this hypothesis by removing the water droplets leaving primarily salt particles in the aerosol flow injected in the plasma reactor. For these experiments, characterization of the chemical and morphological characteristics of the treated particles were made using SMPS and Uv-Vis absorbance measurements. To achieve water droplet removal, a diffusion dryer was placed between the nebulizer and the plasma reactor. The diffusion dryer operated by removing water vapor in the flow which caused a larger driving force for evaporation due to vapor liquid equilibrium. In this configuration, the absence of light scattering (Figure 3.20b, Appendix section) before the plasma discharge and the comparison with the standard case were the droplet flow reach the plasma reactor served as evidence for droplet removal. It's important to mention here that the power delivered to the plasma reactor remained around 7 W (Table 3.1), enabling a true comparison with the standard experiment (droplet flow through the reactor). The Lissajous plots of the diffusion dryer experiment is reported in Figure 3.10b. As already discussed in literature, with respect to the standard experiment, we observed that the breakdown voltage was smaller in value while the discharge current, and therefore the deposited charge, was higher. Results from the SMPS measurements when the plasma was off (Figure 3.17a) supported that the water evaporation led to the formation of  $AgNO_3$  salts with a similar size distribution to the 'plasma off' experiments in the standard case (Table 3.1, Figure 3.13a). The reduction in particle concentration for the diffusion dryer experiments can be ascribed to particle loss inside the dryer volume.

When the plasma was switched on, the resulting particle distribution showed a shift of the mean size to 33.8 nm from 38.2 nm measured during the plasma off. The observed shift in the particle size distribution was less than the one observed for the standard experiment while the distribution reshaping can be ascribed to the various particle loss mechanisms that occurred in the discharge. It should be pointed out that the mean size shift was related to a large decrease in big particle concentration, while for smaller diameter the distribution shape was almost constant. As discussed by Jidenko et al. [68], submicron salt particles introduced in an atmospheric DBD plasma discharge undergo charging and are removed due to the applied electric field. The authors also reported that filtering efficiency strongly depends on plasma parameters and particle diameter, where smaller particles obtain less charge than larger particles. Similar results have been obtained by Intra et al. [69] using a negative DC corona charger able to remove particles between 32 and 63 nm with efficiency up to 70%. Our results were found in good agreement with this explanation, suggesting the lack of particle reduction for the DD experiment.

In order to validate the hypothesis of particle removal and lower distribution shift rate suggested by the SMPS results, particles were collected and suspended in 1% PVA solution. The reduced rate of conversion was confirmed by the absence of any LSPR peak in the analyzed colloid (Figure 3.17b). Since the diffusion dryer experiments exhibited lower particle concentration by a factor of three, we also compared the UV-Vis absorbance for particles collected in the standard experiment for 10 minutes for better comparison of spectra by collecting the same number of particles. Results reported in Figure 3.17b outlined the lack of characteristics peak absorbance spectra, suggesting that when water was removed the reduction of  $\text{AgNO}_3$  scarcely occurred, thus highlighting the role of liquid water in the reduction process.

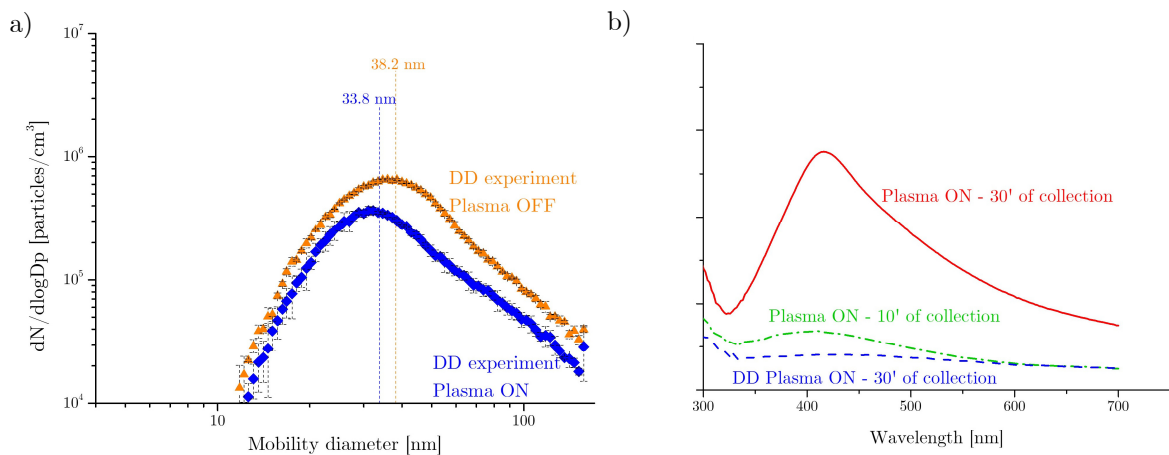


Figure 3.17 a) Comparison between particle distribution obtained from SMPS during plasma on and off between droplet and diffusion dryer(DD) experiments; b) UV-Vis analysis of colloid from filter collected particles for DD experiments (30' of collection time) and comparison with droplets cases (10' and 30' of collection time).

### 3.3.2 Process efficiency

An analysis approach based on the proposed conversion mechanism and the mean particle diameter was employed to investigate the reduction performances our plasma process. The conversion efficiency ( $\eta_V$ ) was evaluated using Equation (3-4), using the geometric mean of particle size during plasma off ( $d_{off}$ ) and plasma on ( $d_{on}$ ) as variables. The reduction in

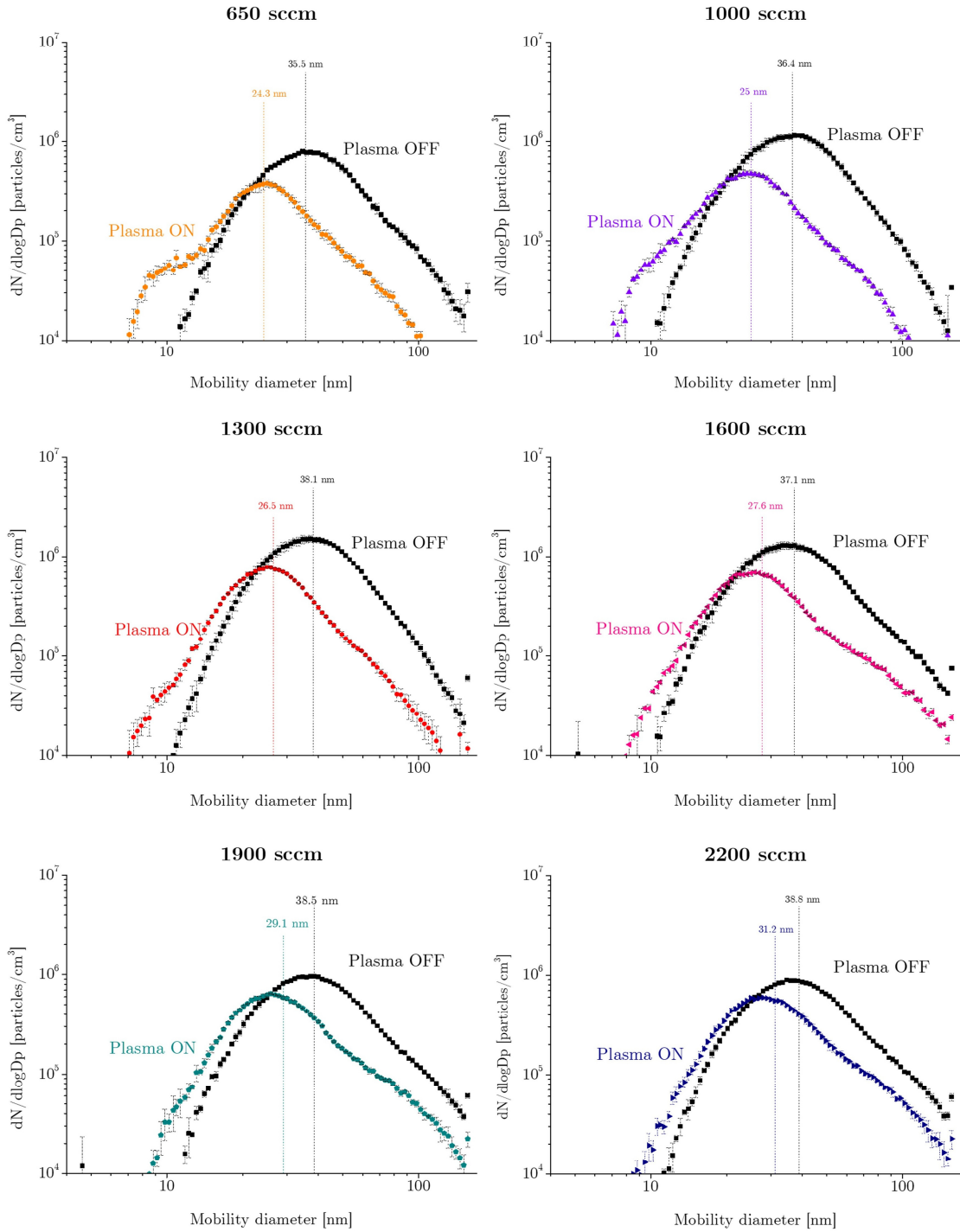


Figure 3.18 Particle size distribution for different flow rate/residence time.

particle volume from experiments was compared to the ideal volumetric difference between  $\text{AgNO}_3$  and Ag particle, where 100% conversion was achieved (Equation (3-2)).

This approach assumed a log-normal particle size distribution and therefore calculations carried out using the geometric mean diameter can be slightly affected by aggregation and losses. Nevertheless, based on the measured particle distributions, our proposed metric for conversion efficiency can be applied to the results in order to gain insight on the role of process parameters on the synthesized Ag NPs. In this framework, residence time through the plasma reactor was varied and resulting size distributions were measured using the SMPS (reported in Figure 3.18). Geometric mean diameters ( $d_{\text{off}}$ ,  $d_{\text{on}}$ ), reported in Table 1, were then used to calculate the conversion efficiency of all the experimental conditions. As reported in Figure 3.19, with a flow rate of 1300 sccm through the reactor, we achieved the highest conversion efficiency of 90%. Deviations from the theoretical maximum value of 100% can be ascribed to the effect of loss and aggregation on the geometric mean diameter. Decreasing the flow rate did not result in significant improvements in conversion efficiency. Higher flow rates outlined a progressive drop in efficiency down to 65% at 2200 sccm, suggesting limited  $\text{AgNO}_3$  conversion.

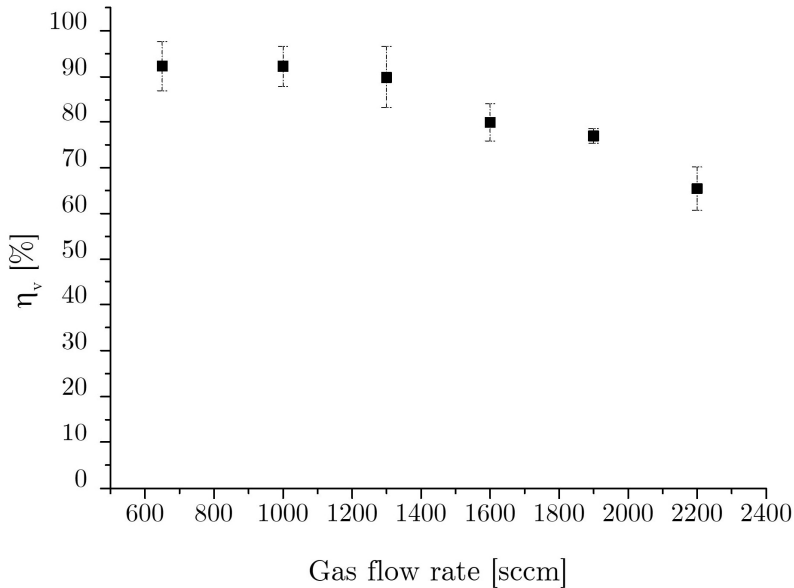


Figure 3.19 Conversion efficiency of the synthesis process for different gas flow rate.

Once demonstrated the conversion mechanism behind particle formation in droplet-plasma reactor, reduction mechanism was investigated. Plasma-assisted reduction was primarily attributed to an electron driven mechanism [20] and, in light of this, Faradaic efficiency can be calculated to evaluate the process performances from an electrochemical point of view [70]. In the field of DC microplasma processing, faradaic efficiency has been assessed comparing the number electrons injected in the system to the mass of elements reduced in the reactor to the theoretical number of ions that could have been reduced

assuming complete chemical reduction. It is worth mentioning that reported results are based on important assumptions and are strongly influenced by experimental setup and reaction pathway that often involve side reactions at the plasma-liquid interface [71]. To our knowledge, no studies have applied faradaic approach to investigate the efficiency of DBD plasma reactor at atmospheric pressure. From an ideal point of view, if one can measure the amount of electrons introduced in a DBD discharge, like Ghosh et al. [20] did for the DC microplasma, the efficiency can be evaluated as the ratio between the electrons employed in the reagent-product conversion (under the hypothesis of complete reactions) and the electrons in the discharge. The method applied here is based on the approach proposed by Ghosh and on the hypothesis that every electron introduced in the plasma discharge could reduce silver ion through Reaction R1. Under the assumption of electron balance across the electrodes of the reactor for each period, the amount of electrons injected for each cycle was obtained by measuring the amount of charge injected for each cycle ( $Q_{\text{cycle}}$ ) during the positive and negative half cycle from the Lissajous figures. The theoretical mass flow rate of produced silver,  $\dot{m}_{\text{Ag,F}}$ , was then calculated using Equation (3-5) adapted from [20] for our continuous flow process, where  $z$  is the number of electrons involved in the reaction (1 for Ag reduction) and  $F$  is Faraday's constant

$$\dot{m}_{\text{Ag,F}} = \left( \frac{Q_{\text{cycle}}}{zF} \right) \cdot M_{\text{Ag}} \quad (3-5)$$

The experimental silver mass produced by our process,  $\dot{m}_{\text{Ag,SPMS}}$ , can be estimated by integrating the mass particle distribution under the hypothesis of spherical Ag particles, according to Equation (3-6).

$$\dot{m}_{\text{Ag,SMSP}} = \sum_{i=1}^{64} \frac{\pi \cdot D_{p,i}^3}{6} \cdot \rho_{\text{Ag}} \cdot N_i, \text{ where } i=[4.61 \text{ nm}, 4.78, \dots, 156.6 \text{ nm}] \quad (3-6)$$

where  $D_{p,i}$  and  $N_i$  are respectively particle diameter and concentration relative to each bin of the SMPS instrument [72].

Finally, faradaic efficiency (FE) can be evaluated:

$$\text{FE} = \frac{\dot{m}_{\text{Ag,SMSP}}}{\dot{m}_{\text{Ag,F}}} \quad (3-7)$$

The calculated efficiency was found around 1%, a significantly smaller value compared to other microplasma experiments in the literature. Since the reasons behind these differences are multiple and unexplored, couple of hypotheses are proposed and discussed in the following. It should be mentioned that the equivalent circuit of an electrochemical plasma cell is completely different from the one of a DBD reactor, where parasitic elements must be taken into account due to the AC driven voltage. Dielectric and Joule losses cause an overestimation of the electrons available in the plasma discharge calculated from the number

of charge/electrons injected. It's also worth mentioning that the higher electron density found in DC microplasma discharges ( $10^{14}$ - $10^{15}$   $\text{cm}^{-3}$ , [73,74]) with respect to AC flow-through DBD ( $10^{11}$ - $10^{12}$   $\text{cm}^{-3}$ , see [61,75] and Chapter 4) can be responsible for lower electron solvation and reduced reaction rate. Moreover, the electrons in the plasma discharge are mostly driven by the electric field to the powered electrodes and only a fraction of them solvate through the interface of floating-potential droplet and react with the Ag ions in the water. This characteristics of DBD is different with respect to DC microplasma, where the liquid act as an anode of the electrochemical cell and the electrons are mainly driven towards the liquid surface by the electric field. Finally, as already discussed, side reactions both in the gas and in the liquid phase could be accounted for the reduction of Faradaic efficiency. The results achieved on Faradaic efficiency in DBD flow-through reactor appear preliminary and based on important assumptions. Therefore, future simulation and experimental studies need to be carried out to investigate droplet-plasma interaction and shedding some light on the electrochemical, diffusive and convective phenomena taking place in this environment.

### 3.4 Conclusions

In this present work, we have carried out a detailed study of a flow-through APP reactor examining the different effect of process parameters on salt containing droplet to particle conversion. The interaction between plasma discharge and the  $\text{AgNO}_3$  containing liquid aerosol was studied analysing reactor effluent using SMSP, UV-Vis and TEM diagnostic techniques. For a given gas carrier flow rate and precursor concentration, when droplet flow was exposed to the plasma discharge the mean particle mobility diameter shifted from 38.1 to 26.5 nm. The decrease of mean particle size can be ascribed to  $\text{AgNO}_3$  reduction and Ag NPs production, as corroborate by Ag LSPR peak of synthesized particles obtained from UV-Vis analysis. Results of TEM analysis are consistent with SMSP results, outlining the synthesis of crystalline Ag NPs both dispersed and aggregated. The comparison of droplet size measurement and NPs distribution indicated a strong correlation which suggests a plasma driven droplet to particle conversion mechanism. In this framework, we have analyzed the performance of the reactor using a conversion efficiency approach based on the comparison of distribution shift. While the reduction of the flow rate did not affect the efficiency, which reached an asymptote ( $\sim 90\%$ ), starting around 1300 sccm, the decrease of droplets residence time strongly limited the conversion rate. In order to prove the role of solvated electron in the chemical pathway driving  $\text{AgNO}_3$  reduction, liquid water was removed and dried  $\text{AgNO}_3$  salts were introduced in the plasma reactor. The key role of liquid phase reactions in plasma assisted Ag synthesis was highlighted by the lack of precursor reduction form UV-Vis analysis and the limited shift in particle distribution from SMSP data. Whereas the results that have been presented give insight into the in-flight and in-situ synthesis of inorganic nanoparticle assisted by aerosol plasma, further efforts need to be devoted to the investigation of plasma-droplet interaction with the aim of tuning the chemomorphological properties of synthesized particles. In this perspective, plasma assisted nanomaterial processing could take advantage of a better understanding of the role of droplet size distribution and precursor concentration on the complex phenomena taking place inside the discharge.

## 3.5 References

- [1] Magureanu M, Lukes P and Pârvulescu V I 2012 *Plasma Chemistry and Catalysis in Gases and Liquids* (John Wiley & Sons)
- [2] Mariotti D, Patel J, Švrček V and Maguire P 2012 Plasma-liquid interactions at atmospheric pressure for nanomaterials synthesis and surface engineering *Plasma Process. Polym.* **9** 1074–85
- [3] Velusamy T, Liguori A, Macias-Montero M, Padmanaban D B, Carolan D, Gherardi M, Colombo V, Maguire P, Svrcek V and Mariotti D 2017 Ultra-small CuO nanoparticles with tailored energy-band diagram synthesized by a hybrid plasma-liquid process *Press Plasma Process. Polym.* 1–39
- [4] Kaushik N, Kaushik N, Linh N, Ghimire B, Pengkit A, Sornsakdanuphap J, Lee S-J and Choi E 2019 Plasma and Nanomaterials: Fabrication and Biomedical Applications *Nanomaterials* **9** 98
- [5] Chen Q, Li J and Li Y 2015 A review of plasma-liquid interactions for nanomaterial synthesis *J. Phys. D. Appl. Phys.* **48**
- [6] Liguori A, Galligani T, Padmanaban D B D B, Laurita R, Velusamy T, Jain G, Macias-Montero M, Mariotti D and Gherardi M 2018 Synthesis of Copper-Based Nanostructures in Liquid Environments by Means of a Non-equilibrium Atmospheric Pressure Nanopulsed Plasma Jet *Plasma Chem. Plasma Process.* **38** 1209–22
- [7] Richmonds C and Sankaran R M 2008 Plasma-liquid electrochemistry: Rapid synthesis of colloidal metal nanoparticles by microplasma reduction of aqueous cations *Cit. Appl. Phys. Lett. J. Appl. Phys. Appl. Phys. Lett* **93** 131501–64103
- [8] Švrček V, Mariotti D and Kondo M 2010 Microplasma-induced surface engineering of silicon nanocrystals in colloidal dispersion *Appl. Phys. Lett.* **97** 3–6
- [9] Mariotti D and Sankaran R M 2010 Microplasmas for nanomaterials synthesis *J. Phys. D. Appl. Phys.* **43** 323001
- [10] Huang X Z, Zhong X X, Lu Y, Li Y S, Rider A E, Furman S A and Ostrikov K 2013 Plasmonic Ag nanoparticles via environment-benign atmospheric microplasma electrochemistry *Nanotechnology* **24**
- [11] Du C and Xiao M 2014 Cu<sub>2</sub>O nanoparticles synthesis by microplasma. *Sci. Rep.* **4** 7339
- [12] Velusamy T, Liguori A, Macias-Montero M, Padmanaban D B, Carolan D, Gherardi M, Colombo V, Maguire P, Svrcek V and Mariotti D 2017 Ultra-small CuO nanoparticles with tailored energy-band diagram synthesized by a hybrid plasma-liquid process *Press Plasma Process. Polym.* 1–39
- [13] Pârvulescu V I, Magureanu M and Lukes P 2012 *Plasma Chemistry and Catalysis in Gases and Liquids*
- [14] Bruggeman P J, Kushner M J, Locke B R, Gardeniers J G E, Graham W G, Graves

- D B, Hofman-Caris R C H M, Maric D, Reid J P, Ceriani E, Rivas D F, Foster J E, Garrick S C, Gorbanev Y, Hamaguchi S, Iza F, Jablonowski H, Klimova E, Kolb J, Krcma F, Lukes P, Machala Z, Marinov I, Mariotti D, Thagard S M, Minakata D, Neyts E C, Pawlat J, Petrovic Z L, Pflieger R, Reuter S, Schram D C, Schröter S, Shiraiwa M, Tarabová B, Tsai P A, Verlet J R R, von Woedtke T, Wilson K R, Yasui K and Zvereva G 2016 Plasma-liquid interactions: a review and roadmap *Plasma Sources Sci. Technol.* **25** 53002
- [15] Rumbach P, Bartels D M, Sankaran R M and Go D B 2015 The solvation of electrons by an atmospheric-pressure plasma. *Nat. Commun.* **6** 7248
- [16] Rumbach P, Bartels D M and Go D B 2018 The penetration and concentration of solvated electrons and hydroxyl radicals at a plasma-liquid interface *Plasma Sources Sci. Technol.* **27** 115013
- [17] Rumbach P, Griggs N, Sankaran R M and Go D B 2014 Visualization of electrolytic reactions at a plasma-liquid interface *IEEE Trans. Plasma Sci.* **42** 2610–1
- [18] Gopalakrishnan R, Kawamura E, Lichtenberg A J, Lieberman M A and Graves D B 2016 Solvated electrons at the atmospheric pressure plasma-water anodic interface *J. Phys. D. Appl. Phys.* **49**
- [19] Vos C De, Baneton J, Witzke M, Dille J and Sankaran R M 2017 A comparative study of the reduction of silver and gold salts in water by a cathodic microplasma electrode *J. Phys. D. Appl. Phys.* **50** 105206
- [20] Ghosh S, Hawtof R, Rumbach P, Go D B, Akolkar R and Sankaran R M 2017 Quantitative Study of Electrochemical Reduction of Ag<sup>+</sup> to Ag Nanoparticles in Aqueous Solutions by a Plasma Cathode *J. Electrochem. Soc.* **164** D818–24
- [21] Patel J, Němcová L, Maguire P, Graham W G and Mariotti D 2013 Synthesis of surfactant-free electrostatically stabilized gold nanoparticles by plasma-induced liquid chemistry *Nanotechnology* **24** 245604
- [22] Sun D, Turner J, Jiang N, Zhu S, Zhang L, Falzon B, McCoy C, Maguire P, Mariotti D and others 2019 Atmospheric Pressure Microplasma for Antibacterial Silver Nanoparticle/Chitosan Nanocomposites With Tailored Properties
- [23] Rumbach P, Lindsay A and Go D B 2019 Turing patterns on a plasma-liquid interface *Plasma Sources Sci. Technol.*
- [24] Nolan H, Sun D, Falzon B G, Maguire P, Mariotti D, Zhang L and Sun D 2019 Thermoresponsive nanocomposites incorporating microplasma synthesized magnetic nanoparticles—Synthesis and potential applications *Plasma Process. Polym.* **16** 1–7
- [25] Ghosh S, Bishop B, Morrison I, Akolkar R, Scherson D and Mohan Sankaran R 2015 Generation of a direct-current, atmospheric-pressure microplasma at the surface of a liquid water microjet for continuous plasma-liquid processing *J. Vac. Sci. Technol. A Vacuum, Surfaces, Film.* **33** 021312
- [26] Bouchard M, Laprise-Pelletier M, Turgeon S and Fortin M A 2017 Efficient and Rapid Synthesis of Radioactive Gold Nanoparticles by Dielectric Barrier Discharge

- [27] Ghosh S, Liu T, Bilici M, Cole J, Huang I-M, Staack D, Mariotti D and Sankaran R M 2015 Atmospheric-pressure dielectric barrier discharge with capillary injection for gas-phase nanoparticle synthesis *J. Phys. D. Appl. Phys.* **48** 314003
- [28] Chiang W H and Sankaran R M 2008 In-flight dimensional tuning of metal nanoparticles by microplasma synthesis for selective production of diameter-controlled carbon nanotubes *J. Phys. Chem. C* **112** 17920–5
- [29] Sankaran R M, Holunga D, Flagan R C and Giapis K P 2005 Synthesis of blue luminescent Si nanoparticles using atmospheric-pressure microdischarges *Nano Lett.* **5** 537–41
- [30] Maguire P, Rutherford D, Macias-Montero M, Mahony C, Kelsey C, Tweedie M, Pérez-Martin F, McQuaid H, Diver D and Mariotti D 2017 Continuous In-Flight Synthesis for On-Demand Delivery of Ligand-Free Colloidal Gold Nanoparticles *Nano Lett.* **17** 1336–43
- [31] Mariotti D, Mahony C M O and Maguire P 2017 Method And Apparatus For Producing Nanoscale Materials 41
- [32] Kruszelnicki J A, Lietz A M and Kushner M J 2019 Atmospheric pressure plasma activation of water droplets *J. Phys. D. Appl. Phys.* **52** 355207
- [33] Bennet E D, Mahony C M O, Potts H E, Everest P, Rutherford D, Askari S, McDowell D A, Mariotti D, Kelsey C, Perez-martin F, Hamilton N, Maguire P and Diver D A 2016 Precision charging of microparticles in plasma via the Rayleigh instability for evaporating charged liquid droplets *J. Aerosol Sci.* **100** 53–60
- [34] Maguire P D, Mahony C M O, Kelsey C P, Bingham A J, Montgomery E P, Bennet E D, Potts H E, Rutherford D C E, McDowell D A, Diver D A and Mariotti D 2015 Controlled microdroplet transport in an atmospheric pressure microplasma *Appl. Phys. Lett.* **106** 224101
- [35] Tsumaki M, Shimizu Y and Ito T 2016 Size-controlled sub-micrometer spheroidized ZnO particles synthesis via plasma-induced processing in microdroplets *Mater. Lett.* **166** 81–4
- [36] Su Y, Kuo Y, Lin C and Lee S 2014 One-step fabrication of tetragonal ZrO<sub>2</sub> particles by atmospheric pressure plasma jet *Powder Technol.* **267** 74–9
- [37] Beier O, Pfuch A, Horn K, Weisser J, Schnabelrauch M and Schimanski A 2013 Low temperature deposition of antibacterially active silicon oxide layers containing silver nanoparticles, prepared by atmospheric pressure plasma chemical vapor deposition *Plasma Process. Polym.* **10** 77–87
- [38] Ranieri P, McGovern G, Tse H, Fulmer A, Kovalenko M, Nirenberg G, Miller V, Fridman A, Rabinovich A and Fridman G 2019 Microsecond-Pulsed Dielectric Barrier Discharge Plasma-Treated Mist for Inactivation of Escherichia coli In Vitro *IEEE Trans. Plasma Sci.* **47** 395–402
- [39] Burlica R, Grim R G, Shih K Y, Balkwill D and Locke B R 2010 Bacteria inactivation

- using low power pulsed gliding arc discharges with water spray *Plasma Process. Polym.* **7** 640–9
- [40] Kovalova Z, Leroy M, Kirkpatrick M J, Odic E and Machala Z 2016 Corona discharges with water electro-spray for *Escherichia coli* biofilm eradication on a surface *Bioelectrochemistry* **112** 91–9
- [41] Stancampiano A, Galligani T, Gherardi M, Machala Z, Maguire P, Colombo V, Pouvesle J-M M and Robert E 2019 Plasma and Aerosols: Challenges, Opportunities and Perspectives *Appl. Sci.* **9** 3861
- [42] Lee H, Park S H, Jung S-C, Yun J-J, Kim S-J and Kim D-H 2013 Preparation of nonaggregated silver nanoparticles by the liquid phase plasma reduction method *J. Mater. Res.* **28** 1105–10
- [43] Kondeti V S S K, Gangal U and Bruggeman P J 2017 The mechanism of reduction of  $\text{Ag}^+$  and formation of nanoparticles by a DC driven pulsed atmospheric pressure plasma jet *ISPC23 Proc.* 1–3
- [44] Shirai N, Uchida S and Tochikubo F 2014 Synthesis of metal nanoparticles by dual plasma electrolysis using atmospheric dc glow discharge in contact with liquid *Jpn. J. Appl. Phys.* **53** 0–5
- [45] Gubkin J 1887 Electrolytische Metallabscheidung an der freien Oberfläche einer Salzlösung *Ann. Phys.* **268** 114–5
- [46] Barauna J, Cunha-filho F J, Chiavone-filho O and Mota-lima A 2019 Reduction of Aqueous  $\text{Ag}^+$  Steered by Electrochemical Plasma: Connecting the Bulk pH Variation with the Reaction Pathways for Hydrated Electrons *J. Brazilian Chem. Soc.* **30** 1252–65
- [47] Kondeti V S S K, Gangal U, Yatom S and Bruggeman P J 2017  $\text{Ag}^+$  reduction and silver nanoparticle synthesis at the plasma–liquid interface by an RF driven atmospheric pressure plasma jet: Mechanisms and the effect of surfactant *J. Vac. Sci. Technol. A Vacuum, Surfaces, Film.* **35** 061302
- [48] Gorbanev Y, O’Connell D and Checkik V 2016 Non-Thermal Plasma in Contact with Water: The Origin of Species *Chem. - A Eur. J.* **22** 3496–505
- [49] Borra J P 2006 Nucleation and aerosol processing in atmospheric pressure electrical discharges: Powders production, coatings and filtration *J. Phys. D. Appl. Phys.* **39**
- [50] Pipa A and Brandenburg R 2019 The Equivalent Circuit Approach for the Electrical Diagnostics of Dielectric Barrier Discharges: The Classical Theory and Recent Developments *Atoms* **7** 14
- [51] Mussard M D V S, Foucher E and Rousseau A 2015 Charge and energy transferred from a plasma jet to liquid and dielectric surfaces *J. Phys. D. Appl. Phys.* **48** 424003
- [52] Wiedensohler A and Fissan H J 1991 Bipolar charge distributions of aerosol particles in high-purity argon and nitrogen *Aerosol Sci. Technol.* **14** 358–64
- [53] Fuchs N A 1963 On the stationary charge distribution on aerosol particles in a bipolar

ionic atmosphere *Geofis. Pura e Appl.* **56** 185–93

- [54] National Center for Biotechnology Information PubChem Database. Silver nitrate, CID=24470
- [55] National Center for Biotechnology Information PubChem Database. Silver, CID=23954
- [56] Allen T 1990 *Particle size measurement* (Springer)
- [57] International Organization for Standardization 2014 Representation of results of particle size analysis. Calculation of average particle sizes/diameters and moments from particle size distributions *BN ISO 9276-22014*
- [58] Smits A J and Lim T T 2010 *Flow Visualization - Techniques and Examples* (Imperial College Press)
- [59] Qian S-X, Snow J B, Tzeng H-M and Chang R K 1986 Droplets: Highlighting the Liquid-Air *Science (80-. )*. **231** 486–8
- [60] Hinds W C 1999 *Aerosol technology: properties, behavior, and measurement of airborne particles* (John Wiley & Sons)
- [61] Maguire P D, Mahony C M O, Kelsey C P, Bingham A J, Montgomery E P, Bennet E D, Potts H E, Rutherford D C E, McDowell D A, Diver D A and Mariotti D 2015 Controlled microdroplet transport in an atmospheric pressure microplasma *Appl. Phys. Lett.* **106** 224101
- [62] Chen T M and Chein H M 2017 Generation and Evaluation of Monodisperse Sodium Chloride and Oleic Acid Nanoparticles *Aerosol Air Qual. Res.* **6** 305–21
- [63] Stabile L, Trasserra C V, Agli G D and Buonanno G 2013 Ultrafine Particle Generation through Atomization Technique: The Influence of the Solution 1667–77
- [64] Wei-Hung C, Carolyn R and Sankaran R M 2010 Continuous-flow, atmospheric-pressure microplasmas: a versatile source for metal nanoparticle synthesis in the gas or liquid phase *Plasma Sources Sci. Technol.* **19** 34011
- [65] Kyrychenko A, Pasko D A and Kalugin O N 2017 Poly ( vinyl alcohol ) as a water protecting agent for silver nanoparticles : the role of polymer size and structure *Phys. Chem. Chem. Phys.* **19** 8742–56
- [66] Chen R, Nuhfer N T, Moussa L, Morris H R and Whitmore P M 2008 Silver sulfide nanoparticle assembly obtained by reacting an assembled silver nanoparticle template with hydrogen sulfide gas *Nanotechnology* **19** 455604
- [67] Rumbach P, Bartels D M, Sankaran R M and Go D B 2015 The effect of air on solvated electron chemistry at a plasma/liquid interface *J. Phys. D. Appl. Phys.* **48** 424001
- [68] Jidenko N and Borra J P 2012 Self-cleaning , maintenance-free aerosol filter by non-thermal plasma at atmospheric pressure *J. Hazard. Mater.* **235** 237–45
- [69] Intra P, Yawootti A and Rattanadecho P 2017 Corona Discharge Characteristics and

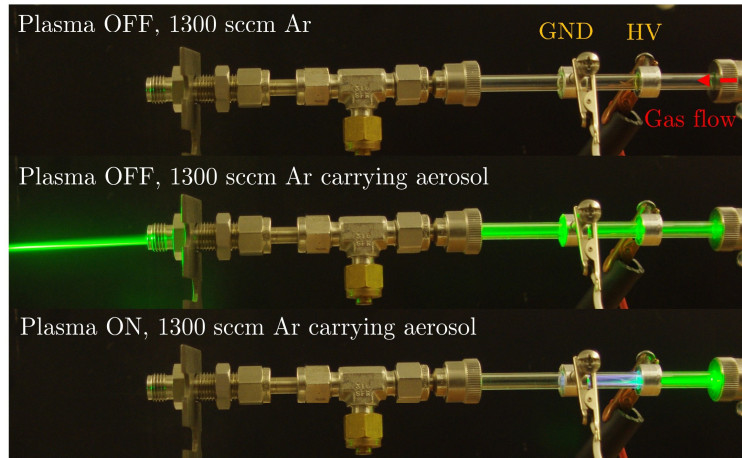
Particle Losses in a Unipolar Corona-needle Charger Obtained through Numerical and Experimental Studies *J. Electr. Eng. Technol.* **12** 2021–30

- [70] Kawamura H, Moritani K and Ito Y 1998 Discharge electrolysis in molten chloride: formation of fine silver particles *Plasmas Ions* **1** 29–36
- [71] Delgado H E, Radomsky R C, Martin D C, Bartels D M, Rumbach P and Go D B 2019 Effect of Competing Oxidizing Reactions and Transport Limitation on the Faradaic Efficiency in Plasma Electrolysis *J. Electrochem. Soc.* **166** E181–6
- [72] TSI Inc. 2012 *Aerosol statistics lognormal distribution and  $dN/d\log D_p$  - Application Note PR-001*
- [73] Chen Q and Shirai H 2012 Diagnostics of atmospheric pressure microplasma with a liquid electrode *Eur. Phys. J. D* **66** 1–5
- [74] Jamróz P and Żyrczyński W 2011 Spectroscopic characterization of miniaturized atmospheric-pressure dc glow discharge generated in contact with flowing small size liquid cathode *Plasma Chem. Plasma Process.* **31** 681–96
- [75] Oinuma G, Nayak G K and Bruggeman P 2016 Micro-water droplets in non-equilibrium atmospheric pressure plasma: Evaporation and OH induced chemistry *IEEE International Conference on Plasma Science (ICOPS)*

## 3.6 Appendix

### 3.6.1 Droplet flow visualization

a)



b)

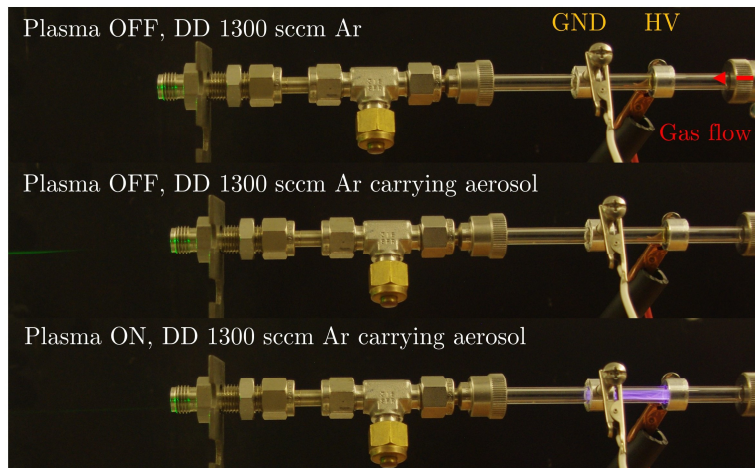


Figure 3.20 Laser diffraction pictures of the plasma reactor when carrier flow was introduced in the discharge region during the a) standard and b) diffusion dryer experiments.

Exploiting droplet laser scattering, aerosol flow through the reactor was monitored. When only Ar was flow through the reactor, no scattering pattern was recorded. Conversely, the presence of the droplets was corroborated by the light diffraction, both with plasma off and on. It's worth highlighting that when the plasma was turned on (as reported in above in the chapter), the reaction between the discharge and the droplet flow led to droplet evaporation and to a progressive decrease in the scattering signal through the reactor. The analysis was completed investigating the effect of droplet drying by means of a diffusion dryer. For this experimental configuration, the absence of any scattering patter confirmed the efficient

removal of liquid droplet before the reactor, allowing the introduction of solid salt residual in the discharge.

### 3.6.2 Physical database used for calculation

	Ag		AgNO <sub>3</sub>	
Density [g/cm <sup>3</sup> ]	$\rho_{\text{Ag}}$	10.49	$\rho_{\text{AgNO}_3}$	4.35
Molar mass [g/mol]	$M_{\text{Ag}}$	107.87	$M_{\text{AgNO}_3}$	169.87

Table 3.2 Physical characteristics of silver and silver nitrate.

Data collected in the Table 3.2 were used to complete the calculations discussed in the Material and Methods section.

### 3.6.3 Control experiment with aerosol drying before the DMA

With the aim of confirming that the effluent of the reactor (both during plasma on and off experiments) reached the DMA dried, the diffusion dryer was placed in between the outlet of the plasma source and the SMPS. The dried effluents were then analyzed using the DMA coupled with the CPC and particle distribution were plotted and compared with standard case. The results reported in Figure 3.21 outlined no statistically variation of mean particle

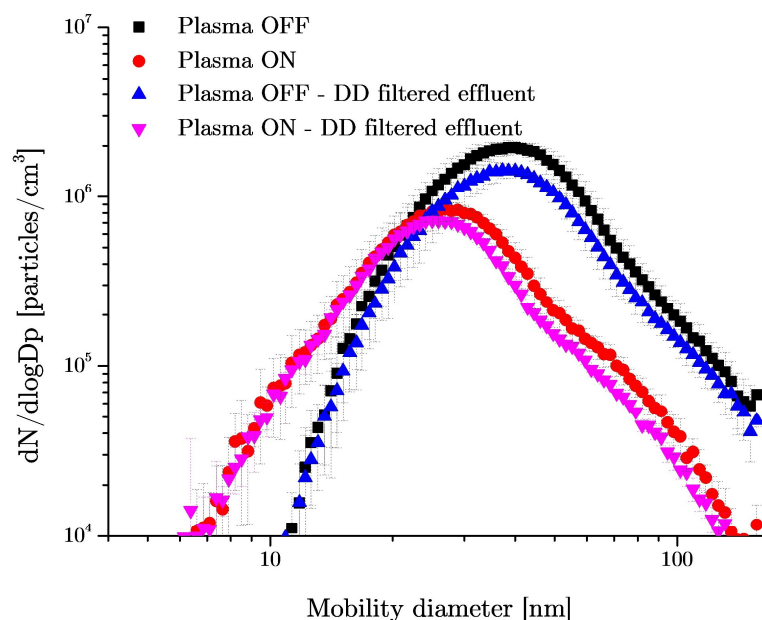


Figure 3.21 Particle size distribution for the control experiment where the effluent of the plasma reactor were dried before the SMSP analysis.

diameter. The slight reduction in particle concentration can be ascribed to losses in the diffusion dryer, as already discussed above.

**CHAPTER 4**  
**Experimental and simulative  
approach for the investigation of  
droplet evaporation in a flow-through  
non-thermal plasma reactor**

## 4.1 Introduction

Since the first years of the 19<sup>th</sup> century [1], the unique features of plasma discharges in or in contact with liquids have received a great attention, promoting the birth to specific fields of plasma chemistry and technology (e.g. plasma processing of nanomaterials [2], plasma medicine [3], plasma catalysis [4], plasma agriculture [5]). While offering enormous opportunities for multidisciplinary scientific studies [6], the multiphase nature of the plasma liquid-interface coupled with the complexity of non-equilibrium chemistry produced by gas discharges strongly limited industrial applications. Indeed, even if recent developments in diagnostic techniques [7] and simulative models [8–10] started to shed light on liquid-gas phase reactions, plasma and liquid chemistry is still an open and wide research field. With the aim of answering scientific questions about the interfacial phenomena, scientists arranged experimental setups already in use in the electrochemistry field, replacing one of the electrodes with a contact-less plasma cathode [11]. Thus, following the setup proposed by Schoenbach et al. [12,13], microplasma based reactors were widely employed to support nanomaterial processing and chemicals production [14,15], offering a green chemistry alternative to traditional techniques. While providing a wide range of versatility in terms of geometry, gas type and configurations, the limited area of interaction between gas and liquid phases reduced the process throughput. For this reason, as already discussed in the previous chapters, aerosol-plasma interaction has been proposed as an alternative to batch processes, with the aim increasing process efficiency and enabling in-situ particle and chemical delivery. In this framework, flow-through reactors were firstly proposed by Burlica [16,17] and Maguire [18,19] to support in-situ and on-demand delivery of chemicals or nanoparticles. The possibility to couple liquid aerosol injection with a plasma discharge has recently spurred the

growth of a completely new research field aimed at investigating plasma-aerosol interactions. Among the unanswered questions brought out in a recent opinion paper by Stancampiano et al. [20], the authors pointed out that a better understanding of the effect of the plasma discharge on droplet evaporation will enable a better design of plasma processes. Depending on the type of application, in fact, microdroplets can act as microreactors, where surface processes are enhanced with respect to the case of treating batch solutions, and the presence of the liquid phase is necessary both for an increase of reaction rate and for possibility to localized delivery reactive species. Conversely, other applications (e.g. coating deposition [21]) require a complete evaporation of a liquid precursor, in particular when higher crosslink degrees are required [22,23]. Unfortunately, scientific literature published so far on this subject is limited and comprehensive analyses dealing with these phenomena have not yet been carried out. A recent work published by Kruszelnicki et al. [24] deeply discussed on gas phase reaction and reactive specie solvation in microdroplet using 0D and 2D models, although the authors did not investigate droplet evaporation as a function of plasma parameters. While an interesting description of gas phase reactions was provided, the discussion on reactive species solvation in the liquid phase did not take into account droplet shrinking (because of model limitations) which is known to strongly affect Henry's law [25]. Conversely, Iqbal et al. [26–28] compared simulative results of droplet evaporation for different liquid aerosols exposed to a corona discharge, excluding plasma chemistry effects and validating the approach through droplet measurements at the exit of the reactor. These investigations however disregarded the driving mechanism of liquid evaporation and the model took into account only energy and mass balances, avoiding the possible effects of electron/ion impact and droplet fission (Coulombic fission), induced by charging and Rayleigh instabilities [29]. Nevertheless, a comparison of simulative model and obtained results suggested that the thermal contribution itself can be held responsible for droplet evaporation. Similar results were found by Bruggeman et al. [30], analysing single micrometric droplet evaporation in a RF through flow reactor. However, these results disagree with experimental data obtained by Maguire [18] who found an atypical size reduction when droplet were exposed to a RF plasma discharge. The lack of knowledge on the role of droplet (e.g. size, surface tension, temperature) and plasma (e.g. electron density, gas temperature, electron temperature, electric field) characteristics strongly limits the comparison of modelling [24] and simulative results [26], hindering technological development.

In this perspective, the aim of this work is to develop and describe an experimental and simulative approach to investigate droplet evaporation in plasma flow-through reactors. With the aim of tracking the droplet flow inside a non-thermal atmospheric discharge, we employed the laser induced Mie scattering generated by the interaction between the laser beam and the droplet flow. Following the approaches already applied in combustion engine science, the calibration of the system was carried out for different droplet concentrations and

the scattering intensity was measured by means of an optical probe located at  $90^\circ$  with respect to the aerosol flow. Once corroborated the linearity of the system, a semi-quantitative analysis of droplet concentration in different positions of the plasma reactor was completed. Achieved results were then compared with a 0D model used to simulated droplet evaporation as a function of environment temperature and vapour concentration.

## 4.2 Materials & Methods

### 4.2.1 Experimental setup

#### 4.2.1.1 Plasma reactor

To gain insights in plasma induced liquid evaporation, a flow-through DBD plasma reactor was coupled with an inexpensive laser source (LT-301, 532 nm, 5 mW) able to track droplet flow and concentration by exploiting Mie scattering. The plasma discharge was generated inside a quartz tube (OD 6.35 mm, ID 4 mm) between two metal ring electrodes powered by an alternate current (AC) high voltage (HV) generator (PVM500-2500, Information Unlimited). With the aim of evaluating aerosol concentration also in the area covered by the electrodes, metallic rings used in the experimental setup described in the previous chapter were replaced using conductive meshes. A droplet aerosol flow, generated by a Venturi effect nebulizer (BLAM, CH Technologies Inc.) and carried by 1300 sccm of Ar, was introduced in the quartz tube. The nebulizer, operated in recirculation mode, was filled with 40 ml distilled water (HPLC grade, Fisher Chemical) and a liquid flow rate of 0.04 ml/min was measured weighting the device before and after 30 minutes of operation. A schematic of the used experimental setup is reported in Figure 4.1.

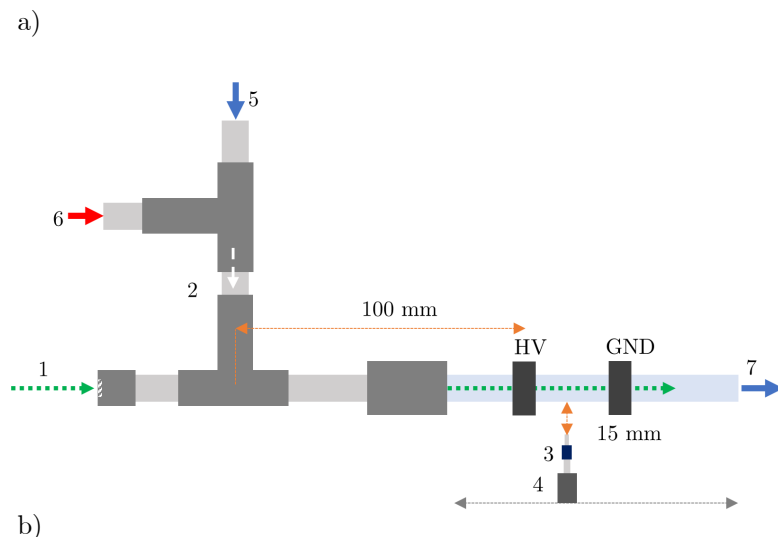
The electrical characteristics of the plasma discharge were measured by means of high voltage and current probes coupled with a digital oscilloscope (DPO4043, Tektronix, Inc.). Beyond voltage (V) and current (I) waveforms, the charge deposited during each period was acquired measuring the voltage drop across a capacitor (940 pF) placed on the ground (GND) branch of the circuit. As already widely reported, charge-voltage plots (Lissajous figure) were used to calculate either the charge deposited for each cycle [31] or the net discharge power [32,33].

Reactor temperature measurements were carried out by means of an infrared thermal camera (FLIR i3) used to measure the temperature of the quartz tube, assuming a quartz emissivity of 0.93. Obtained data were then used as input parameters for the simulation of droplet evaporation in the model described in the following section.

#### 4.2.1.2 Droplet size and concentration measurements

The droplet size measurement at the exit of the nebulizer was carried out acquiring the diffraction pattern produced by laser-particle interactions (Spraytec, Malvern). Ne-He laser induced diffraction was collected by a photodetector and data were analyzed using Spraytech software. The volumetric weighted size distribution was measured and analyzed for different operating conditions (i.e. gas flow rate).

Droplet concentration was assessed measuring the residual salt concentration obtained from aerosol evaporation through scanning mobility particle analysis. For this purpose, silver salt was dissolved in the liquid solution and was introduced in a diffusion dryer (Model 3062, TSI Inc.) used to decrease aerosol water content and lead to salt residual nucleation. As reported in literature, when limited solute concentration is used [34], a single particle is obtained from the evaporation of a salt containing droplet, enabling the possibility to correlate salt residual concentration to droplet concentration. For this reason, following the drying of the flow, the effluent gas was firstly introduced in a differential mobility analyser (DMA, Model 3080N, TSI, Inc.): polydisperse particles were charged using a radioactive bipolar charger ( $^{85}\text{Kr}$ ,  $\beta^-$  source) and then separated according to their electrical mobility using an electric field. Monodisperse particles flow was finally sent to an ultrafine condensation particle counter (CPC, Model 3776, TSI Inc.) where particle concentration was assessed. The filtered particle mobility diameter was automatically scanned over the 64 bins of DMA range (4.61-156.8 nm) and then correlated to concentration measured by CPC.



b)

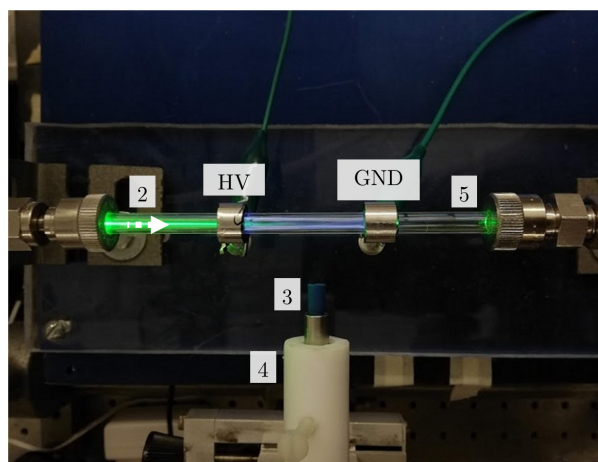


Figure 4.1 Schematic (a) and picture (b) of the plasma reactor and the experimental setup: 1) laser beam; 2) droplet flow; 3) optical probe; 4) holder; 5) droplet flow from the nebulizer; 6) humidified dilution flow; 7) effluent.

The setup developed for the in-situ analysis of droplet concentration is composed by the plasma reactor described above, where the laser beam was aligned with the quartz tube through an optical access located in the upstream region of the gas flow. An optical probe was connected to an UV-spectrometer (HR4000, Ocean Optics) and used to monitor the intensity of the 90° scattered light. The distance between the optical fiber and the reactor was kept constant at 15 mm while its position along the quartz tube was changed by means of a micrometric optical rail. All the data were collected for an exposure time of 100  $\mu$ s and postprocessed averaging at least 10 different acquisitions.

The scattered signal was correlated to the aerosol droplet concentration to confirm a linear relationship that has been previously reported. For this reason, a humidified Ar flow (100% RH) was introduced upstream the reactor with the aim of avoiding droplet evaporation during the mix of the two gas flows. The saturation pressure of the diluting gas was controlled using a home-made humidifier where liquid flow rate and temperature were adjusted using a syringe pump (KDS Legato 100, Fisher Scientific) and heat tape, respectively. The simplified schematic of the setup used for calibration is reported in Figure 4.2. All flow rates were controlled using a digital mass flow controller (El-Flow, Bronkhorst).

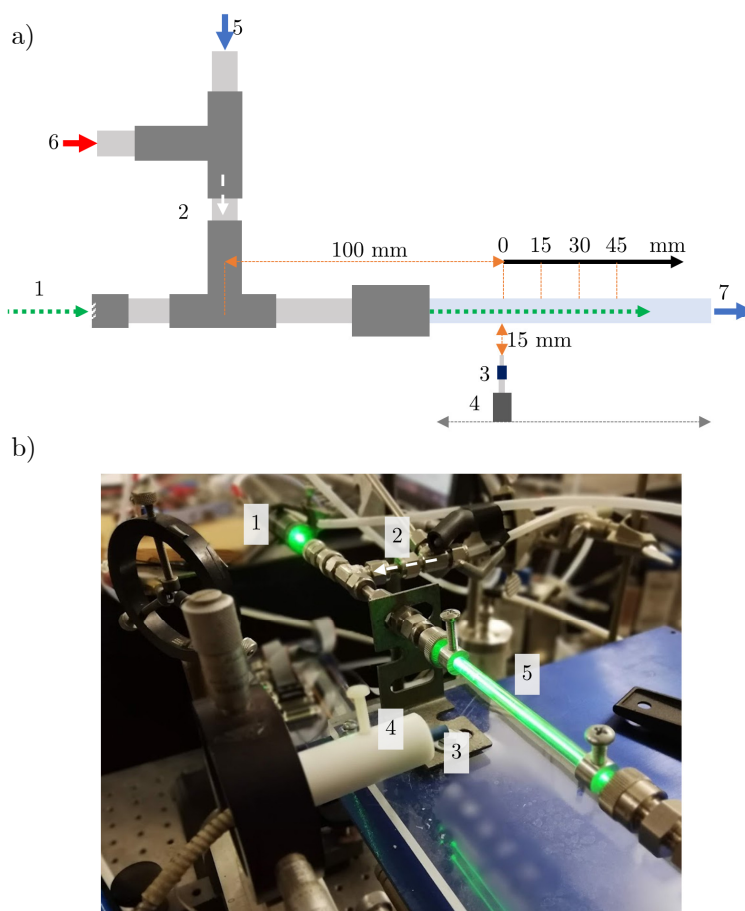


Figure 4.2 Schematic (a) and picture (b) of the plasma reactor and the experimental setup used for system calibration: 1) laser beam; 2) droplet flow; 3) optical probe; 4) holder; 5) droplet flow from the nebulizer; 6) humidified dilution flow; 7) effluent.

## 4.2.2 Evaporation model

The 0-D model used for the simulation of a single droplet evaporation was developed according to a diffusion model based on mass and energy balance well reported in literature [35,36], following the classical evaporation model (CEM) proposed by Spalding [37] and Godsave [38]. This model was further improved following Abramzon-Sirignano approach [39,40], that enabled a better account for advective mass and energy transport. A detailed description of the governing equations and limitations of this model was recently reviewed by Pinheiro et al. [41]. Mass and energy balances can be described according to equations (3-2) and (4-2), respectively:

$$\frac{dm_d}{dt} = -\dot{m}_d \quad (4-1)$$

$$m_d c_{p_l} \frac{dT_d}{dt} = -Q_s \quad (4-2)$$

where  $m_d$  is the droplet mass,  $\dot{m}_d$  is the mass evaporation rate,  $c_{p_l}$  in the specific heat capacity of the liquid droplet,  $T_d$  in the droplet temperature and  $Q_s$  is the net power transferred from the environment which contribute to droplet temperature increase.

Equation (3-2) can be rewritten as a function of droplet diameter ( $D_d$ ), under the hypothesis of a spherical and homogeneous droplet:

$$\frac{dD_d}{dt} = -\frac{2 \dot{m}_d}{\pi \rho_l D_d^2} \quad (4-3)$$

According to the CEM model, widely discussed and applied in different fields of research to study droplet evaporation, based on mass and energy balance evaporation flow rate can be described according to the following equation:

$$\dot{m}_d = \pi D_d D_{vm} \rho_m \text{Sh}_m \ln(1 + B_M) \quad (4-4)$$

where  $D_v$  is the vapour diffusion coefficient,  $\rho$  the density, Sh the Sherwood number and  $B_M$  the Spalding mass transfer number. It's worth mentioning that all the physical properties were calculated in the region of gas-vapour film, considering the presence of both gas and water vapour species. Moreover, as described below, the temperature effect on the value of physical properties was included. The Spalding mass transfer number can be calculated using equation (4-5)

$$B_M = \frac{Y_{vs} - Y_{vg}}{1 - Y_{vs}} \quad (4-5)$$

where  $Y_{vs}$  and  $Y_{vg}$  refer to vapour mass fraction at the droplet-gas interface and in the environment away from the droplet surface, respectively. While  $Y_{vg}$  can be calculated using the known vapour content in the gas phase far away from the droplet surface,  $Y_{vs}$  can be determined applying the classical ideal gas law (Equation (4-6)) under the assumption of liquid-vapour thermodynamic equilibrium at the droplet interface (Raoult's and Clausius-Clapeyron's laws, equation (4-7))

$$Y_{vs} = \frac{\chi_{vs} W_v}{\chi_{vs} W_v + \chi_{gs} W_g} \quad (4-6)$$

$$\chi_{vs}^{eq} = \frac{p_{sat}}{p_g} = \frac{p_{atm}}{p_g} \exp \left[ \frac{L_v M_v}{R} \left( \frac{1}{T_b} - \frac{1}{T_d} \right) \right] \quad (4-7)$$

where  $\chi_{vs}$  and  $\chi_{gs}$  are respectively the surface vapour and gas mass fraction of the liquid gas mixture,  $M_v$  the vapour molar mass fraction and  $W_g$  the gas molar mass.  $L_v$  is the enthalpy of vaporization of the liquid droplet,  $p_g$  the gas pressure,  $R$  the gas constant and  $T_b$  the liquid boiling temperature at standard condition.

Sherwood number (Sh) accounts for the increase of mass transfer due to gas motion and droplet slip velocity through Reynolds (Re) and Schmidt (Sc) numbers. According to Ranz-Marshall empirical correlation [42], Sh number can be evaluated using equation (4-8):

$$Sh_m = 2 + Re_d^{1/2} Sc_m^{1/3} \quad (4-8)$$

where

$$Re_d = \frac{\rho_g D_d |u_g - u_d|}{\mu_m} \quad (4-9)$$

$$Sc_m = \frac{\mu_m}{\rho_m D_{vm}} \quad (4-10)$$

and  $\rho_g$  is the gas density,  $u_g$  and  $u_d$  are the gas and droplet velocity respectively and  $\mu_m$  is the dynamic viscosity calculated for the gas-vapour mix. The mass and energy transfer between gas and droplets at the interface is usually taken into account using a correction factor  $G$ , as discussed by El Wakil et al [43]. Concerning the energy balance, already reported in equation (4-2), it should be mentioned that only part ( $Q_s$ ) of the total energy received from the environment ( $Q_d$ ) contributes to the droplet temperature increase. Indeed, part of the energy contributes to the evaporation of the liquid ( $Q_l$ ), limiting the droplet temperature increase. Following what is reported in [41], the energy balance can be rewritten as a function of gas temperature ( $T_g$ ) as follows:

$$Q_s = Q_d - Q_l = G\pi D_d \text{Nu}_m k_m (T_g - T_d) - L_v \dot{m}_d \quad (4-11)$$

Where Nusselt number (Nu) can be calculated using Prandtl number (Pr) instead of Sc number in equation (4-8), using the specific heat capacity ( $c_{pm}$ ) and the thermal conductivity ( $k_m$ ) of the gas-vapour mixture:

$$\text{Pr}_m = \frac{\mu_m c_{pm}}{k_m} \quad (4-12)$$

The correction factor G can be expressed as a function of a non-dimensional evaporation parameters  $\beta$ .

$$G = \frac{\beta}{e^{\beta} - 1} \quad (4-13)$$

$$\beta = \frac{\dot{m}_d c_{pm}}{2\pi k_m D_d} \quad (4-14)$$

As detailed in several publications by Abramzon and Sirignano [39,40], a more realistic approach can be used taking more precisely into account mass and energy transport. In this perspective, modification to the CEM model was carried out using two different correction factors ( $F_M$  and  $F_T$ ), based on the film theory considering the effect of Stefan's flows at the liquid-gas interface.

$$F_M = (1 + B_M)^{0.7} \frac{\ln(1 + B_M)}{B_M} \quad (4-15)$$

$$F_T = (1 + B_T)^{0.7} \frac{\ln(1 + B_T)}{B_T} \quad (4-16)$$

Where  $B_T$  is the Spalding thermal energy transfer number calculated according to the following equations:

$$B_T = (1 + B_M)^\varphi \quad (4-17)$$

$$\varphi = \left( \frac{c_{pv}}{c_{pg}} \right) \left( \frac{\text{Sh}}{\text{Nu}} \right) \frac{1}{\text{Le}_m} \quad (4-18)$$

$$\text{Le}_m = \frac{k_m}{c_{pm} D_{vm} \rho_m} \quad (4-19)$$

where Le is Lewis number. The corrected value of G,  $\text{Sh}^*$  and  $\text{Nu}^*$  numbers that should be employed in Abramzon-Sirignano model are reported in the following equations:

$$\text{Sh}^* = 2 + \frac{\text{Sh}_0 - 2}{\text{F}_M} \quad (4-20)$$

$$\text{Nu}^* = 2 + \frac{\text{Nu}_0 - 2}{\text{F}_T} \quad (4-21)$$

$$\text{G}^* = \frac{\ln(1 + \text{B}_T)}{\text{B}_T} \quad (4-22)$$

#### 4.2.2.1 Gas, vapour and liquid properties

As mentioned above, the physical properties of the gas, liquid and gas-vapour mixtures and their temperature dependence were calculated using different approaches reported in the published literature.

In the droplet proximity, gas-vapour properties can be described according to the film theory. A brief schematic representation of the droplet-gas environment and the “film region” is reported in Figure 4.3, where  $T$  is the temperature and  $Y$  is the vapour mass fraction. As reported by Hubbard et al. [44] and Yuen and Chen [45], temperature and other physical properties can be approximated using an averaging procedure (Equation (4-23)), where the weighting coefficient ( $\alpha$ ) is 1/3 [41].

$$T_m = T_s + \alpha (T_g - T_s) \quad (4-23)$$

Vapour diffusion coefficient ( $D_{vm}$ ,  $\text{cm}^2/\text{s}$ ) were calculated following the approach reported by Cussler [46] and proposed by Chapman and Enskog:

$$D_{vm} = \frac{1.86 \cdot 10^{-3} \cdot T_m^{\frac{3}{2}} \left( \frac{1}{M_{Ar}} + \frac{1}{M_v} \right)}{p \cdot \sigma_{12} \cdot \Omega} \quad (4-24)$$

where  $p$  is the process pressure in atm,  $\sigma_{12}$  is the collisional diameter in  $\text{Å}$  while  $\Omega$  is a dimensionless factor that can be described according Lennard–Jones 12-6 potential. The temperature dependence of all these factors was taken into account by fitting the data reported in [46] (Table 5.1-2, 5.1-3) for different temperature values.

The fitting of experimental data on liquid enthalpy of vaporization ( $L_v$ ) was used to calculate its dependence with respect to the droplet temperature ( $T_d$ ). While gas density was calculated using the hypothesis of ideal gas, dynamic viscosity ( $\mu_m$ ) and gas thermal conductivity ( $k_m$ ) at the film interface were obtained applying Wilke equation and Chapman-Enskog model [47] to pure gas values obtained from NIST database [48]. Likewise, the specific heat capacity ( $C_{pm}$ ) of gas mixture was calculated through an average weighted on the value of the single gas component obtained from NIST database [49,50].

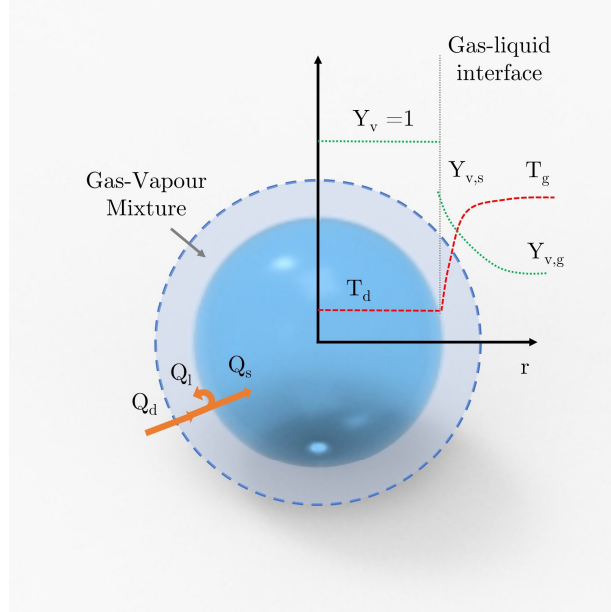


Figure 4.3 Schematic description of gas/liquid properties for an evaporating droplet (modified from [41] and [35])

#### 4.2.2.2 Variation of environment vapour content

As a consequence of the droplet evaporation, the water vapour content of the environment increases during droplet shrinking. Since the model was developed to study droplet evaporation in a close-not infinite environment (because of the plasma source relatively low volume dimension with respect to droplet diameter), increase of vapour content affects the driving force of liquid evaporation (mass concentration gradients) and should be considered. In this perspective, droplet concentration can be obtained using scanning mobility particle sizer (SMPS) data under the hypothesis of one droplet-one particle conversion, as widely discussed in literature [34,51,52]. Under the assumption that droplets are equally distributed in the space, each droplet can be considered at the centre of a control volume which dimension is the reciprocal of particle concentration. Following this hypothesis, the hypothetical control volume in which each droplet is contained is much larger than droplet volume: for a droplet density of  $10^5 \text{ cm}^{-3}$ , each droplet is enclosed in a control volume of  $10^6 \mu\text{m}^3$ . If the particle size distribution is small enough (1-5  $\mu\text{m}$  or below), the relative contribution of the droplet volume to the available gas volume can be neglected (for a 5  $\mu\text{m}$  droplet the ration between liquid volume and control volume is 0.01 %). Under the hypothesis, the gas mass for each volume unit ( $\text{mass}_{Ar}$ ) can be calculated using the gas ideal

law. For each time step of the simulation ( $\Delta t$ ), water content ( $\text{ppm}_i$ ) was updated considering the initial vapour concentration ( $\text{ppm}_0$ ) and the mass evaporated from the droplet ( $m_d$ ), as reported in equation (4-25).

$$\text{ppm}_1 = \frac{(\text{ppm}_0 \cdot \text{mass}_{Ar} + m_d \cdot 10^6 \cdot \Delta t)}{\text{mass}_{Ar}} \text{ for } i=1 \dots n \quad (4-25)$$

#### 4.2.2.3 Assumptions and limitation of the simulative model

It should be remembered that the model here proposed is characterized by some assumption and limitations, that, according to the literature, can marginally affect the obtained results. However, since the output of the model will be compared to experimental results, it's worth highlighting the main hypotheses on which the model is based.

Firstly, gas temperature during evaporation and during droplet transport inside the control volume (e.g. reactor) was assumed constant. With respect to the experimental results, this assumption is valid if the heating up of the gas is fast inside the reactor and the droplet temperature reaches a constant value in a period which order of magnitude is lower than the evaporation time. This way, possible effect of localized streamers and inhomogeneities in the temperature field are not taken into account, Gas temperature was estimated by means of different techniques described in the previous paragraphs.

According to what is reported in literature, usually heat transfer resistance inside an evaporating droplet can be assumed to be negligible. To support this point, we compared the heat transfer resistance inside and outside the evaporating droplet using Biot number (Bi). Bi is a dimensionless number described as the ratio between the heat transfer inside the droplet and at the droplet surface. If  $\text{Bi} < 1$ , then the internal body thermal resistance can be neglected and the temperature field considered uniform. Bi can be defined according equation (4-26) and expressed as a function of  $\text{Nu}_m$ , already introduced above.

$$\text{Bi} = \frac{L_0 \cdot h}{k_l} = \frac{\text{Nu}_m \cdot k_m}{k_l} \quad (4-26)$$

where  $L_0$  is the characteristic length ( $r/3$  for a sphere),  $h$  is the film heat transfer coefficient ( $\text{W}/\text{m}^2\text{K}$ ) and  $k_l$  is the thermal conductivity of the droplet. Even if all terms are temperature dependent, the value of Bi number is slightly affected by small thermal gradients. Indeed, at 293 K the Bi number for the tested condition is 0.066, significantly lower than 1. This result, in line with what has been already reported in literature [43], outlines that the temperature gradient is much higher in the film region than in the droplet bulk, confirming that we can describe the droplet as a solid sphere with infinite thermal conductance.

## 4.3 Results & Discussion

### 4.3.1 Experimental setup characterization and calibration

#### 4.3.1.1 Characterization of the plasma reactor

Electrical characterization of the plasma discharge was carried out with the aim of monitoring the power supplied by the HV generator. The energy delivered for each period was obtained through the measurement of the area of Lissajous figures (Figure 4.4a), pointing out a mean power of 7 W supplied by the generator to the reactor (Table 4.1). According to Pipa and Brandenburg [32], the charge-voltage plot can also be used to obtain information about the equivalent circuit which describes a DBD plasma reactor. Considering this, the slope of the curve during the *plasma on* and *plasma off* phases (Figure 4.4a) was measured and used as a good approximation of dielectric and gas capacitances (Table 4.1). Afterwards, the equivalent circuit can be solved with the aim of obtaining the current and the voltage flowing and applied to the gas gap, respectively. An analysis of the voltage-current curves applied to the DBD plasma reactor outlined 90° of current phase shift with respect to the ones calculated at the gas gap. Conversely, the absence of delay in the current waveform through the gas gap with respect to the voltage gap (Figure 4.4b) supports the description of the discharge as a resistance, enabling further considerations. Following the approach proposed by Sarani [53] and Ge [54], electron density ( $N_e$ ,  $\text{cm}^{-3}$ ) can be assessed through the measurement of discharge current ( $J$ ,  $\text{A cm}^{-2}$ ) and electric field ( $V \text{ cm}^{-1}$ ). The relationship can be re-written relating electron density to gas impedance ( $Z$ ,  $\Omega \text{ cm}^2$ ) and the approach can be easily applied once the equivalent circuit is solved. Equation (4-27) reports the formula used for electron density, as a function of the discharge gap ( $d$ ), the Faraday constant ( $e$ ) and the electron mobility ( $\mu_e$ , [55]). Based on a mean plasma impedance of  $1.09 \text{ M}\Omega$ , our calculation highlighted an electron density of  $3 \cdot 10^{11} \text{ cm}^{-3}$ , in line with what was previously reported for this type of reactor and discharges by Bruggeman [30].

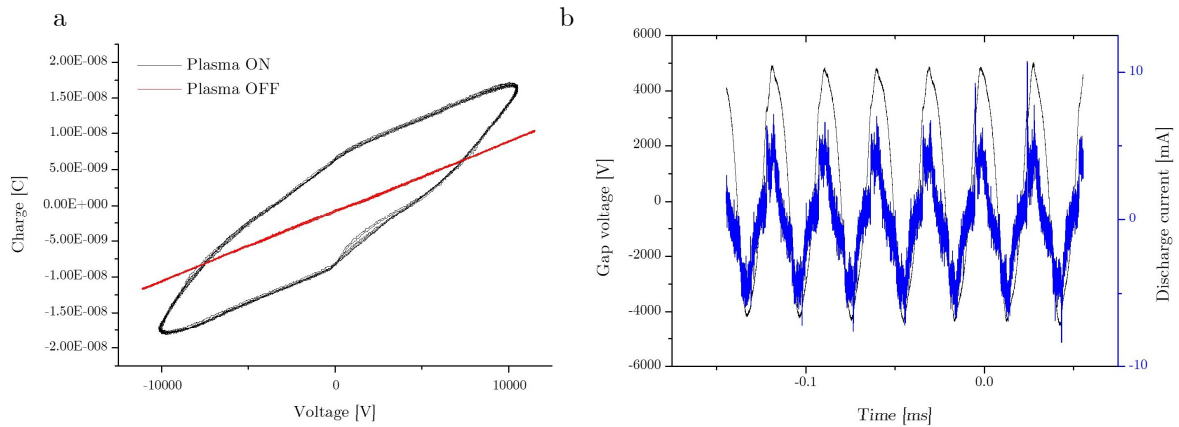


Figure 4.4 Lissajous figure (a) and voltage-current waveform calculated at the discharge gap (b).

$$N_e = \frac{J}{e \cdot \mu_e \cdot E} = \frac{d}{e \cdot \mu_e \cdot Z} \quad (4-27)$$

Power [W]	$7.2 \pm 0.2$
$C_{\text{die}}$ [pF]	2.46
$C_{\text{gap}}$ [pF]	0.73
$Z$ [ $\Omega$ ]	$1.09 \cdot 10^6$
$\mu_e$ [ $\text{cm}^2 \text{V}^{-1} \text{s}^{-1}$ ]	434.21
$N_e$ [ $\text{cm}^{-3}$ ]	$3.14 \cdot 10^{11}$

Table 4.1 Electrical characteristics of the plasma reactor and of the gas discharge.

The estimation of gas discharge temperature for non-equilibrium plasma is usually performed through optical emission spectroscopy and the analysis of molecular rotational states of OH and  $\text{N}_2$  [56]. Since the impurities in our reactor were limited and the introduction of  $\text{N}_2$  dilution gas has been shown to affect the accuracy of gas temperature measurement [53], we carried out the investigation of OH rotational states. Unfortunately, as already reported by Bruggeman [57,58], the presence of a high amount of water (above 1000 ppm) prevented the thermalization of the rotational population, affecting the measurement of gas temperature through Boltzmann plot techniques. As shown by Sarani [53] in fact, this evidence limits the possibility to use rotational OH temperature as a good approximation of gas temperature. In our experiments, the overpopulation of rotational levels hindered the possibility to obtain reliable values. It's worth mentioning that, even if advantageous with the aim of improve the simulation taking into account temperature gradient, a precise knowledge of the local temperature field inside the reactor is hampered because of several

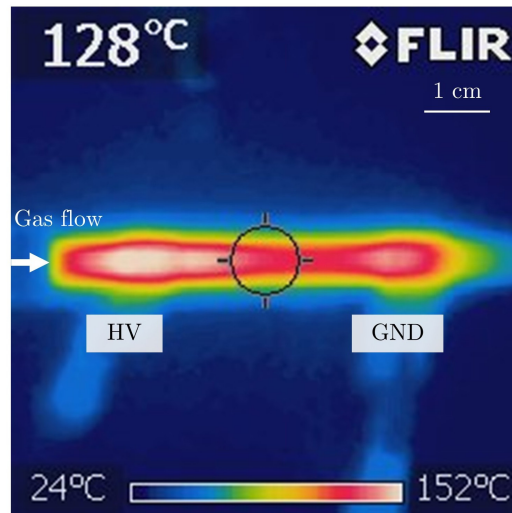


Figure 4.5 Temperature distribution of the external wall of the plasma reactor.

phenomena. While the presence of streamers, in particular localized near the quartz wall because of hugging-mode discharge [59,60], can induced a non-uniform temperature field, it's well known that the presence of evaporating aerosol can be accounted for a local decrease of gas temperature, further affecting temperature distribution. For this reason, the temperature of the reactor was estimated using an IR camera and estimating through a thermodynamic approach the wall temperature inside the reactor.

After the measurement of the reactor temperature carried out by means of an IR camera (Figure 4.5), the value of the temperature of the internal wall was estimated considering the thermal conductivity of quartz ( $1.4 \text{ W m}^{-1} \text{ K}^{-1}$ ) and the thickness of the wall (1 mm). The temperature difference between the internal and the external wall was calculated in the range of  $\sim 10 \text{ K}$  due to the limited power (7 W) supplied by the HV generator.

Therefore, the results suggested an internal wall temperature in the range of 410-430 K, depending on the position in the reactor.

#### 4.3.1.2 Characterization of droplet flow and scattering calibration procedure

With the aim of exploring the evaporation of water droplets inside a plasma reactor, an extensive characterization of aerosol flow and plasma discharge was carried out.

Laser diffraction was employed to characterize the size distribution at the exit of the Venturi nebulizer (inlet of the plasma reactor) for different flow rates. According to the Fraunhofer approximation, the analysis of scattering patterns produced by the interaction of a laser beam and an aerosol flow enabled the possibility to obtain information on volumetric droplet size distribution. Depending on the application, number or surface weighted droplet distribution can be obtained following the approach proposed by Hinds [34] and reported in the Malvern guideline [61]. Under the assumption of spherical droplets, volume-based distributions were then converted to number and surface weighted ones. Results for 1300 scem of Ar passing through the nebulizer are reported in Figure 4.6 and

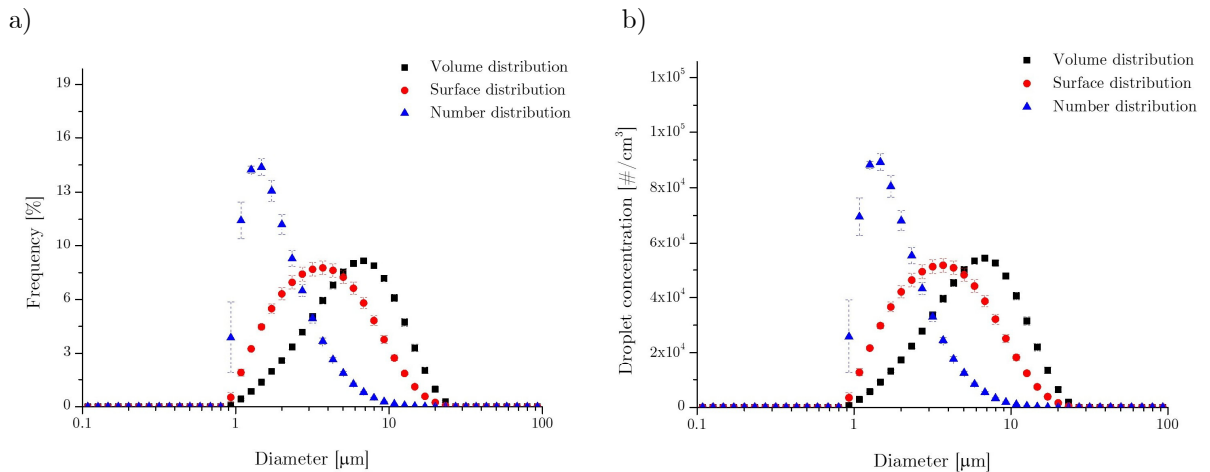


Figure 4.6 Frequency (a) and concentration(b) distributions of aerosol droplet.

outlined a mean particle distribution of 1.4  $\mu\text{m}$ , 3.7  $\mu\text{m}$  and 6.8  $\mu\text{m}$  respectively for number, surface and volume distributions.

When the Ar mass flow rate passing through the nebulizer was increased or reduced, a shift to lower or higher mean droplet diameter is respectively found (Figure 4.6 and Figure 4.7). The results, in line with what reported by Lefebvre [35], suggested that higher flow rate increased the gas speed through the nozzle and led to the formation of smaller droplets. Conversely, lower flow rates were characterized by lower break down energy, contributing to the increase of mean droplet size. For this reason, gas flow rate through the nebulizer was kept constant at 1300 sccm for all the experiments, thus preserving the droplet distribution used as a fixed parameter for the following experiments.

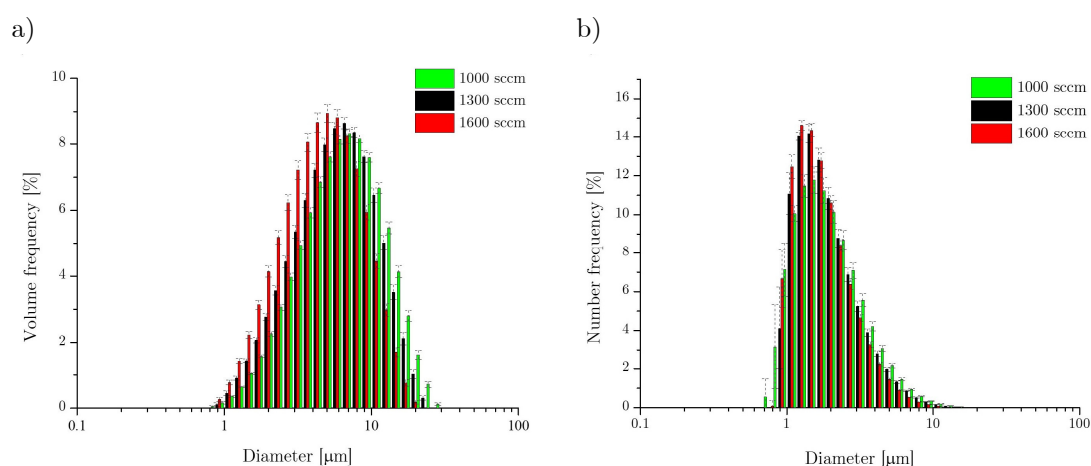


Figure 4.7 Volume (a) and number(b) weighted droplet size distributions for different flow rates.

Beside size distribution, droplet concentration was investigated and used as an input data for the following experiments. According to Stabile et al. [51], our hypothesis is based on the formation of a single crystal particle from an evaporating droplet containing a salt solution. Therefore, under the hypothesis of one droplet – one particle conversion, the droplet concentration should be assessed from the particle concentration. To confirm the accuracy of the hypothesis, we compared droplet size distribution obtained from laser diffraction with salt residual size distribution measured with SMPS, calculating the expected particle size distribution that could have been obtained from the evaporating aerosol with known distribution and salt concentration (further information on the used approach can be found in Chapter 4). Results, reported in Figure 4.8, showed a good agreement between experimental and expected results in terms of particle size.

Finally, absolute droplet concentration, calculated integrating the concentration measured using SMPS for each bin and corrected by the  $\log D_p$  factor (as suggested by TSI guidelines [62]), was used to obtain the droplet concentration as a function of size (Figure 4.6) that was found to be  $6 \cdot 10^5 \text{ cm}^{-3}$ .

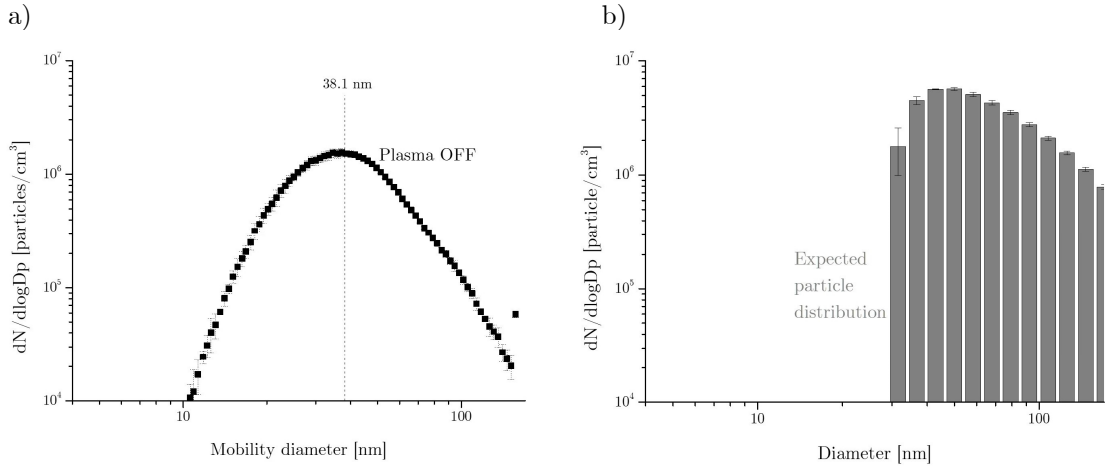


Figure 4.8 a) Mean particle distribution obtained from SMSP measurements; b) expected particle distribution calculated from laser diffraction measurement under the hypothesis of complete droplet evaporation and one droplet – one particle conversion.

While size and concentration measurements of aerosols expanding in ambient air are widely applied both in combustion [63] and medical studies [64], recently *in-situ* measurement of droplet concentration has received attention with the aim of investigating localized phenomena inside diesel combustors [35,65]. In this framework, the measurement of droplet induced light extinction is a well-established and calibration-free method, employed for the quantitative analysis of particle concentration. As discussed by Bachalo et al. [66] in fact, laser light travelling in a spray of suspended droplets experiences intensity attenuation in the forward direction that can be described according to Lambert-Beer law [67,68]. Extinction cross sections, calculated as a function of droplet size, can be directly employed for particle concentration measurement, offering a fast and on-line characterization method. Where optical accesses are limited because of geometrical limitation of the device, light scattering method has been proposed as an alternative for aerosol characterization [65]. Following these established approaches, we developed an experimental design with the aim of exploring the possibility to track a particle flow inside a plasma discharge.

Once obtained information on droplet flow properties, the aerosol nebulizer was coupled with the plasma reactor already described above. To gain insights in droplet concentration decrease due to droplet evaporation inside the plasma reactor, laser scattering intensity was measured with an optical probe located at  $90^\circ$  with respect to the aerosol flow. The experimental setup and approach was developed following what has been proposed in the combustion engine field, where *in-situ* droplet characterization is usually performed using Mie scattering [65,68,69]. Interestingly, the possibility to track a droplet flow in a thermal

plasma reactor has been exploited only by Jorabchi et al. [70] and, to the best of our knowledge, our work is the first attempt to quantitative measure droplet concentration inside a non-equilibrium plasma discharge.

Results of preliminary experiments aimed at supporting the specific relationship between the droplet presence and the characteristic peak produced by laser-droplet interaction are reported below (Figure 4.9). The laser emission peak centred at 531 nm is reported for different operating conditions. In particular, the data corroborated that the scattering signal can be ascribed to the presence of the droplet flow. Furthermore, the reduction of the droplet concentration due to plasma induced evaporation is highlighted from the lower emission intensity of the collected spectrum (b) with respect to the plasma off experiment (a).

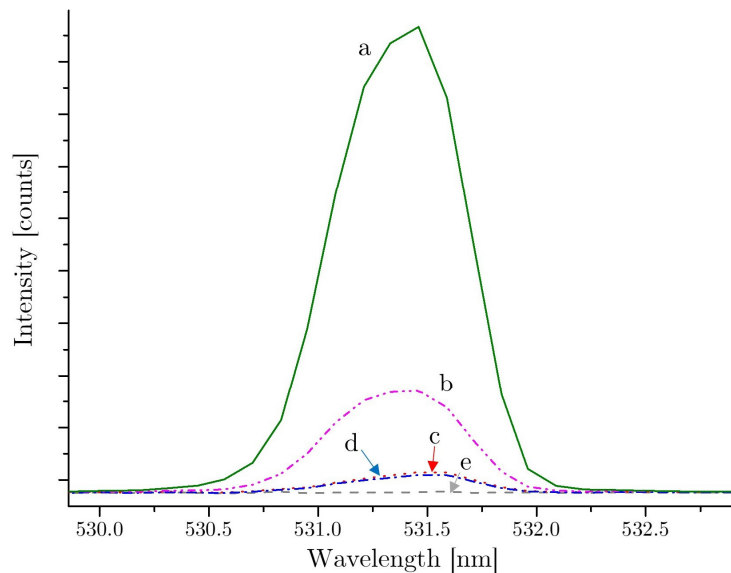


Figure 4.9 Emission peak due to laser scattering for different operating conditions:  
 - with droplet flow: a) Plasma OFF; b) Plasma ON;  
 - without droplet flow: c) Plasma OFF; b) Plasma ON  
 -e) Background (Plasma ON, without droplet).

The calibration of the measurement system was carried out through the analysis of the scattering intensity for five different droplet concentrations in four different position of the reactor (Table 4.2). According to the theory, two main contributions can be accounted for the reduction of scattering intensity inside the reactor during the calibration procedure: firstly, since the intensity of scattering signal is proportional to the droplet surface it was expected that a decrease in droplet concentration would have led to a reduction in the scattering intensity (for a given position in the reactor); secondly, keeping constant the concentration of the droplet inside the reactor and under the assumption of a proportional correlation between the incident and scattered light, one would expect a reduction of the incident laser intensity for following sections of the reactor [66,68] due to light absorption and a consequent decrease in the scattering intensity. A brief schematic that describes the

two effects is reported in Figure 4.10. Since the dilution of the droplet flow was performed by means of a humidified Ar flow, we can assume negligible the effect of change in droplet size (and surface area) when droplet concentration was changed.

For the same droplet concentration, the light intensity was found to decrease as a function of the position in the reactor Figure 4.11. Focusing the attention of the light extinction through the reactor for the same concentration, we found that experimental data had an exponential trend. This result corroborated that, for each droplet concentration, the 90° scattering light decrease along the reactor can be described following the Lambert-Beer (Equation (3-1)) law and therefore the extinction coefficient ( $\sigma$ ) can be calculated fitting the collected experimental data.

$$I(x) = I_0 \cdot \exp(-\sigma \cdot x) \quad (4-28)$$

Carrier flow rate [sccm]	1300	1300	1300	1300	1300
Dilution flow rate [sccm]	0	904	1358	1811	2265
Dilution ratio [%]	100	59	49	42	36
Droplet concentration [# / cm <sup>3</sup> ]	6.29E+05	3.71E+05	3.07E+05	2.63E+05	2.29E+05
$\sigma$ , extinction coefficient [cm <sup>-1</sup> ]	0.124 ± 0.006	0.096 ± 0.003	0.083 ± 0.006	0.061 ± 0.006	0.057 ± 0.006

Table 4.2 Operating parameters used for system calibration and scattering extinction coefficient obtained from data fitting.

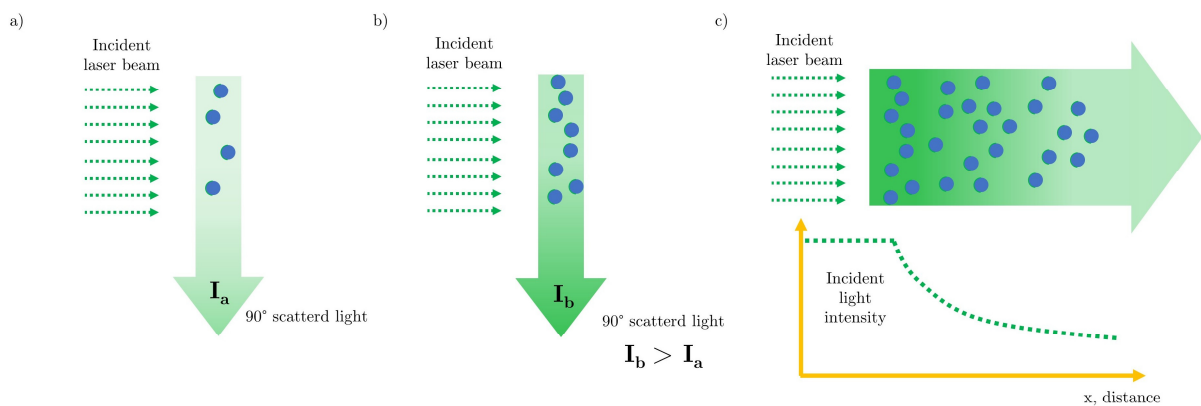


Figure 4.10 Effect of droplet concentration of scattered light intensity for lower (a) and higher (b) droplet number; c) qualitative description of incident laser decay through the reactor due to droplet absorption.

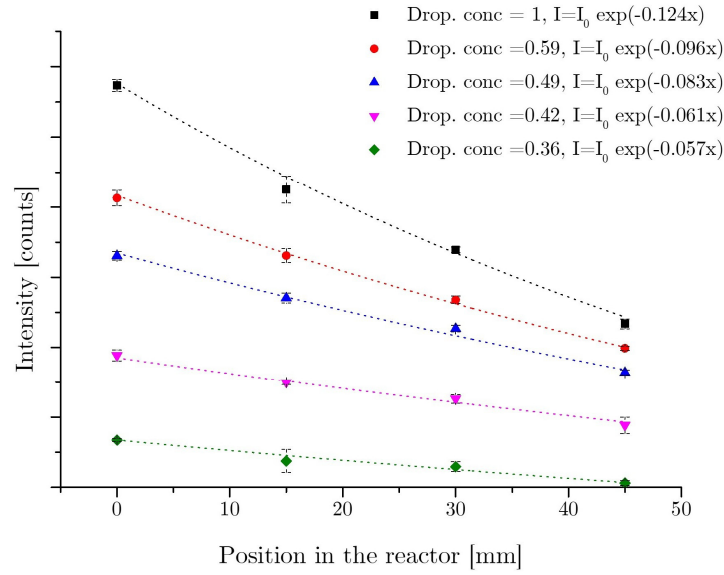


Figure 4.11 Dependence of scattering intensity with respect to droplet concentration and probe position along the reactor.

The results were then fitted using an exponential law and extinction coefficient and are reported in Table 4.2. A comparison among the extinction coefficients calculated for different droplet concentrations showed that the reduction in the intensity of forwarded light was lower when the droplet concentration was decreased, confirming the results already discussed by Sulaiman et al. [68]. The decrease of extinction coefficients as a function of dilution rate is related to a reduced droplet concentration: the lower number of droplets in the forward direction in fact is responsible for minor absorbance and, therefore, of lower light extinction along the reactor. This result is in agreement with the results discussed by Sulaiman and Bachalo [66,68], where the extinction coefficients were calculated using the following Equation:

$$\sigma = \sigma_e \cdot N_d \quad (4-29)$$

where  $N_d$  is the droplet density ( $\text{cm}^{-3}$ ) and  $\sigma_e$  is the extinction ( $\text{cm}^{-2}$ ). This latter value can be calculated according to Equation (4-30) as a function of mean extinction coefficient ( $\bar{Q}_e$ , assumed to be 2 [66]) and the square value of droplet diameter ( $D_{2,0}$ ).

$$\sigma_e = \frac{\pi}{4} \bar{Q}_e D_{2,0}^2 \quad (4-30)$$

In Figure 4.12, the semi-empirical extinction coefficients calculated according to Equation (4-29) are compared to the measured data obtained from the experimental curve fitting. The good agreement among the data supported the validity of the proposed approach and reliability of the experimental setup.

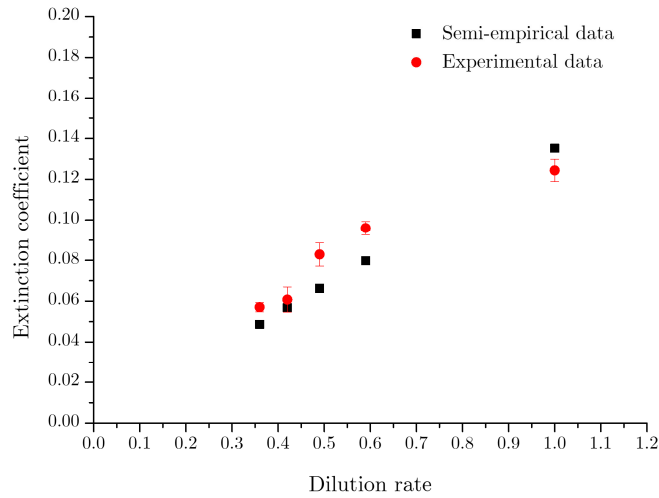


Figure 4.12 Comparison of semi-empirical and measured extinction coefficient as a function of dilution rate.

With the aim of system calibration, the evaluation of extinction coefficients offered the possibility to investigate the relationship between scattering intensity and droplet concentration for a fixed position along the reactor. It should be mentioned that while comparing the effect of different concentrations inside the reactor, the effect of droplet concentration on the intensity of the incident light should also be considered. The raw data obtained from intensity measurement for different concentrations were then corrected using the extinction factors and the distance travelled by the laser beam inside the reactor (between the aerosol inlet and the analysis point), according to equation (4-31). Afterwards, experimental data collected for different concentrations were normalized with respect to the pristine concentration and plotted against the dilution ratio, as reported in Figure 4.13. The results outlined a good agreement between dilution ratio and scattering intensity, confirming

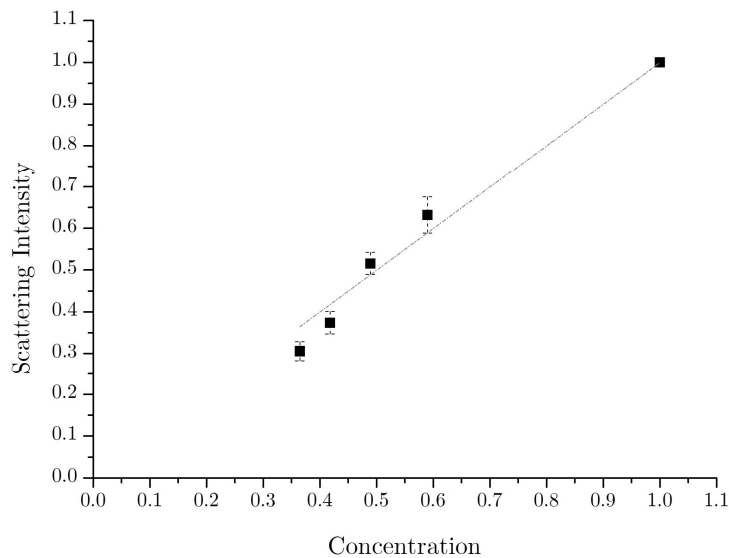


Figure 4.13 Relationship between scattering intensity and droplet concentration for a fixed position in the reactor.

the possibility to use a linear correlation to evaluate aerosol concentration inside the reactor by measuring the laser scattering intensity.

$$I^*(0)=I(x) \cdot \exp(-\sigma \cdot x) , \text{ where } x=10 \text{ cm} \quad (4-31)$$

Once demonstrated the possibility to correlated laser scattering intensity and droplet concentration, the investigation of droplet evaporation inside the plasma reactor was carried out. The reference position ( $x=0$ ) was located at the upper edge of the HV electrode, according to the schematic reported in Figure 4.14a. Raw data collected during the *plasma on* and *plasma off* experiment were then plotted and compared to the background intensity (Figure 4.14b). The decrease of scattering intensity during the plasma on phase can be ascribed to a gradual evaporation of the droplet through the reactor due to plasma-droplet interactions. The intensity decrease followed an exponential law, suggesting that droplet concentration reduction was faster during the first instants of plasma-aerosol contact. This evidence supported the hypothesis of a fast evaporation of smaller droplets in the first sections of the reactor, followed by a more stable reactor zone where evaporation of bigger droplets took place. Based on the linear relationship between droplet concentration and scattering intensity, the percentage reduction in droplet concentration was evaluated through normalization of acquired data with respect to the *plasma off* intensity. Absolute droplet concentration was then evaluated using the total particle concentration obtained from SMPS measurement described above and plotted for all the sections of the plasma reactor.

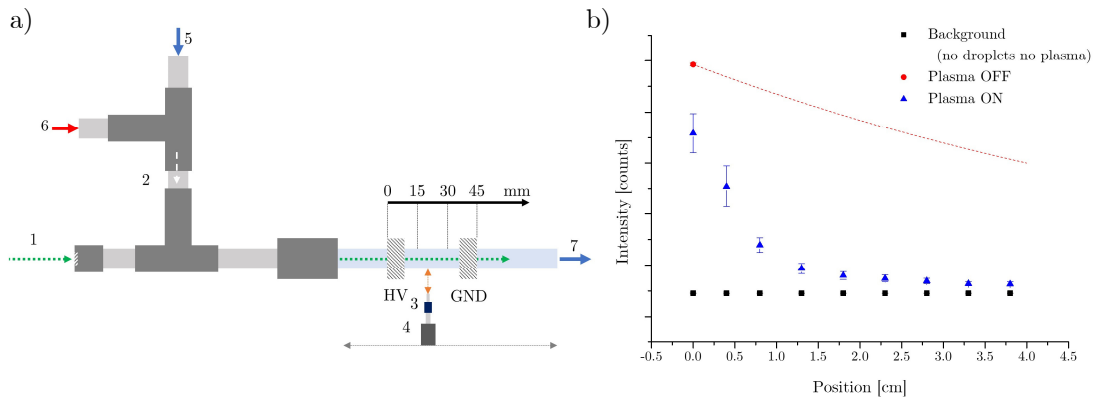


Figure 4.14 a) Schematic representation of the plasma reactor: 1) laser beam; 2) droplet flow; 3) optical probe; 4) holder; 5) droplet flow from the nebulizer; 6) humidified dilution flow; 7) effluent; b) Scattered light intensity in different section of the reactor.

### 4.3.2 Simulation of droplet evaporation

With the aim of investigating the role of thermal effect of droplet evaporation inside a plasma discharge, a 0D simulation script was developed in MatLab<sup>®</sup> environment. Validation of the simulative model was completed comparing the obtained results with the experimental data reported by Ranz and Marshall [42]. The hypotheses used for model

validation apply also for the results presented in the following paragraphs, where input parameters of the simulation were changed. Afterwards the model was used to simulate water droplet evaporation in a closed environment filled with Ar gas. While the dimension of the control volume was evaluated taking into account the droplet concentration in the aerosol flow, droplet size and gas temperature were changed with the aim of investigating their effect on evaporation time (Table 4.3). The initial value of water vapour content was kept constant for all the simulation. Conversely, due to droplet evaporation, vapour content of the environment was updated for each simulative step, considering the amount of water evaporated during the previous one. The results for different droplet diameters and gas temperatures are reported in Table 4.3 and Figure 4.15.

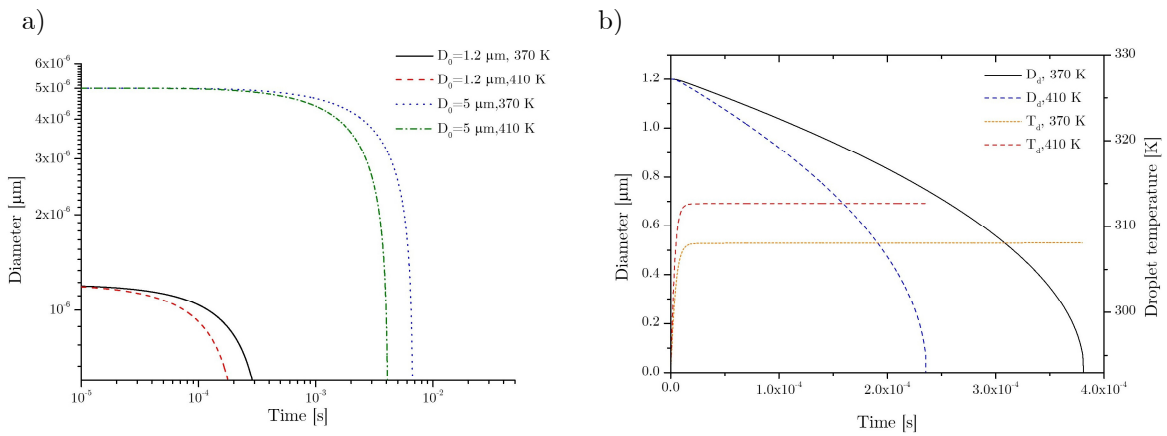


Figure 4.15 a) Temporal variation of droplet diameter as a function of gas temperature and initial size; b) Droplet diameter and temperature during evaporation process as a function of gas temperature.

Input parameters/Condition	A	B	C	D
Droplet size [μm]	1.2	5	1.2	5
Droplet temperature [K]	293	293	293	293
Gas humidity [ppm <sub>v</sub> ]	10657	10657	10657	10657
Gas temperature [K]	370	370	410	410
Evaporation time [s]	3.81·10 <sup>-4</sup>	6.8·10 <sup>-3</sup>	2.36·10 <sup>-4</sup>	4.1·10 <sup>-3</sup>
Evaporation constant [m <sup>2</sup> /s]	3.8·10 <sup>-9</sup>	3.8·10 <sup>-9</sup>	6.2·10 <sup>-9</sup>	6.2·10 <sup>-9</sup>

Table 4.3 Input data and simulative results for different gas temperatures and droplet sizes.

Inside a hot environment, where the water content was lower with respect to the one found at gas-droplet interface, the droplet underwent evaporation following the classical D-square law (Equation (4-32)). The imbalance in energy equilibrium between evaporation and heating-up brought to an increase of droplet temperature, which reached a steady state after a few microseconds. While, bigger droplets were characterized by higher evaporation time, lower gas temperature was found to decrease droplet evaporation rate. Interestingly, we found that the evaporation constant (c) was not a function of droplet size, but only depended

on gas temperature (and eventually on water vapour content). This result, in agreement with what previously reported in literature [34], was also corroborated by the parabolic relationship between the evaporation time and droplet initial diameter for different gas temperatures (Figure 4.16).

$$D^2(t) = D^2(0) - c \cdot t \tag{4-32}$$

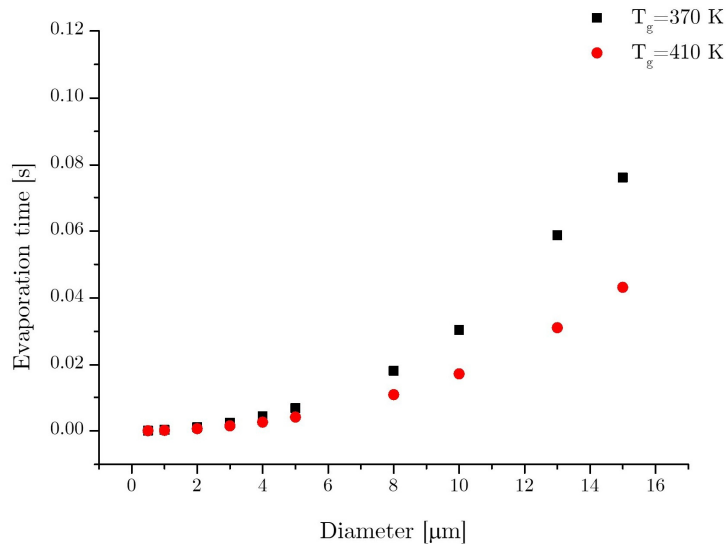


Figure 4.16 Evaporation time for different droplet sizes and gas temperatures.

The developed model was then used to simulate the evaporation of the distribution of water droplets measured at the exit of the nebulizer. For each droplet size, the evaporation

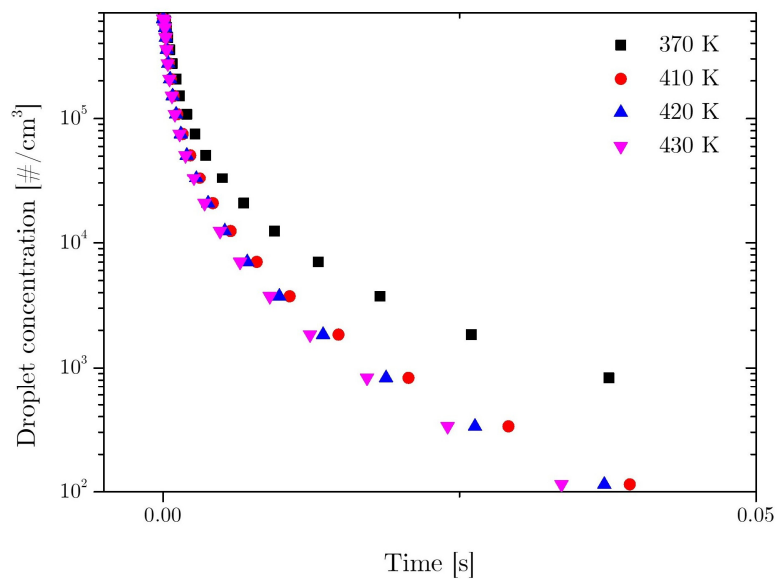


Figure 4.17 Simulation of droplet distribution evaporation for different gas temperature.

time was calculated as a function of gas temperature, enabling the study of droplet number decrease as a function of time. The results, plotted in Figure 4.17, describe the fast reduction of droplet concentration during the first instants and the first zone inside the reactor, followed by a reduction in the evaporation rate. This behaviour can be explained taking into account the D-square relationship between the evaporation time and droplet diameter, as already discussed above. It was also demonstrated that the contribution of gas temperature to the evaporation rate was significant only for bigger droplets, only partially affecting the slope of droplet concentration during the first milliseconds.

### 4.3.3 Comparison of experimental and simulation results

To gain a deeper understanding on the droplet evaporation mechanism, experimental results were compared to the data obtained using the simulative model. It is worth bearing in mind that scattering intensity is proportional to the surface area rather than droplet concentration. Regarding droplet evaporation, size reduction is controlled by surface reactions leading to a linear relationship between the square diameter and the evaporation time (D-square law). This evidence highlights that with regards to our experiments, along the reactor the surface area available for Mie scattering decreased both because of droplet number decrease (complete evaporation) and for the particle shrinking (partial evaporation). When comparing experimental results and simulative model it's therefore important to take into account both contributions. For this reason, the contribution to the whole aerosol surface of all the droplets as a function of their size was corrected using the evaporation constant evaluated accordingly to D-square law (see Table 4.4 and equation (4-33) in the Appendix).

The results of the simulation obtained as a function of the time step for different gas temperatures (Figure 4.17) were then converted to space-dependent function, taking into account the section of the reactor ( $4\pi \text{ mm}^2$ ), the gas flow rate (1300 sccm Ar) and temperature. The comparison of laser scattering data (Figure 4.18) and results derived from simulation outlined a good agreement both in terms of droplet concentration and evaporation rate. In particular, experimental data were consistent with the simulation performed in the range of 410-430 K supporting the possibility to describe plasma induced evaporation according to a standard aerosol model, as brought up by Bruggeman [30] and Iqbal [71]. Even if carried out with different experimental setup (He RF discharge), droplet size and measuring techniques (fast framing microscopic imaging), the agreement of our results with the study carried out by Bruggeman corroborated the hypothesis that water vapour diffusion and heat transfer can be accounted as the major contributions to droplet evaporation inside gas discharges. Interestingly, the models fitted properly different droplet size, validating once more our hypothesis. Likewise, measurement of droplet size carried out by Iqbal at the outlet of a corona reactor matched the results of 3D modelling based on aerosol energy and mass balance, where only thermal heating was taken into account. All these findings disagreed with what was proposed by Maguire [18], who found evaporation constant of  $5 \cdot 10^{-7} \text{ m}^2/\text{s}$  for

droplet aerosol exposed to a cold ( $\sim 350\text{-}400\text{ K}$ ) plasma discharge. The value found by the author, definitely higher with respect to our and Bruggeman's ( $c=2\cdot 10^{-8}\text{ m}^2/\text{s}$ ) results, was found in line with evaporation rate reported for inductively coupled RF thermal plasma torch modelling [72] and experiments [73,74] where the gas temperature was significantly higher (3000 K). Because of the limited discharge temperature, the significative decrease in droplet size was addressed to unexplored phenomena taking place in the plasma discharge (e.g. Coulombic fission, ion impact). Despite the limited resolution ( $1.73\text{ }\mu\text{m}$  [19]) of the experimental setup could have affected the measurement of droplet size reduction in Maguire's work, we can speculate that the combination of gas mixtures, electron energy/density and droplet distribution could have influenced the evaporation rate. In this perspective, the findings presented so far highlights the need of comprehensive approach to fully addressed the effect of parameters on droplet evaporation: in order to corroborate the achieved results.

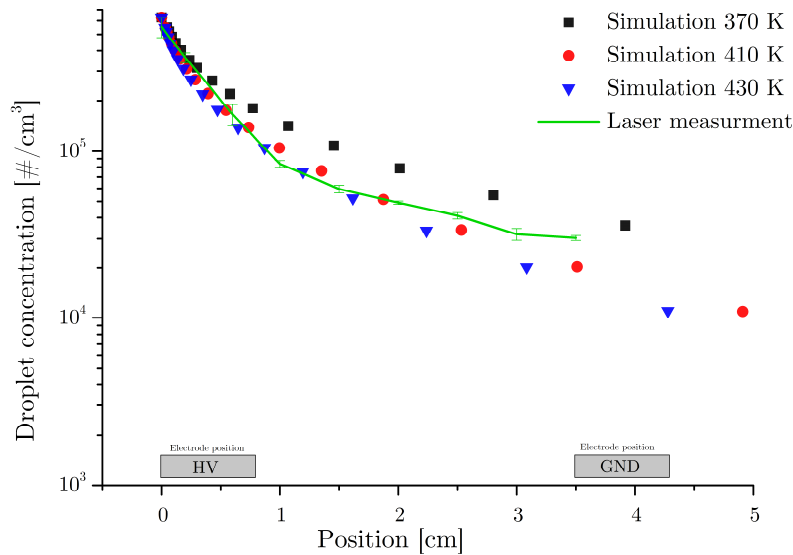


Figure 4.18 Comparison among simulative and experimental results for different gas temperature.

Even if a good correlation between simulation results and experimental data was found, a deeper investigation on the effect of plasma and droplet characteristics should be carried out coupling in-situ and ex-situ monitoring techniques discussed above. In particular, the unknown effects of droplets on streamer propagation and of streamers impingement on droplet surface (e.g. Joule heating, charge deposition) should be investigated with the aim of gaining a deeper control of plasma-droplet interaction.

## 4.4 Conclusions

The design and development of an experimental setup aimed at *in-situ* monitoring of droplet concentration inside a plasma discharge gave us the opportunity to study liquid evaporation along the reactor, also comparing the achieved results with simulative model results. To the best of our knowledge, this was the first attempt to gain insight on the interaction between a non-equilibrium plasma and an aerosol flow by means of a non-invasive and inexpensive diagnostic technique able to quantitatively track particle concentration inside the discharge. In this framework a water aerosol flow was introduced in a DBD flow-through reactor coupled with a laser beam that was aligned to the axis of the plasma device. Exploiting Mie scattering induced by droplet-laser beam interaction, the system was calibrated for different droplet concentration and finally droplet decay in the plasma discharge was monitored. The decrease of droplet concentration when the plasma was turned on was found to be a decreasing function of distance travelled inside the reactor, suggesting a relationship between plasma exposure and evaporation rate. With the aim of addressing the main contribution to droplet evaporation, the results of experimental tests were compared to a 0D model developed following the standard evaporative model applied for combustion studies. The simulative results fitted with a good approximation the exponential decay of droplet concentration measured exploiting laser scattering. While in line with part of the previously published results, the developed experimental approach can be used to further address the specific contributions of plasma reactive species and characteristics. The possibility to couple laser scattering measurement, with evaporation modelling, plasma characterization and droplet size control will be a great achievement for future studies, enabling the tuning of plasma-aerosol treatment with a view to industrial applications.

## 4.5 References

- [1] Gubkin J 1887 Electrolytische Metallabscheidung an der freien Oberfläche einer Salzlösung *Ann. Phys.* **268** 114–5
- [2] Lin L and Wang Q 2015 Microplasma: A New Generation of Technology for Functional Nanomaterial Synthesis *Plasma Chem. Plasma Process.* **35** 925–62
- [3] Bekeschus S, Favia P, Robert E and von Woedtke T 2019 White paper on plasma for medicine and hygiene: Future in plasma health sciences *Plasma Process. Polym.* **16** 1–12
- [4] Parvulescu V I, Magureanu M and Lukes P 2012 *Plasma Chemistry and Catalysis in Gases and Liquids*
- [5] Gherardi M, Puač N and Shiratani M 2018 Special issue: Plasma and agriculture *Plasma Process. Polym.* **15** 1877002
- [6] Bruggeman P J, Kushner M J, Locke B R, Gardeniers J G E, Graham W G, Graves D B, Hofman-Caris R C H M, Maric D, Reid J P, Ceriani E, Rivas D F, Foster J E, Garrick S C, Gorbanev Y, Hamaguchi S, Iza F, Jablonowski H, Klimova E, Kolb J, Krcma F, Lukes P, Machala Z, Marinov I, Mariotti D, Thagard S M, Minakata D, Neyts E C, Pawlat J, Petrovic Z L, Pflieger R, Reuter S, Schram D C, Schröter S, Shiraiwa M, Tarabová B, Tsai P A, Verlet J R R, von Woedtke T, Wilson K R, Yasui K and Zvereva G 2016 Plasma-liquid interactions: a review and roadmap *Plasma Sources Sci. Technol.* **25** 53002
- [7] Bruggeman P, Verreycken T, Gonzalez M A, Walsh J L, Kong M G, Leys C and Schram D C 2010 Optical emission spectroscopy as a diagnostic for plasmas in liquids: opportunities and pitfalls *J. Phys. D. Appl. Phys.* **43** 124005
- [8] Lietz A M and Kushner M J 2016 Air plasma treatment of liquid covered tissue: long timescale chemistry *J. Phys. D. Appl. Phys.* **49** 425204
- [9] Vanraes P and Bogaerts A 2018 Plasma physics of liquids - A focused review *Appl. Phys. Rev.* **5**
- [10] Gorbanev Y and Bogaerts A Chemical Detection of Short-Lived Species Induced in Aqueous Media by Atmospheric Pressure Plasma 1–19
- [11] Mariotti D and Sankaran R M 2010 Microplasmas for nanomaterials synthesis *J. Phys. D. Appl. Phys.* **43** 323001
- [12] Sankaran R M, Giapis K P, Moselhy M and Schoenbach K H 2003 Argon excimer emission from high-pressure microdischarges in metal capillaries *Appl. Phys. Lett.* **83** 4728–30
- [13] Moselhy M, Petzenhauser I, Frank K and Schoenbach K H 2003 Excimer emission from microhollow cathode argon discharges *J. Phys. D. Appl. Phys.* **36** 2922–7
- [14] Bruggeman P and Brandenburg R 2013 Atmospheric pressure discharge filaments and microplasmas: Physics, chemistry and diagnostics *J. Phys. D. Appl. Phys.* **46**

- [15] Bruggeman P, Czarnetzki U and Tachibana K 2013 Special issue: Diagnostics of atmospheric pressure microplasmas *J. Phys. D. Appl. Phys.* **46** 14–7
- [16] Burlica R, Kirkpatrick M J, Finney W C, Clark R J and Locke B R 2004 Organic dye removal from aqueous solution *J. Electrostat.* **62** 309–21
- [17] Locke B R, Member S and Thagard S M 2009 Analysis of Chemical Reactions in Gliding-Arc Reactors With Water Spray Into Flowing Oxygen **37** 494–501
- [18] Maguire P D, Mahony C M O, Kelsey C P, Bingham A J, Montgomery E P, Bennet E D, Potts H E, Rutherford D C E, McDowell D A, Diver D A and Mariotti D 2015 Controlled microdroplet transport in an atmospheric pressure microplasma *Appl. Phys. Lett.* **106** 224101
- [19] Maguire P, Rutherford D, Macias-Montero M, Mahony C, Kelsey C, Tweedie M, Pérez-Martin F, McQuaid H, Diver D and Mariotti D 2017 Continuous In-Flight Synthesis for On-Demand Delivery of Ligand-Free Colloidal Gold Nanoparticles *Nano Lett.* **17** 1336–43
- [20] Stancampiano A, Galligani T, Gherardi M, Machala Z, Maguire P, Colombo V, Povesle J-M M and Robert E 2019 Plasma and Aerosols: Challenges, Opportunities and Perspectives *Appl. Sci.* **9** 3861
- [21] Fanelli F and Fracassi F 2013 Aerosol-Assisted Atmospheric Pressure Cold Plasma Deposition of Organic-Inorganic Nanocomposite Coatings *Plasma Chem. Plasma Process.* 1–15
- [22] Herbert P A F, O'Neill L, Jaroszyńska-Wolińska J, Stallard C P, Ramamoorthy A and Dowling D P 2011 A comparison between gas and atomized liquid precursor states in the deposition of functional coatings by pin corona plasma *Plasma Process. Polym.* **8** 230–8
- [23] O'Neill L, Herbert P A F, Stallard C and Dowling D P 2010 Investigation of the effects of gas versus liquid deposition in an aerosol-assisted corona deposition process *Plasma Process. Polym.* **7** 43–50
- [24] Kruszelnicki J A, Lietz A M and Kushner M J 2019 Atmospheric pressure plasma activation of water droplets *J. Phys. D. Appl. Phys.* **52** 355207
- [25] Davidovits P, Kolb C E, Williams L R, Jayne J T and Worsnop D R 2006 Mass accommodation and chemical reactions at gas-liquid interfaces *Chem. Rev.* **106** 1323–54
- [26] Iqbal M M, Stallard C P, Dowling D P and Turner M M 2015 Three-Dimensional Coupled Fluid--Droplet Model for Atmospheric Pressure Plasmas *Plasma Process. Polym.* **12** 201–13
- [27] Iqbal M M and Turner M M 2015 Investigations of Droplet-Plasma Interaction using Multi-Dimensional Coupled Model *Contrib. to Plasma Phys.* **55** 627–42
- [28] Iqbal M M, Stallard C P, Dowling D P and Turner M M 2015 Two-Dimensional Integrated Model for Interaction of Liquid Droplets with Atmospheric Pressure Plasma *Plasma Process. Polym.* **12** 1256–70

- [29] Bennet E D, Mahony C M O, Potts H E, Everest P, Rutherford D, Askari S, Mcdowell D A, Mariotti D, Kelsey C, Perez-martin F, Hamilton N, Maguire P and Diver D A 2016 Precision charging of microparticles in plasma via the Rayleigh instability for evaporating charged liquid droplets *J. Aerosol Sci.* **100** 53–60
- [30] Oinuma G, Nayak G K and Bruggeman P 2016 Micro-water droplets in non-equilibrium atmospheric pressure plasma: Evaporation and OH induced chemistry *IEEE International Conference on Plasma Science (ICOPS)*
- [31] Mussard M D V S, Foucher E and Rousseau A 2015 Charge and energy transferred from a plasma jet to liquid and dielectric surfaces *J. Phys. D. Appl. Phys.* **48** 424003
- [32] Pipa A and Brandenburg R 2019 The Equivalent Circuit Approach for the Electrical Diagnostics of Dielectric Barrier Discharges: The Classical Theory and Recent Developments *Atoms* **7** 14
- [33] Holub M 2012 On the measurement of plasma power in atmospheric pressure DBD plasma reactors *Int. J. Appl. Electromagn. Mech.* **39** 81–7
- [34] Hinds W C 1999 *Aerosol technology: properties, behavior, and measurement of airborne particles* (John Wiley & Sons)
- [35] Lefebvre A H and McDonell V G 2017 *Atomization and sprays* (CRC press)
- [36] Zhifu Z, Guoxiang W, Bin C, Liejin G and Yueshe W 2013 Evaluation of Evaporation Models for Single Moving Droplet with a High Evaporation Rate *Powder Technol.* **240** 95–102
- [37] Spalding D B 1953 The combustion of liquid fuels *Symposium (International) on Combustion* vol 4 pp 847–64
- [38] Godsave G 1953 Studies of the combustion of drops in a fuel spray—the burning of single drops of fuel *Symposium (International) on Combustion* vol 818 pp 818–30
- [39] Abramzon B and Sirignano W A 1989 Droplet vaporization model for spray combustion calculations **32** 1605–18
- [40] Sirignano W A 1999 *Fluid Dynamics and Transport of Droplets and Sprays* (Cambridge University Press)
- [41] Pinheiro A P and Vedovoto J M 2019 Evaluation of Droplet Evaporation Models and the Incorporation of Natural Convection Effects *Flow, Turbul. Combust.* **102** 537–58
- [42] Ranz W E, Marshall W R and Myers P 1952 Evaporation from drops *Chem. eng. prog* **48** 141–6
- [43] El Wakil M M, Uyehara O A and Myers P S 1954 *A theoretical investigation of the heating-up period of injected fuel droplets vaporizing in air*
- [44] Hubbard G L, Denny V E and Mills A F 1975 Droplet evaporation: effects of transients and variable properties *Int. J. Heat Mass Transf.* **18** 1003–8
- [45] Yuen M C and Chen L W 1976 *On drag of evaporating liquid droplets* (Taylor & Francis)

- [46] Cussler E L and Cussler E L 2009 *Diffusion: mass transfer in fluid systems* (Cambridge university press)
- [47] Wilke C R 1972 A Viscosity Equation for Gas Mixtures **517** 6–9
- [48] Huber M L and Harvey A H 2011 *Tables of recommended values for the viscosity and thermal conductivity of common gases as a function of temperature* ed CRC-Press
- [49] NIST Water - Gas phase thermochemistry data
- [50] NIST Argon - Gas phase thermochemistry data
- [51] Stabile L, Trassierra C V, Agli G D and Buonanno G 2013 Ultrafine Particle Generation through Atomization Technique: The Influence of the Solution 1667–77
- [52] Chen T M and Chein H M 2017 Generation and Evaluation of Monodisperse Sodium Chloride and Oleic Acid Nanoparticles *Aerosol Air Qual. Res.* **6** 305–21
- [53] Sarani A, Nikiforov A Y and Leys C 2010 Atmospheric pressure plasma jet in Ar and Ar/H<sub>2</sub>O mixtures: Optical emission spectroscopy and temperature measurements *Phys. Plasmas* **17** 063504
- [54] Ge L and Zhang Y 2014 A simple model for the calculation of plasma impedance in atmospheric radio frequency discharges *Plasma Sci. Technol.* **16** 924–9
- [55] Raizer Y P 1991 Gas discharge physics
- [56] Bruggeman P J, Sadeghi N, Schram D C and Linss V 2014 Gas temperature determination from rotational lines in non-equilibrium plasmas: A review *Plasma Sources Sci. Technol.* **23**
- [57] Bruggeman P, Schram D C, Kong M G and Leys C 2009 Is the rotational temperature of OH(A-X) for discharges in and in contact with liquids a good diagnostic for determining the gas temperature? *Plasma Process. Polym.* **6** 751–62
- [58] Bruggeman P, Iza F, Guns P, Lauwers D, Kong M G, Gonzalvo Y A, Leys C and Schram D C 2010 Electronic quenching of OH ( A ) by water in atmospheric pressure plasmas and its influence on the gas temperature determination by OH ( A - X ) emission **015016**
- [59] Xiong Z, Robert E, Sarron V, Pouvesle J M and Kushner M J 2013 Atmospheric-pressure plasma transfer across dielectric channels and tubes *J. Phys. D. Appl. Phys.* **46**
- [60] Tian W, Tachibana K and Kushner M J 2014 Plasmas sustained in bubbles in water: Optical emission and excitation mechanisms *J. Phys. D. Appl. Phys.* **47**
- [61] Malvern Instrument 2015 *A basic guide to particle characterization*
- [62] TSI Inc. 2012 *Aerosol statistics lognormal distribution and dN/dlogDp - Application Note PR-001*
- [63] Rask R B 1979 Laser Doppler anemometer measurements in an internal combustion engine *SAE Trans.* 371–82

- [64] Davis S S 1978 Physico-chemical studies on aerosol solutions for drug delivery I. Water-propylene glycol systems *Int. J. Pharm.* **1** 71–83
- [65] Looijmans K N H and Van Dongen M E H 1997 A pulse-expansion wave tube for nucleation studies at high pressures *Exp. Fluids* **23** 54–63
- [66] Bachalo W D, Rosa A B and Sankar S V 1991 Diagnostic for Fuel Spray Characterization *Combust. Meas.* 229–78
- [67] Zhang Y, Nishida K and Yoshizaki T 2001 Quantitative measurement of droplets and vapor concentration distributions in diesel sprays by processing UV and visible images *SAE Tech. Pap.*
- [68] Sulaiman S A, Ahmed Ismail A K A and Noor Azman M N F 2014 Scattering effects in laser attenuation system for measurement of droplet number density *Energy Procedia* **50** 79–86
- [69] Bohren C F and Huffman D R 2008 *Absorption and scattering of light by small particles* (John Wiley & Sons)
- [70] Jorabchi K, Kahen K, Gray C and Montaser A 2005 In situ visualization and characterization of aerosol droplets in an inductively coupled plasma *Anal. Chem.* **77** 1253–60
- [71] Iqbal M M, Stallard C P, Dowling D P and Turner M M 2015 Three-Dimensional Coupled Fluid–Droplet Model for Atmospheric Pressure Plasmas *Plasma Process. Polym.* **12** 201–13
- [72] Aghaei M and Bogaerts A 2016 Particle transport through an inductively coupled plasma torch: Elemental droplet evaporation *J. Anal. At. Spectrom.* **31** 631–41
- [73] Benson C M, Zhong J, Gimelshein S F, Levin D A, Montaser A and Valerie Camel 2003 Simulation of droplet heating and desolvation in inductively coupled plasma—part II: coalescence in the plasma *Spectrochim. Acta Part B At. Spectrosc.* **58** 1453–71
- [74] Levin D A, Benson C M, Gimelshein S F and Montaser A 2002 Simulation of droplet heating and desolvation in an inductively coupled plasma *IEEE Int. Conf. Plasma Sci.* 134
- [75] Stancampiano A, Galligani T, Gherardi M, Machala Z, Maguire P, Colombo V, Pouvesle J-M and Robert E 2019 Plasma and Aerosols: Challenges, Opportunities and Perspectives *Appl. Sci.* **9**

## 4.6 Appendix

### 4.6.1 Procedure for simulative data correction and comparison with experimental results

With the aim of comparing experimental and simulative results, droplet distribution for different time steps should consider both the complete evaporation of smaller droplet and the reduction of diameter due to droplet shirking. In this regard, the evaluation of droplet concentration was done for discrete time steps assuming that the droplet of each bin size could have been described with the mean bin dimension. The evaporation time of each bin was chosen as time step for the analysis of droplet concentration, as reported in Table 4.4. Afterwards, for each time step, bin size and gas temperature ( $T_g$ ) the reduction of aerosol

Bin number	Mean bin size[ $\mu\text{m}$ ]	Evaporation time [s]	$c$ [ $\text{m}^2/\text{s}$ ]	Surface reduction [%]
<hr/>				
t=1.18·10 <sup>-4</sup> s				
1	0.929	1.18·10 <sup>-4</sup>	7.34·10 <sup>-9</sup>	100%
2	1.083	1.60·10 <sup>-4</sup>	7.34·10 <sup>-9</sup>	74%
3	1.2625	2.17·10 <sup>-4</sup>	7.33·10 <sup>-9</sup>	54%
4	1.472	2.96·10 <sup>-4</sup>	7.33·10 <sup>-9</sup>	40%
...				
<hr/>				
t=1.60·10 <sup>-4</sup> s				
1	0.929	1.18·10 <sup>-4</sup>	7.34·10 <sup>-9</sup>	Evaporated at step 1
2	1.083	1.60·10 <sup>-4</sup>	7.34·10 <sup>-9</sup>	100%
3	1.2625	2.17·10 <sup>-4</sup>	7.33·10 <sup>-9</sup>	73%
4	1.472	2.96·10 <sup>-4</sup>	7.33·10 <sup>-9</sup>	54%
...				

Table 4.4 Examples of droplet surface reduction for two different time steps with a gas temperature of 430 K.

surface was done calculating the droplet diameter reduction for bins that didn't undergo a complete evaporation (Equation (4-33)) and removing the amount of area ascribable to evaporation process.

$$\text{Surface reduction} = \frac{D^2(t)}{D^2(0)} = \frac{D^2(0) - c(T_g) \cdot t_{\text{step}}}{D^2(0)} = 1 - \frac{c(T_g) \cdot t_{\text{step}}}{D^2(0)} \quad (4-33)$$

## Conclusions and Perspectives

Grown from the pioneering works carried out during the last century, atmospheric pressure plasma science and technology have shown incredible results in terms of supported processes and achieved functionalities. Despite the efforts done with the aim of shedding some light on the complex chemistry and physics behind atmospheric discharges, a comprehensive control of plasma processes has not yet been achieved.

Considering this, the aim of this dissertation was to report my work on the development and investigation of a plasma process for the treatment and functionalization of biomaterials characterized by anti-biofilm and anti-clot properties. Risen from the need of innovative solutions to fight hospital acquired infections caused by medical devices, the work here reported is mainly focused on the design, development and investigation of a plasma assisted process for the synthesis of silver nanoparticles (Ag NPs). Exploiting the reaction between silver nitrate containing droplets and the plasma discharge, Ag NPs were successfully *in-flight* synthesized and *in-situ* deposited on 2D and 3D substrates. The synthesis process was then combined with the plasma deposition of organic coatings, with the aim of developing a multilayer active film able to reduce cell adhesion and ensure high level of biocompatibility. The promising results of both *in-vitro* and *in-vivo* assays outlined important perspectives on process scalability. Nevertheless, as usual in industrial processes, the control of operating parameters and the possibility to tune the desired functionalities are required. While the plasma deposition process was already widely studied in the scientific communities, the modest amount of reported literature on droplet-plasma interactions drove further research activities towards a better understanding of synthesized particle characteristics. In the

perspective of controlling coating functionalities, the final aim of tuning Ag NPs properties was reached thanks to a comprehensive analysis of a flow-through plasma reactor where the droplet aerosol was introduced. The use several diagnostic techniques employed for the analysis of the multiphase environment of the plasma process suggested the key role of precursor concentration and droplet distribution on synthesized particle size. Moreover, results confirmed the importance of a single droplet both as a microreactor and as a microcarrier, through which synthesized particles can be locally delivered on biomaterial avoiding further process steps. According to the proposed conversion mechanism, the evaporation through the reactor due to plasma-liquid interaction could be accounted for the reduction of silver ions and the formation of a single Ag particle from each droplet. Beyond the control of particle distribution and, in perspective, of their antibacterial properties, precursor conversion efficiency was enhanced increasing the droplet residence time in the reactor. Furthermore, the results here presented suggest that the reduction of silver ions was driven by solvated electrons in the liquid phase, in accordance with what was previously reported in literature for batch processes. Droplet evaporation was finally studied combining an experimental and a simulative approach, with the aim of providing insights on the complex reaction between gas and liquid phase in the reactor and achieving a fine process control. According to the discussed results, droplet evaporation in plasma discharges is driven by thermal and diffusive forces, thus opening the possibility to control the droplet shrinking rate through gas temperature and residence time.

Towards the development of industrial processes, the results presented pointed out the possibility to support a multistep deposition process able to decrease biofilm adhesion and clot formation, while ensuring material biocompatibility. From a scientific point of view, future activities will need to address the effect of droplet size and plasma characteristics on synthesized particles. A better control of NPs size distribution and chemistry will indeed enable the possibility to tune the process with the aim of controlling coating functionalities for different applications. Future applications will also take advantages from a more accurate on-line control of plasma process together with the investigation of the effect of dynamic treatment. Finally, further efforts need to be devoted to the development of reliable pre-industrial plasma sources able to support developed processes and ensure their repeatability. While highlighting the outstanding potentialities of atmospheric pressure plasma technology for the processing of nanomaterials, the results presented in this dissertation confirmed the need of comprehensive and multidisciplinary approach to gain better understating of plasma processing of nano- and biomaterial. The introduction of plasma-droplet processes to enhance reaction rate and enable on-demand/in-situ delivery of nanomaterial has pushed forward new and challenging questions, that should be addressed. As happened for low pressure plasma, one can expect that bridges to other communities will probably be the key for the future success of plasma science and technologies, encouraging the rise of interests from the industrial world.

# Acknowledgments

At the end of every short or long journey, turning back and taking the time to travel again through experiences and emotions help us to make further steps into the future. For this reason, acknowledging who left either a small or big seed that was able to change our life is crucial and rightful.

This work would have never been possible without the funding support of Democenter-SIPE Foundation (Modena, Italy) who I gratefully acknowledge.

I owe my gratitude to my supervisor Prof. Vittorio Colombo for the chance to join his research group four years ago, helping me to grow through life and science. Beside his advices and our discussions that often broadened by point of view, I am grateful for the several opportunities to meet and work with other researchers from all around the world, making me feel a member of the scientific community.

I am also in debt to my co-advisor Dott. Matteo Gherardi for his friendship, his support and for the time spent together discussing and travelling.

My deepest heartfelt appreciation goes to Prof. Mohan Sankaran, who opened the doors of his research lab and group for me, encouraging my personal and scientific growth. This extraordinary experience left many seeds in my life over this past year, that are a gift to take care of.

The fruitful collaboration with the Technopole of Mirandola has been possible thanks to the efforts done by dott. Giorgio Mari, that I would like to greatly acknowledge. I am also grateful to dott. Elisa Resca and dott. Tiziana Petrachi for their support during biological assays.

I would like to acknowledge Prof. Alessandro Paglianti from the Department of Civil, Chemical, Environmental, and Materials Engineering of the University of Bologna for his help in the droplet size measurement.

I started this experience three years ago with two strangers, that have become more than friends over this time. Thank you, Federica, for your frank words, never obvious always fruitful. Thank you, Filippo, for your wild spirit, that somehow scratched my hard shell.

To my friends over the sea, Nabil Abuyazid and Joseph Toth, more fellow travellers than lab mates.

I have been part of an amazing research group: Alina, Augusto, Cristiana, Elisa, Emanuele, Enrico, Giulia, Marco, Romolo. My gratitude goes to all of you too.

To all my friends and my family, abiding presence during sunny days and safe harbour during the storms.

To Benedetta, past, present and future spring of love.